INVERSE ESTIMATION METHODOLOGY FOR THE ANALYSIS OF AEROHEATING AND THERMAL PROTECTION SYSTEM DATA

A Thesis
Presented to
The Academic Faculty

by

Milad Mahzari

In Partial Fulfillment
of the Requirements for the Degree
Doctor of Philosophy in the
Daniel Guggenheim School of Aerospace Engineering

Georgia Institute of Technology
December 2013

INVERSE ESTIMATION METHODOLOGY FOR THE ANALYSIS OF AEROHEATING AND THERMAL PROTECTION SYSTEM DATA

Approved by:

Dr. Robert D. Braun, Advisor
Daniel Guggenheim School of
Aerospace Engineering
Georgia Institute of Technology

Dr. Stephen M. Ruffin
Daniel Guggenheim School of
Aerospace Engineering
Georgia Institute of Technology

Prof. David A. Spencer
Daniel Guggenheim School of
Aerospace Engineering
Georgia Institute of Technology

Dr. Michael J. Wright
Entry Systems and Technologies
Division
NASA Ames Research Center

Dr. John A. Dec
Structural & Thermal Systems Branch
NASA Langley Research Center

Date Approved: October 30, 2013

To my parents, Alireza and Zohal.

All I have ever accomplished would have been impossible without their endless love, sacrifice, support and guidance.

ACKNOWLEDGEMENTS

Many people have helped me throughout my academic career and without their encouragement and support this manuscript would have not come into existence. I would like to thank my advisor, Robert Braun, for providing exceptional technical insight and motivation for my graduate work. His leadership, wisdom, passion and dedication have been an inspiration to me for the past few years and will continue to inspire me in future. I am very grateful for his help with developing a well-balanced academic plan that has allowed me to discover things on my own while ensuring that I stay on track. I am also very thankful to Ian Clark who provided me with unlimited help during his two years at Georgia Tech as a visiting professor. I wish to thank the other members of my committee, John Dec, Stephen Ruffin, David Spencer, and Michael Wright whose guidance and support have been invaluable and greatly appreciated.

This research was completed with the assistance of numerous individuals throughout the NASA community both in person during my summer internships and remotely during my time back at Georgia Tech. The constant support and technical insight offered by Deepak Bose, David Hash and Todd White have been instrumental in completing my research. I am also very grateful to Ioana Cozmuta, Karl Edquist, Bernie Laub, Jose Santos and Jay Feldman for their time to discuss some aspects of my research.

This work would have been impossible without the exceptional education I received at Georgia Tech. I am very grateful to the faculty and staff of the Daniel Guggenheim School of Aerospace Engineering for that. I am also very thankful for my colleagues in the Space Systems Design Laboratory, who provided good company

during countless hours in the lab and always improved my work by their valuable thoughts and feedback.

Finally I would like to thank my parents, Alireza and Zohal, for their endless love, support and sacrifice throughout all my life. Without them, I would have never come this far. I am very grateful to my sister, Afsaneh, for her unwavering love and friendship. I would also like to thank my fiance, Shirin, for being supportive and understanding of the long hours and hard work that went into this manuscript.

TABLE OF CONTENTS

LIST OF TABLES

LIST OF FIGURES

NOMENCLATURE

Acronyms

ACE	Aerotherm Chemical Equilibrium program
ARAD	Analog Resistance Ablation Detector
BET	Best Estimated Trajectory
BLT	Boundary Layer Transition
CAT	Charring Ablator Thermal response code
CEV	Crew Exploration Vehicle
CFD	Computational Fluid Dynamics
CMA	Charring Material thermal response and Ablation program
DES	Detached Eddy Simulation
DNS	Direct Numerical Simulation
DPLR	Data Parallel Line Relaxation
DSC	Digital Scanning Calorimeter
DSMC	Direct Simulation Monte Carlo
EDL	Entry Descent and Landing
EKF	Extended Kalman Filter
FEA	Finite Element Analysis
FIAT	Fully Implicit Ablation and Thermal response program

HEAT	Hollow aErothermal Ablation and Temperature sensor
IHCP	Inverse Heat Conduction Problems
IHF	Interaction Heating Facility
IHTP	Inverse Heat Transfer Problems
IMU	Inertial Measurement Unit
IPE	Inverse Parameter Estimation
KF	Kalman Filter
L/D	Lift-to-Drag ratio
LAURA	Langley Aerothermal Upwind Relaxation Algorithm
LES	Large Eddy Simulation
LHMEL	Laser-Hardened Materials Evaluation Laboratory
MAT	Multi-component Ablation Thermochemistry program
MC	Monte Carlo
MEADS	Mars Entry Atmospheric Data System
MEDLI	MSL Entry, Descent, and Landing Instrumentation
MISP	MEDLI Integrated Sensor Plug
MSL	Mars Science Laboratory
NAD	Normalized Absolute Difference
NASA	National Aeronautics and Space Administration
PDF	Probability Distribution Function

PICA	Phenolic Impregnated Carbon Ablator
RANS	Reynolds-Averaged Navier-Stokes
RCS	Reaction Control System
RIE	Relative Integrated Error
RMS	Root Mean Square
RSS	Root Sum Squared
SCEBD	Self-Consistent Effective Binary Diffusion
SEB	Surface Energy Balance
SLA	Super-Light Ablator
SSE	Sensor Support Electronics
SST	Shear Stress Transport
TC	thermocouple
TGA	Thermo Gravimetric Analysis
TPS	Thermal Protection System
UKF	Unscented Kalman Filter

Greek Variables

α	surface absorptivity	
β	energy accommodation coefficient	
$\boldsymbol{\eta}$	vector of material true temperature response	K
Δ	change in a parameter	

Δ	normalized 2σ uncertainty	
ϵ	error	
ϵ	surface emissivity	
Γ	volume fraction of resin	
γ_N	catalytic efficiency	
κ	thermal conductivity	W/mK
λ	blowing reduction parameter	
μ	Levenberg-Marquardt damping parameter	
μ	Tikhonov regularization parameter	
ϕ	material porosity	
Ψ	decomposition reaction order	
ρ	density	kg/m^3
σ	Stefan-Boltzmann constant	W/m^2K^4
σ	standard deviation	
τ	mass fraction of virgin material	

Subscripts

∞	freestream
c	char
cond	conduction
e	boundary layer edge

g	pyrolysis gas
$host$	host material
i	density component
i, j	counters
rad	radiative
s	material surface
$true$	true value
v	virgin
w	wall
$wire$	wire properties

Superscripts

BE	best estimate
k	iteration number
Nom	nominal
T	transpose

Roman Variables

$\bar{h}$	partial heat of charring	J/kg
$\dot{m}$	mass flux	kg/m^2s
$\dot{s}$	surface recession rate	m/s
$\mathbf{I}$	Identity matrix	

H1	Tikhonov first order regularization matrix	
H2	Tikhonov second order regularization matrix	
J	sensitivity matrix (Jacobian)	
P	vector of estimation parameters	
T	vector of FIAT temperature predictions	K
Y	vector of temperature measurements	K
A	surface area	m^2
B'	dimensionless mass blowing rate	
B_a	pre-exponential constant rate	$1/s$
C_H	heat transfer coefficient = $\rho_e u_e C_h$	$kg/m^2 s$
C_h	Stanton number for heat transfer	
C_M	Stanton number for mass transfer	
c_p	specific heat	J/kgK
C_{h1}	unblown Stanton number for heat transfer	
E_a	activation temperature	K
F	view factor	
G	physical model (FIAT)	
h	enthalpy	J/kg
h_c	contact conductance	$W/m^2 K$
H_r	recovery enthalpy	J/kg

M	number of measurements	
N	number of estimation parameters	
P	pressure	atm
q	heat flux	W/m^2
Re	Reynolds number	
S	ordinary sum of square of errors function	K^2
s	surface recession	m
Sc_T	turbulent Schmidt number	
T	temperature	K
t	time	s
u	velocity	m/s
V	volume	m^3
W_0	zero-order regularization weighting parameter	
W_1	first-order regularization weighting parameter	
W_2	second-order regularization weighting parameter	
x	moving coordinate $= y - s$	m
y	stationary coordinate	m

SUMMARY

The interaction between an entry vehicle and an atmosphere during the hypersonic phase of flight results in a high-temperature flowfield around the forebody surface of the vehicle. A Thermal Protection System (TPS) is required to protect the vehicle from such severe environments. There are significant uncertainties in the tools and models currently used for the prediction of entry aeroheating and TPS material response such as the level of heating augmentations due to turbulent flow and catalytic effects, TPS recession and material properties. Experimental data can significantly reduce these uncertainties. Analysis of TPS ground and flight data has been traditionally performed in a direct fashion. Direct analyses involve comparison of the computational model predictions to data. Qualitative conclusions about model validity may be drawn based on this comparison and a limited number of model parameters may be adjusted to obtain a better match between predictions and data. For example, in past work, the reconstruction of surface heating has been limited to simple scaling of the predicted heating profile.

The goal of this research is to develop a more rigorous methodology for the reconstruction of surface heating and TPS material response using inverse estimation theory. Built on theoretical developments made in related fields, the developed methodology enables the estimation of uncertainties in both the aeroheating environment and material properties from subsurface TPS temperature measurements. This methodology is composed of two parts: the multi-parameter estimation framework and the surface heating function estimation framework. The former is aimed at the estimation of multiple constant parameters such as material properties, while the latter is aimed

at the time-dependent estimation of surface heating profiles. Additionally, a thermocouple (TC) driver approach is developed and employed to decouple the surface heating and in-depth heat transfer problems. In this approach, shallow thermocouple data is first used as the true boundary condition and the heat transfer problem is solved for the remaining TPS material under the thermocouple. This technique enables the independent application of both frameworks to flight data to estimate both material parameters and surface heating profiles.

In this thesis, the methods and tools required for inverse estimation of aeroheating and TPS material response are developed. These tools have been developed for application to flight data obtained from thermocouples embedded in the Mars Science Laboratory (MSL) heatshield during its August 6, 2012 hypersonic entry; however, in this manuscript they are employed in multiple test problems to demonstrate their feasibility and applicability for other functions. First, the multi-parameter estimation framework is applied to a relevant arc jet dataset. This framework performs nominal, uncertainty and sensitivity analyses to select the set of parameters and the range of measurements that should be used in the estimation process. Next, the feasibility of the surface heating estimation framework is demonstrated through application to simulated MSL data and Mars Pathfinder flight data. Ultimately, both frameworks are applied to MSL flight data to estimate its surface heating profile and TPS material performance. A discussion of how findings from MSL data may influence TPS design margin policies follows. Recommendations regarding possible improvements to heatshield instrumentation for future missions are also presented.

The evolved inverse estimation methodology is a significant advance relative to past aerothermal and TPS material response reconstruction methods. The benefits of this methodology goes beyond the applications demonstrated in this thesis. The tools and frameworks introduced here can be applied to all future flight and ground data as a complementary analysis approach to the traditional direct approach.

CHAPTER I

MOTIVATION AND BACKGROUND

1.1 Motivation

Mars has been and will continue to be a frequent destination in space exploration efforts. Starting with the Mars Viking program in 1970s, the United States National Aeronautics and Space Administration (NASA) has successfully landed seven spacecraft on the surface of Mars. Most recently on August 6, 2012, the Mars Science Laboratory (MSL) landed on the surface of Mars. The MSL rover, Curiosity, is the largest mass ever delivered to the surface of Mars.

When spacecraft travel to other planetary surfaces or when they return to Earth upon the completion of their missions, they typically enter the planet's atmosphere at high velocity. During flight between the atmospheric interface and surface, called Entry, Descent and Landing (EDL), spacecraft use a wide range of technologies to reduce the vehicle's velocity to levels safe for landing. Mars EDL is a challenging problem mainly due to the fact that Mars' atmosphere is thick enough to cause significant heating, but not thick enough to slow down the spacecraft to a safe terminal velocity. [1] Figure 1 shows the MSL EDL sequence illustrating a combination of heatshield, hypersonic guidance, supersonic parachute, propulsive descent and landing technologies used to safely place the rover on the surface of Mars. [2]

An important and enabling system used in most EDL missions is the heatshield. During entry, the interaction between the spacecraft and the planet's atmosphere will generally dissipate more than 90% of the entry system's initial kinetic energy, mostly in the form of heat. The heatshield must keep the aeroshell interior safe from these extreme environments. The Thermal Protection System (TPS) material is

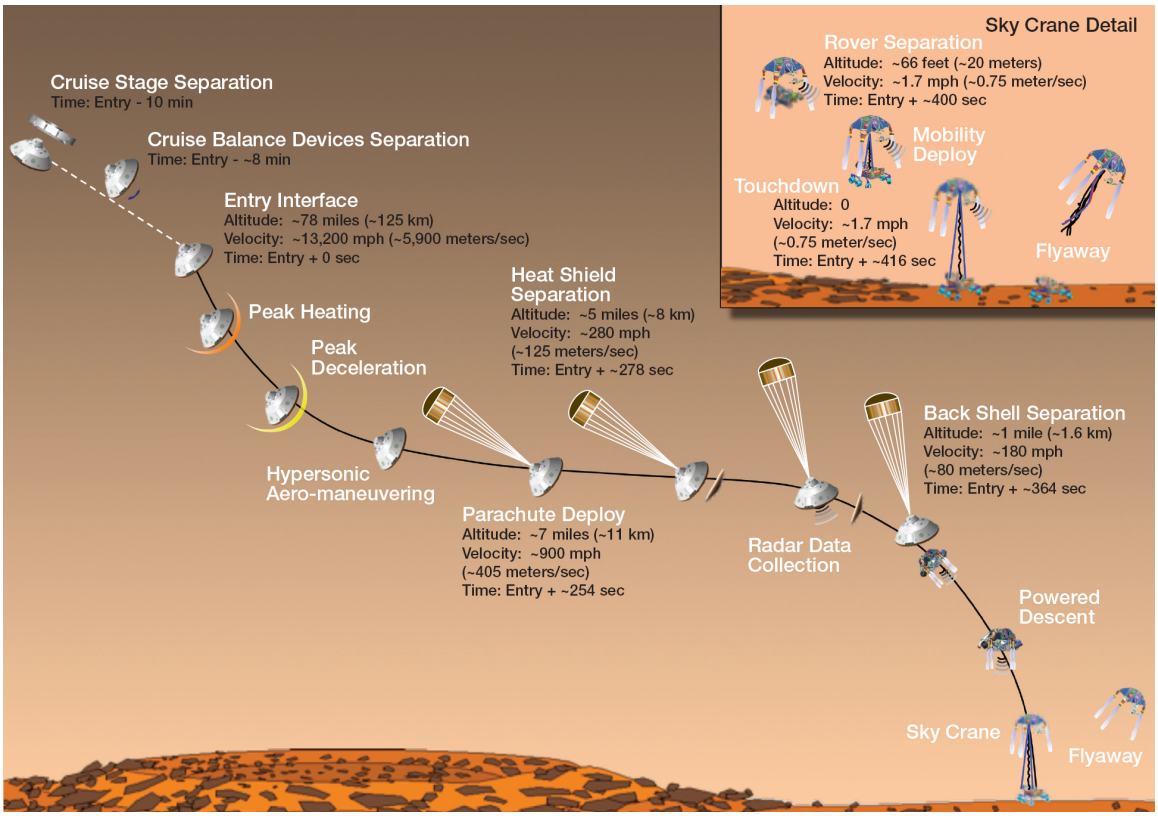

Figure 1: MSL EDL sequence illustrating the advanced technologies used to land the Curiosity rover on Mars.

responsible for rejecting most of this incoming heat and minimizing heat conduction to the payload. Since the TPS is critical to mission success, the physics of entry aeroheating and TPS material response have to be understood accurately. This is accomplished with a combination of ground and flight testing and computational modeling.

There have been significant advancements in the analytical models used for predicting aeroheating and TPS response; however, substantial uncertainties remain. Uncertainties exist in the modeling of the heating augmentation due to flow turbulence, roughness effects and surface catalysis for ablative materials. Figure 2 from Ref. [3] shows how different catalysis and turbulence models result in significantly different centerline heating predictions for the MSL vehicle. Besides aeroheating modeling, there are also large uncertainties in our ability to accurately predict TPS

material recession and estimate certain TPS thermophysical properties such as char thermal conductivity. These uncertainties have a significant effect on the TPS material selection and total heatshield mass, and therefore affect our ability to design more capable and robust EDL systems.

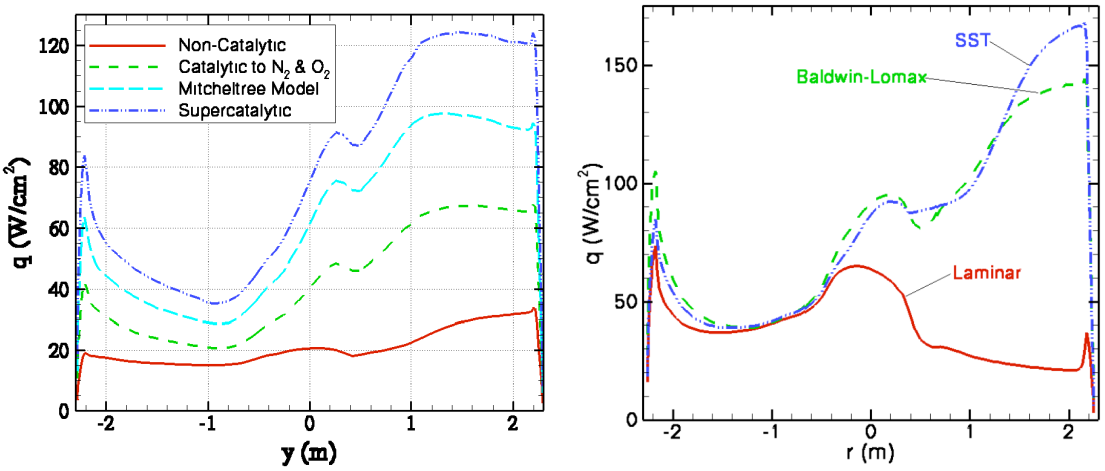

Figure 2: Substantial uncertainties in MSL centerline heating augmentation due to catalysis and turbulence.

Flight data can help engineers reduce these uncertainties thus improving or validating the computational tools. During the past few decades, there have been numerous entry missions that were equipped with instruments to collect aeroheating and TPS performance data, primarily in support of the Apollo program. [4] Lessons have been learned from these efforts, but some of the returned data have either not been critically evaluated or were not sufficient for code validation. A majority of these instrumented missions have occurred in the Earth atmosphere. To date, Viking and Pathfinder have been the only Mars missions equipped with forebody TPS instruments. [5] The need for Martian flight data is further justified since the experimental facilities on Earth are not capable of fully recreating Mars flight conditions.

The MSL entry vehicle is instrumented with aerodynamic and aeroheating sensors. The MSL aeroshell is a 4.5-meter diameter spherically-blunted 70-deg half-angle cone with a triconic afterbody. [6] MSL's heatshield is made of an ablative material

called Phenolic Impregnated Carbon Ablator (PICA). [7] The MSL Entry, Descent, and Landing Instrumentation (MEDLI) [8] suite includes pressure sensors, called Mars Entry Atmospheric Data System (MEADS) and temperature sensors called MEDLI Integrated Sensor Plug (MISP) placed at different locations on the heatshield. There are seven MISP plugs, each containing four subsurface thermocouples and one isotherm sensor. The MEDLI dataset will provide the first non-Earth entry aeroheating data since the Pathfinder mission and will provide more EDL data than all of the previous Mars missions combined. [8] Figure 3 shows the completed MSL heatshield with MEDLI sensors installed. [9]

Figure 3: Completed MSL heatshield and underside with MEDLI system installed.

The flight data acquired by MISP will help answer fundamental questions related to aeroheating and TPS performance while also addressing the uncertainties associated with current tools. A systematic post-flight data analysis strategy is required to maximize the benefits of the MISP data. Traditionally, flight and ground TPS data were analyzed in a direct fashion. [5] Model predictions were directly compared to the flight data and general conclusions were made regarding the accuracy of the modeling tools. Some parameters were manually changed to investigate if an adjustment in the model could result in a better match with the data. The time-dependent surface heating profile was simply scaled until a close qualitative match with the data was obtained.

The main goal of this research is to develop a more rigorous methodology for application to MISP data based on Inverse Parameter Estimation (IPE) theory. The set of methodology and tools created in this work use inverse estimation methods to reconstruct both MSL's surface heating and PICA in-depth material response from MISP data. This will enable targeting the uncertainties in both the aeroheating environment prediction and material properties and performance. Unlike past analyses, the methodology developed here is capable of estimating multiple parameters and reconstructing the complete time-dependent surface heating profile in an automated fashion. While this work is motivated by the analysis of MISP data, the methodology and tools developed for this purpose are applicable to future TPS flight and ground experimental data.

The development of a methodology for the inverse analysis of aeroheating and TPS experimental data is a multi-disciplinary topic involving aerothermal heating, TPS material response, flight instrumentation and inverse estimation. Therefore, the background research provided in this chapter is divided into sections. The first section provides a review of the current aerothermal modeling efforts for Mars entry environments. The second section discusses the current modeling techniques used in the field of ablative material thermal response. The third section provides a summary of past relevant TPS flight data and a detailed description of the MEDLI instrument with a focus on the MISP subsystem. These sections are followed by a discussion of the contributions of this thesis and a brief outline of the document. Chapter 2 will provide background on inverse problems and methods employed to solve these problems focusing mainly on the inverse problems encountered in the heat transfer field and the methods devised to tackle Inverse Heat Transfer Problems (IHTP).

1.2 Mars Entry Aerothermal Modeling

The aerothermal environment of an entry vehicle is modeled with continuum or non-continuum (rarefied) fluid dynamics at different parts of the entry trajectory depending on the size of the vehicle, its entry velocity and the density of the atmosphere. [10] For most missions of interest using rigid aeroshells, the majority of the heat pulse occurs in flow regimes where continuum flow physical models are valid. For this reason, the discussion presented here focuses solely on continuum flow physics during Martian entry.

Wright et al. [3] and Hollis et al. [11] provide reviews of the status of continuum aerothermal modeling for Mars entry missions. References [12, 13] also discuss aerothermal modeling challenges for entry missions at Earth and other planetary bodies. Material from these works are widely used in this review. While rarefied flow is not a focus of this research, Moss et al. provide an excellent summary of Direct Simulation Monte Carlo (DSMC) techniques that are normally used for the analysis of rarefied flows. [14] The following sections review the best-practice Martian entry aerothermal physical models. Different sources of uncertainty in the models are discussed.

1.2.1 Physical Models

The Mars atmosphere is composed of approximately 97% CO_2 and 3% N_2 by volume. During the hypersonic phase of the entry, a strong bow shock forms in front of the vehicle creating a high-temperature flowfield in the region between the shock and the vehicle's surface. As the gas heats up, energy is transferred between different modes resulting in a vibrationally excited gas. Molecules dissociate, ionize and radiate while undergoing chemical reactions. This high-temperature flowfield interacts with the vehicle's surface resulting in surface reradiation, ablation and pyrolysis gas blowing. Figure 4 from Wright [15] shows a schematic of the aerothermal phenomena

that occur during a blunt body's atmospheric entry. Computational Fluid Dynam-

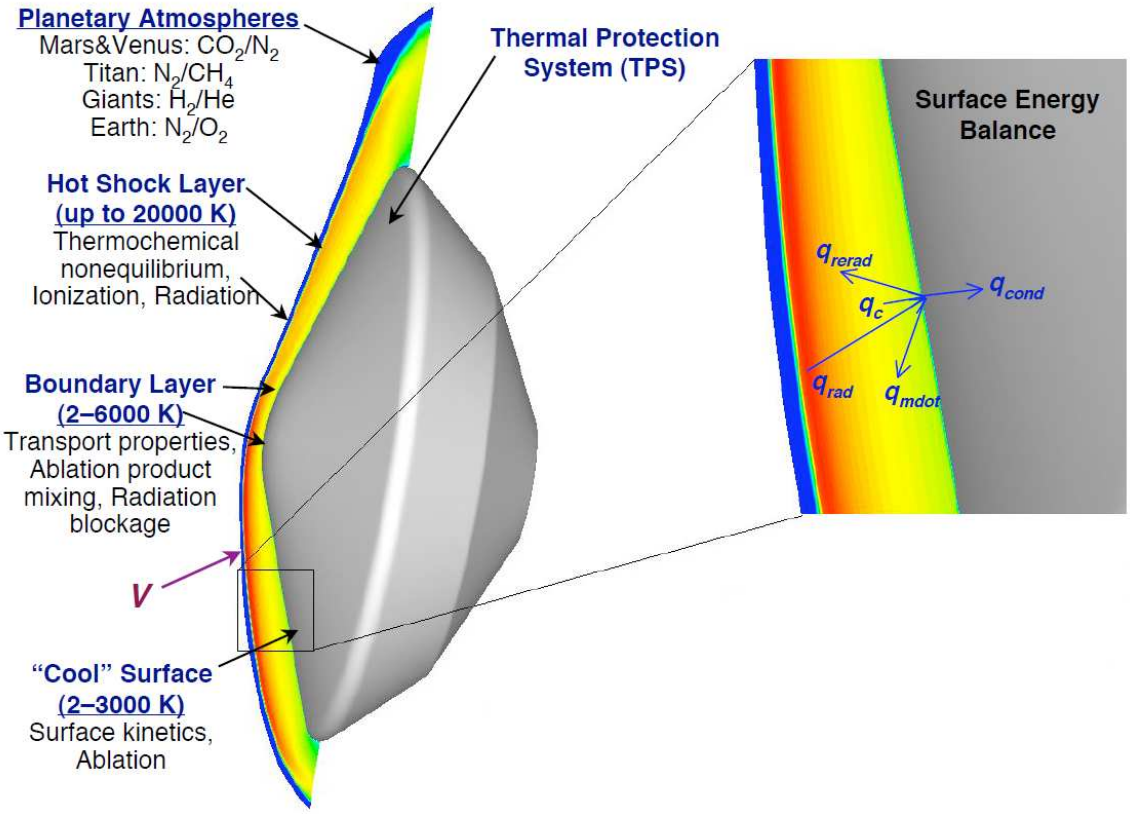

Figure 4: Schematic of a blunt body's aerothermal environment during atmospheric entry.

ics (CFD) tools are normally used to solve the Navier-Stokes equations governing the flow physics. [16] These flows are usually modeled in thermochemical non-equilibrium. Gnoffo et al. provide a review of the relevant conservation equations and physical models used to describe hypersonic flows in thermochemical non-equilibrium. [12, 17] These models use a two-temperature formulation that assumes the vibrational and electronic modes of the gas are in equilibrium, but not with the translational and rotational components. [18] Vibrational relaxation times for most species are obtained from works by Millikan and White,[19] Camac,[20] and Park et al. [21] The thermodynamic properties for component species are taken from Gordon and McBride [22] and a recent work by Capitelli et al. [23] A reduced 8-species, 13-reaction mechanism from Mitcheltree and Gnoffo [24] is used to model the non-equilibrium chemical kinetics of

the shock layer. The modeling of transport properties of a reacting gas mixture and the required input collision integrals are reviewed in detail by Wright et al. [25, 26].

1.2.2 Turbulence

Turbulent heating has not been an important issue for past Mars entry missions since small blunt aeroshells were used. However, for larger aeroshells or high Lift/Drag (L/D) slender entry vehicles, the flow is expected to transition to turbulent and the resulting heating augmentation will be significant. Hypersonic turbulent flow is modeled using methods ranging from simple algebraic models to the more complicated and general Direct Numerical Simulation (DNS) techniques. Traditionally for Mars entries, simulations have been performed using either the Baldwin-Lomax algebraic model [27] or the two-equation Shear Stress Transport (SST) model. [28] Both models have been corrected for compressibility effects and while Baldwin-Lomax is frequently used for the design purposes, the SST model has proved to be more accurate for many applications. [29] The heating levels predicted by these models is sensitive to the turbulent Schmidt number (Sc_T) used in the simulations; therefore, Reynolds-Averaged Navier-Stokes (RANS) models that allow a variable Schmidt number can be beneficial for Martian entry simulations. [3] Other models such as Large Eddy Simulation (LES) or Detached Eddy Simulation (DES) can provide better results; however, they are computationally expensive for flight full-vehicle analysis.

The onset of turbulent transition has been traditionally modeled using simple geometry-based correlations such as a critical value for the momentum thickness Reynolds number (Re_θ). [6, 30] Once such criterion is reached, the entire vehicle is assumed to be completely turbulent to be conservative for design purposes. Chang et al. [31] give a more detailed overview of the transition analysis that was performed for the MSL entry vehicle. However, this simple smooth-wall criterion is not sufficient. New transition criteria have to be developed that account for transition due

to the ablation-produced roughness effects [32] or blowing of pyrolysis gas into the boundary layer. [33] The existing and future flight and ground data [34, 35] for entry vehicles will contribute significantly to developing representative transition models.

Due to the lack of relevant Martian flight data, current turbulence models have not been well-validated. This was not an issue for previous Mars missions as they flew mostly laminar trajectories. However, for larger vehicles, the uncertainties in our turbulence models are crucial. Transition to turbulence was expected for the MSL entry vehicle and it experienced moderate turbulent heating augmentation. This is due to a combination of large aeroshell size, high ballistic coefficient and large angle of attack. Figure 2 shown earlier illustrates how turbulence can result in a factor of two heating augmentation for the MSL peak heating. Ground testings [36, 37] had also confirmed the heating augmentation predicted by computational models. However, flight conditions can not be completely matched in such ground testings. Therefore, flight data analysis is critical to validating these models.

1.2.3 Surface Catalysis

The exothermic recombination of dissociated species at the TPS surface can augment the convecting heating experienced by the reentry vehicle. Such catalytic processes are poorly understood due to the lack of relevant measurements in representative environments. The heating transferred to the surface by catalytic recombination depends on catalytic efficiency, γ_N (fraction of incident atoms that recombine at the surface), and energy accommodation coefficient, β (fraction of recombination energy that is transferred to the surface). Catalytic efficiency depends mainly on the TPS material. Stewart has studied the catalytic properties of several TPS materials in air. [38] However, TPS catalysis experiments in dissociated CO_2 have not been performed as extensively. [39, 40]

Four simplified catalytic mechanisms are commonly used in the literature. [3]

The simplest model is "non-catalytic" which assumes no recombination of incident atoms. The other extreme is the "supercatalytic" wall model which assumes the recombination of all atoms to the lowest chemical enthalpy state (CO_2/N_2). This is the model commonly used in design because it represents the limiting case of highest heating even though it is not physically based. Another catalysis mechanism was developed during the Mars Pathfinder program by Mitcheltree [24, 41] which assumes that CO_2 recombination happens in a two-step reaction with two parallel paths. This model results in lower heat flux predictions than the supercatalytic model when significant amounts of O_2 are present in the boundary layer edge. [3] The last model, called "catalytic to N_2 & O_2" assumes that CO_2 does not recombine for Martian entry conditions based on the results of related ground experiments. [40] This model results in significantly lower heating than the previous models. Figure 2 illustrates how surface catalysis assumptions result in a factor of three difference in MSL peak heating.

Figure 5 from Ref. [42] compares the results of CFD simulations with the T5 hypervelocity shock tunnel data for expected laminar and turbulent cases. The simulations were performed using two NASA-developed codes, Data Parallel Line Relaxation (DPLR) [43] and Langley Aerothermal Upwind Relaxation Algorithm (LAURA). [44] It can be observed that for the laminar case (plot a), the data match the CFD simulations with the supercatalytic model; however, for the case of leeside turbulent flow (plot b), the data are closer to the turbulent simulations with non-catalytic assumption. These results, combined with other ground test results, show that there are still large uncertainties in our surface catalysis modeling approaches.

1.2.4 Additional Topics

When the surface of an ablative heatshield meets the high-temperature flowfield of the shock layer, it ablates and forms a porous and rough char layer. The surface

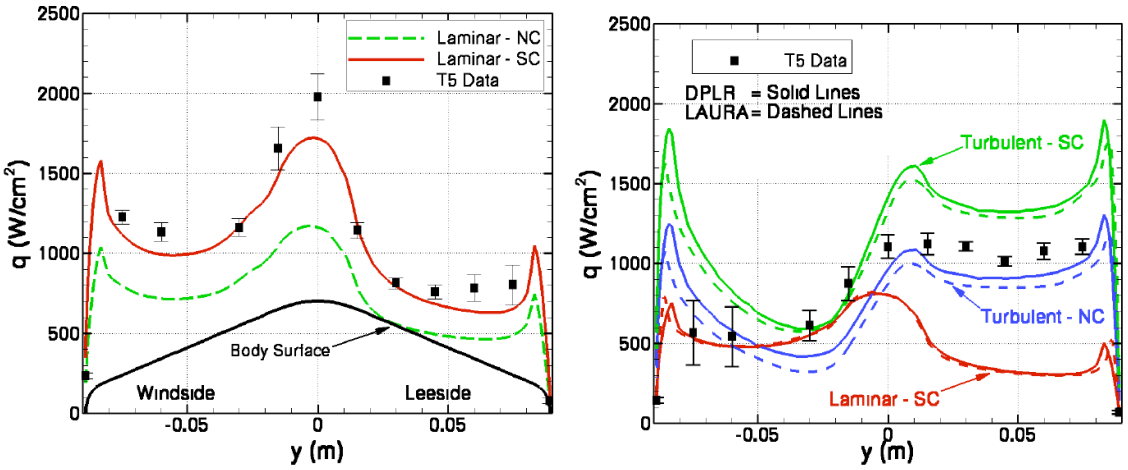

(a) Laminar Case (b) Turbulent Case

Figure 5: Comparison of CFD simulations with T5 shock tunnel data.

roughness has a significant effect on transition to turbulence and results in high levels of heating augmentation. Furthermore, the material pyrolyzes in-depth and the resulting pyrolysis gas convects through the char layer and blows into the boundary layer. This can reduce the convective heat transfer through transpiration, and reduce the heating augmentation caused by the TPS surface roughness. [3]

There has been extensive experimental and theoretical work done to characterize the combined effect of roughness heating and blowing cooling;[45, 46] however, transpiration effects are currently not modeled in CFD methods and are treated using simple correlation methods within the TPS thermal response solvers. [47] These methods reduce the surface heat transfer coefficient computed from flow solvers using a blowing correction factor. Additionally, the blowing of ablation products and pyrolysis gas can alter the catalytic properties of the TPS surface. A coupled flow-solver and material response-solver is required to capture these phenomena. While there has been some work done in this area [48, 49, 50], more experimental data is required for the identification of the related surface mechanisms and rates.

The level of heating due to shock layer radiation has been minimal for the Mars

entry missions so far. However, as future missions will demand higher entry velocities and larger aeroshells, radiative heating may become a significant contributor. Diatomics such as CO and CN that are formed in the high-temperature flowfield have strong radiative properties. [13] There has been substantial work in literature in developing radiation models for Earth entries; however, no validated model exists for shock layer radiation in a CO_2 environment. [3] Some experimental data has been recently obtained for CO_2 shock layer radiation modeling. [51] Radiative heating for MSL entry vehicle is expected to be minimal.

This review focused on forebody heating prediction, but the uncertainties in the afterbody heating prediction are much larger. Large margins are typically applied to mitigate for this uncertainty; however, such margins affect the choice of afterbody TPS material and overall mass significantly. Wright et al. provided a survey of available afterbody experimental and flight data for code validation and discussed the main uncertainties in predicting afterbody heating. [4] Analysis was also done to estimate the level of afterbody aeroheating experienced by the Pathfinder,[24] Pheonix [52] and MSL [53] missions. Another source of uncertainty is singularity heating due to localized effects from heatshield penetrations or Reaction Control System (RCS) thrusters. Reference [3] provides a summary of some of the missions that dealt with such singularities in the heatshield and the simulations that were performed to predict the amount of localized heating they caused.

Finally, it should be noted that validation efforts involve the use of ground testing techniques which are not capable of matching all the flight conditions exactly an cannot match all the flght parameters simultaneously. This introduces a ground to flight traceability issue meaning that the current uncertainties in the tools can be ultimately reduced only using flight data. This motivates active instrumentation on missions and flight test programs. MEDLI will return valuable data for code validation. Accurate estimation of surface heating from flight data is a crucial step

in reducing the uncertainties in our computational aerothermal models.

1.3 Ablative Material Thermal Response Modeling

Heatshield materials are employed to protect the entry vehicle against the harsh aeroheating environments. Two types of materials are typically used: passive and ablative. Passive materials are reusable and rely on surface reradiation to reject the incoming heat. These systems normally have low thermal conductivity which minimizes the penetration of the heat in-depth. However, these materials are limited by reusable surface temperatures and heat fluxes. On the other hand, ablative materials are typically used for the higher heating conditions. These material combine reradiation with ablation and pyrolysis for heat rejection, but are not reusable. Figure 6 from Ref. [54] provides a schematic of ablative material thermal response both at surface and in-depth.

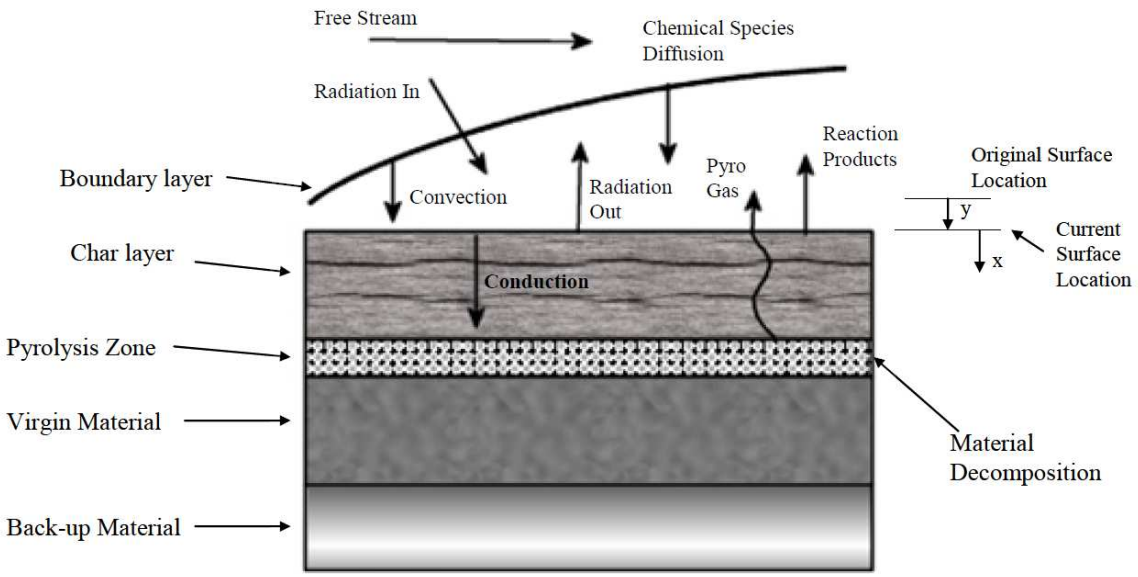

Figure 6: Ablative material surface and in-depth thermal response.

As the TPS material heats up, it ablates. Ablation is defined as the absorption of energy using the removal of surface material by a combination of different processes such as melting, vaporization, sublimation or chemical reaction. Mechanical removal

of material is also possible and is called spallation (spallation is not desirable because it does not absorb a significant amount of energy). Ablation results in the surface of the material receding. Most ablative materials are pyrloyzing. These materials are typically composed of two main components: (1) a substrate material such as carbon or glass that can withstand high temperatures and have favorable ablation and reradiation performance, and (2) organic resins such as phenolics that can absorb energy through pyrolysis. Other components such as microballoons, cork or honeycomb can also be added to provide structural integrity or density and thermal conductivity control. In addition to surface reactions, as these materials heat up, they decompose, meaning that the resin component generates gas and leaves carbon residue. This process is called pyrolysis and involves endothermic reactions which absorb energy. The pyrolysis gas convects though the char material above it and blows into the boundary layer. This creates three regions in the material as can be seen in Figure 6. On top, there is a char layer which consists of fully decomposed material. Virgin material with no decomposition is on the bottom. The area in between is called the pyrolysis zone where the material is partially decomposed.

TPS material selection and modeling is affected by a range of factors. Surface heat rates drive the TPS material selection while the TPS thickness is greatly dependent on the heat load integrated over the vehicle's trajectory. In addition to the heating conditions, other factors such as the severity of the shear environment, the size of aeroshell and manufacturability of the TPS also affect TPS design choices. Depending on the ablative and insulative requirements, different ablative TPS materials have been used for planetary missions, including AVCOAT, carbon phenolic, carbon-carbon, Super-Light Ablator (SLA) and PICA. For example carbon phenolic is a good ablator and can withstand high heat rates but is not a good insulator due to its high density. This material has been used for Venus and Jupiter missions that experienced heat rates in the excess of 10000 W/cm^2. [55, 56]

On the other hand, SLA is a good insulator with a low density. It experiences thermal and mechanical failure at heat rates above 200 W/cm^2. [57] This material was used for all Mars missions except MSL. The high heating and shear expected for MSL resulted in the selection of PICA as its TPS material. [7] PICA is a low density material that is a good insulator and can withstand heat rates as high as 1500 W/cm^2. [58, 59] It was also employed as the TPS material for the Stardust sample return mission and was one of the two possible candidates for the Crew Exploration Vehicle (CEV) heatshield. [60] The general approach employed in heatshield design is to select a material that provides reliable performance for the expected heating conditions, and then size its thickness such that the aeroshell/heatshield bondline temperature does not exceed a specified value. Validation of these requirements is achieved with a combination of theoretical modeling and experimental efforts. Physical models are developed to characterize the material thermal response both at surface and in-depth. These models are then validated and calibrated by testing in ground facilities such as arc jets.

1.3.1 Early Ablation Modeling

References [54, 61] provide a detailed description of ablation modeling and the technology advances made over the past few decades. The modeling objective is to characterize the TPS response in-depth and its surface energy performance given the incoming heating conditions at the surface. Ablation modeling started in the 1950's and early 60's and involved coupling one-dimensional heat conduction calculations to heat of ablation models to calculate recession. [62, 63] Initially, these in-depth heat conduction models did not include decomposition or pyrolysis gas flow. The heat of ablation methods were simple correlation models that attempted to simplify the more detailed surface energy balance equation using a steady state ablation assumption. This model assumed that recession did not start until a specified ablation temperature

was reached.

Munson and Spindler [64] introduced thermal response modeling for the decomposition of organic resin composite materials. The density decomposition was modeled with a single Arrhenius relation. In 1963, Kratsch et al. [65] modified these equations to include a fiber-resin decomposition model and expressed some chemical parameters in terms of enthalpy. They also integrated the work done by Lester Lees [66] to treat the surface energy balance equation using the transfer coefficient approach. This formulation assumed that the heat and mass transfer coefficients were equal, and the Lewis and Prandtl numbers were equal to unity. Non-dimensional ablation rates, B', were introduced into the surface energy balance equation. Later, Kendall et al. [67] and Moyer et al. [68] modified these equations to include unequal heat and mass transfer coefficients and non-unity Lewis and Prandtl numbers. They also included the work by Goldstein [69] to describe the decomposition of organic resin composites using a three-reaction Arrhenius equation model. Modeling for the convection and generation of the pyrolysis gas within the solid was added to the in-depth energy conservation equation. The equations were also modified to account for grid motion due to surface recession.

These efforts resulted in the introduction of the Charring Material thermal response and Ablation program (CMA) [70], which was used as the leading ablation code within industry and NASA for decades. More recently, Milos and Chen [47, 71] from NASA Ames Research Center developed the Fully Implicit Ablation and Thermal response program (FIAT), based on the same theory as CMA. FIAT uses a fully implicit finite difference formulation which enhances numerical stability and convergence compared to CMA, and thus is more suitable for possible coupling to flow solver codes. Since its introduction in 1999, FIAT has become the primary analysis tool in industry and for many recent NASA missions.

1.3.2 Fully Implicit Ablation & Thermal Response Program (FIAT)

FIAT is used for the simulation of one-dimensional transient thermal energy transport in a multilayer stack of isotropic materials that can ablate from a front surface and decompose in-depth. The equations in FIAT solve the in-depth heat transfer problem and the surface energy balance problem. In-depth modeling involves solving the internal energy balance, internal decomposition and internal mass balance equations. [47] Internal energy balance is characterized using the transient thermal conduction equation with additional terms for internal radiation and pyrolysis shown in Eq. (1).

$$\rho c_p \left.\frac{\partial T}{\partial t}\right|_x = \frac{\partial}{\partial x}\left(\kappa \frac{\partial T}{\partial x} - q_R\right)_t + \left(h_g - \bar{h}\right)\left.\frac{\partial \rho}{\partial t}\right|_y + \dot{s}\rho c_P \left.\frac{\partial T}{\partial x}\right|_t + \dot{m}_g \left.\frac{\partial h_g}{\partial x}\right|_t \tag{1}$$

The y-coordinate is a stationary coordinate system along the thickness of the TPS material with the origin placed at the initial location of the TPS surface. The x-coordinate moves with the receding surface (shown in Figure 6). The individual terms in the above equation are: rate of storage of sensible energy, net rate of thermal conductive and radiative heat fluxes, pyrolysis energy consumption rate, convection rate of sensible energy due to coordinate system movement, and net rate of energy convected by pyrolysis gas. The pyrolysis gas enthalpy, h_g, is a function of temperature and pressure and is calculated using multi-species equilibrium solvers such as the Multi-component Ablation Thermochemistry (MAT) code [72] or the Aerotherm Chemical Equilibrium (ACE) code. [73] Specific heat and thermal conductivity are inputs in the material database and are defined as a function of temperature for both the fully virgin and char states. These properties at any given location in the pyrolysis zone are calculated using a linear density interpolation of the virgin and char properties as shown in Eq. (2).

$$c_p = \tau c_{pv} + (1 - \tau)\, c_{pc} \tag{2}$$

The weight variable, τ, is the mass fraction of the virgin material and is defined

using Eq. (3) while the partial heat of charring, $\bar{h}$, is defined using Eq. (4).

$$\tau = (1 - \rho_c/\rho)(1 - \rho_c/\rho_v) \tag{3}$$

$$\bar{h} = \frac{\rho_v h_v - \rho_c h_c}{\rho_v - \rho_c} \tag{4}$$

Internal decomposition of the material is characterized using a three-component model. The resin filler is assumed to contain two components (A, B) while the third component (C) is the reinforcing material. The density of the material at any given time is given by Eq. (5).

$$\rho = (1 - \phi)\left[\Gamma\left(\rho_A + \rho_B\right) + (1 - \Gamma)\,\rho_C\right] \tag{5}$$

Variable Γ is the specified volume fraction of resin while ϕ is the porosity for the material. Each component can decompose independently according to an Arrhenius-type reaction model as described in Eq. (6). Parameters B_i, E_i and Ψ_i describe the reaction for each component and are determined via the curve fitting of the data obtained from Thermo Gravimetric Analysis (TGA) testing.

$$\left.\frac{\partial \rho_i}{\partial t}\right|_y = -B_i e^{-E_i/T} \rho_{vi} \left(\frac{\rho_i - \rho_{ci}}{\rho_{vi}}\right)^{\Psi_i} \quad , \quad i = A, B, C \tag{6}$$

Internal mass balance accounts for the convection of pyrolysis gas through the material generated from internal decomposition. Assuming quasi-steady one-dimensional flow, conservation of mass can be written using Eq. (7). Variable $\dot{m}_g$ is the mass flux rate of the generated pyrolysis gas which is transferred to the surface and blown into the boundary layer.

$$\frac{\partial \dot{m}_g}{\partial y} = \frac{\partial \rho}{\partial t} \tag{7}$$

The surface conditions are defined through distinct back face and front face boundary conditions. The back-face boundary can be specified as a known temperature history or using a fluid convection boundary condition. Often in TPS design, an insulated boundary condition is used for the back-face. There are multiple options for

the front-face boundary condition. It can be set simply to a known temperature history or defined as a non-ablating surface with incoming convective and radiative heat flux balanced by reradiation. Often, for ablative materials, a more complex Surface Energy Balance (SEB) is used that accounts for the chemical reactions occurring at the surface during ablation. The SEB employed in FIAT is a transfer coefficient type and can be written using Eq. (8), assuming equal diffusion coefficients ($C_M = C_h$).

$$\begin{aligned} \rho_e u_e C_h (H_r - h_w) + \dot{m}_g h_g + \dot{m}_c h_c - (\dot{m}_c + \dot{m}_g)\, h_w \\ + \alpha_w q_{rad} - F\sigma\epsilon_w (T_w^4 - T_\infty^4) - q_{cond} = 0 \end{aligned} \tag{8}$$

In this equation, C_h is the Stanton number. The term $\rho_e u_e C_h$ is the convective heat transfer coefficient denoted with the symbol C_H (input to FIAT from flow solvers) while H_r is the recovery enthalpy. Figure 7 provides a schematic showing the physical phenomena at the surface that are modeled in the SEB equation. The black line represents the receding surface of the material. The first term in the above equation

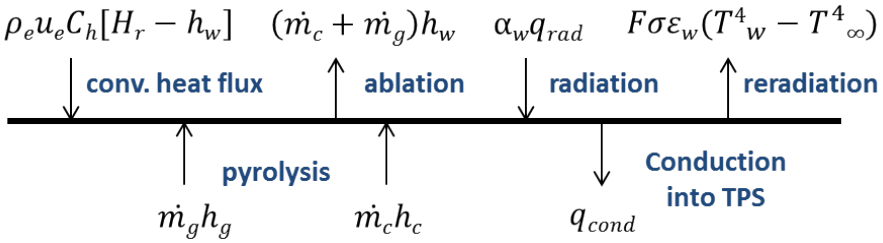

Figure 7: Schematic of different thermal terms in FIAT SEB equation.

represents the sensible convective heat flux. The sum of the second, third and fourth terms define the total chemical energy at the surface due to the ablation products and pyrolysis gas. The fifth and sixth terms are the incoming radiative heat flux absorbed by the material and the reradiation to the environment. The last term in Eq. (8) represents the rate of heat conduction into the TPS material. This equation can be rewritten as Eq. (9) by combining some terms and defining the dimensionless

mass blowing rates, B', shown in Eq. (10).

$$\begin{aligned}\rho_e u_e C_h (H_r - (1 + B')\, h_w) + \dot{m}_g h_g + \dot{m}_c h_c \\ + \alpha_w q_{rad} - F\sigma\epsilon_w (T_w^4 - T_\infty^4) - q_{cond} = 0\end{aligned} \tag{9}$$

$$B' = B'_g + B'_c = \frac{\dot{m}_g + \dot{m}_c}{\rho_e u_e C_M} \tag{10}$$

As mentioned before, the blowing of pyrolysis gas into the boundary layer results in the reduction of incoming convective heating due to the transpiration effect. A simple engineering model, shown in Eq. (11), is used within FIAT to reduce the heat transfer Stanton number calculated by flow solvers. [74] The variable λ is the blowing correction parameter which is normally taken to be 0.5 for laminar flow and between 0.2 and 0.4 for turbulent flow. C_{h1} is the unblown heat transfer Stanton number predicted by flow solvers, while C_h is the heat transfer Stanton number corrected for blowing effects.

$$\frac{C_h}{C_{h1}} = \frac{\ln(1 + 2\lambda B')}{2\lambda B'} \tag{11}$$

FIAT operates using three input files that provide the run settings, initial conditions, back-face boundary conditions, the front-face heating environment and the material database. For each material in the TPS stack-up, the material database includes virgin and char densities for each component, the volume fraction of resin, porosity, decomposition kinetics coefficients, thermophysical properties as function of temperature and pressure (char and virgin specific heat, thermal conductivity and emissivity), pyrolysis gas enthalpy and B' tables calculated externally using a multi-species equilibrium solver such as MAT or ACE. Given the composition of the boundary layer gas, pyrolysis gas, surface char and thermodynamic data, these equilibrium solvers create tables which relate T_w and h_w to P, B'_g and B'_c. Each entry in a B' table represents a chemical solution to a specific ablation problem. At each time step in a FIAT solution, P, $\rho_e u_e C_h$, H_r and T_∞ are known from the input environment and B'_g is calculated from the computed $\dot{m}_g$. The tables are iteratively interpolated

using P and B'_g to find the values of B'_c and associated T_w and h_w that result in the convergence of the SEB equation. This equation and the internal heat transfer equations are strongly coupled and are solved implicitly within FIAT. The grid can be manually imported or automatically generated. For problems with ablation, the computational grid is compressed to account for surface recession.

1.3.3 Advanced Modeling Efforts

FIAT has been successfully used for many NASA missions and is currently the standard tool in industry. However, some of the simplifying assumptions used in FIAT can add uncertainty to its prediction of recession and thermal response. There is extensive research within the ablation community for higher-fidelity methods that rely on fewer assumptions. Some models employ the same theories as CMA and FIAT while adding new equations to relax assumptions used in FIAT. Others have tried to look at the ablation problem with new approaches and theories. Lachaud et al. [75] provide a summary of more than 25 ablation solvers that are currently in use and discuss the main modeling differences between them. Laub [76] also gives a review of current and future modeling enhancements and efforts and discusses some of the issues hindering full validation of the more advanced approaches.

Milos and Chen have developed two-dimensional (TITAN) and three-dimensional (3dFIAT) [77, 78] versions of FIAT that more accurately model cross flow or multi-dimensional material property variations. These multi-dimensional codes allow the analysis of the entire vehicle unlike the point-analysis approach used by FIAT. Furthermore, heatshield features such as penetrations or highly curved areas are not one-dimensional in nature and their analysis requires multi-dimensional capability. These added features and the higher accuracy come at a cost of computational resources and lower stability. Dec and Braun [54, 79] have developed a three-dimensional ablation and thermal response code using the finite element method. Finite element methods

may be better-suited for three-dimensional analysis and complex geometries and are more compatible with finite element discretization used in modern design and analysis tools. Unlike FIAT which makes an equilibrium assumption for the in-depth pressure, these techniques use Darcy's Law to model the flow of the pyrolysis gas through the ablative material obtaining a better prediction of the in-depth pore pressure due to pyrolysis. Reference [54] also solves the equations for linear elasticity which allow simultaneous calculation of thermal stress in addition to thermal response.

Other research advances include adding models to calculate the surface thermochemical ablation as a part of the thermal response code, eliminating the use of B' tables. This has been implemented in a few ablation tools [80] and the most recent versions of FIAT and TITAN. There has also been extensive effort to model pyrolysis gas in more detail by adding gas-species conservation equations and using finite-rate reaction kinetics. [80, 81] The pyrolysis gas movement through the porous material has been modeled using simplifications of the volume-averaged momentum conservation equation (Darcy's law, Klinkenberg and Forchheimer corrections). [81, 82] The modeling of surface ablation chemistry using non-equilibrium finite-rate reaction kinetics has been also attempted; [48, 83] however, the decomposition and reaction rate data required for the validation of these models is scarce. Other research areas involve the inclusion of models that characterize surface catalysis, roughness and mass injection effects in the thermal response codes. Coupling with flow-solvers has also been studied to some extent. [48] Mansour et al. [81] have developed the high-fidelity Charring Ablator Thermal response (CAT) code that consists of species conservation equations in addition to the mass and energy conservation equations. It is tightly coupled to a chemistry model that enables use of equilibrium as well as finite-rate chemistry.

Lachaud et al. [84] have recently developed a multi-scale approach to model the ablation of porous materials. Unlike most other tools that treat recession as a surface

process, they allow the diffusion of boundary layer species within the char layer and allow ablation to occur in volume. This model was able to explain the unexpected drop in char-layer density observed in the post-flight analysis of Stardust sample return capsule PICA heatshield. [60] While these higher-fidelity models show great promise and provide a more accurate characterization of the physics of the problem, more sophisticated experiments and diagnostic techniques are required to acquire the data needed for their validation.

1.3.4 Ground-Based Testing

While there have been many advances in ablation and pyrolysis modeling efforts over the past decades, experimental testing has been required to provide material property and pyrolysis reaction rate data. In addition to providing input parameters for thermal modeling, experimental methods have been used for many years to calibrate or validate these models and qualify the TPS material for use in a flight vehicle.

Many different lab tests are performed to characterize the material thermophysical properties and its pyrolysis performance. Reference [85] provides a summary of some of these lab tests. TGA testing measures the residual mass fraction of the TPS material as a function of temperature at low temperature rise rates. The obtained data are fit to determine the decomposition kinetic constants for the Arrhenius reaction model. Digital Scanning Calorimeter (DSC) experiments are also performed to provide heat of reaction for pyrolysis as a function of temperature. The elemental composition of the virgin material is measured using mass spectrometry. Elemental composition of the char is determined from the known constituents and the char yield data. Heat of combustion of the virgin material is measured and the heat of formation is derived. For the char, the heat of formation is derived from the known constituents and other existing data.

For pyrolysis gas, the elemental composition of the gas is derived, and the pyrolysis gas enthalpy is determined using a combination of thermochemical equilibrium models and measured heat of pyrolysis data. The virgin specific heat and thermal conductivity of the material are measured in specialized lab tests as function of temperature. The specific heat of char is derived from known compositions using method of mixtures. The optical properties of the char can be also determined experimentally. The char thermal conductivity is one of the most uncertain material properties. It can be measured at lower temperatures; however for higher temperatures, it is often determined using thermocouple data from arc jet testing.

There are no ground facilities that can produce all aspects of the flight environment, specifically Mars-like environments. Radiative facilities (radiant lamps, lasers), combustion facilities and arc plasma facilities have been traditionally used for testing of ablative TPS materials. [86] Arc jet facilities are the most versatile and have been used for the testing of candidate TPS material for planetary entry for over 50 years. [87] Material coupons are instrumented with thermocouples and are exposed to the high-heating nozzle exhaust environment of the arc jet. These facilities can produce a wide range of flight-like heat flux, enthalpy, pressure and shear for long durations; however, they can not simultaneously match all these conditions with flight. Some arc jets can provide low enthalpy, high pressure and high heat flux conditions while others can simulate high enthalpy, low pressure and low-moderate heat flux environments. [61] Figure 8 illustrates pre-test and post-test pictures of PICA samples containing MISP plugs that were used in MSL qualification arc jet testing. A picture of a PICA coupon being tested in the arc jet environment is also shown.

Even though arc jets are the most flexible TPS testing facilities, they still have many limitations. Currently there are no arc jet facilities in the United States that can operate on CO_2 and create conditions similar to the Mars atmosphere. Arc jets are also limited by the sample size and only sub-scale material coupons can be

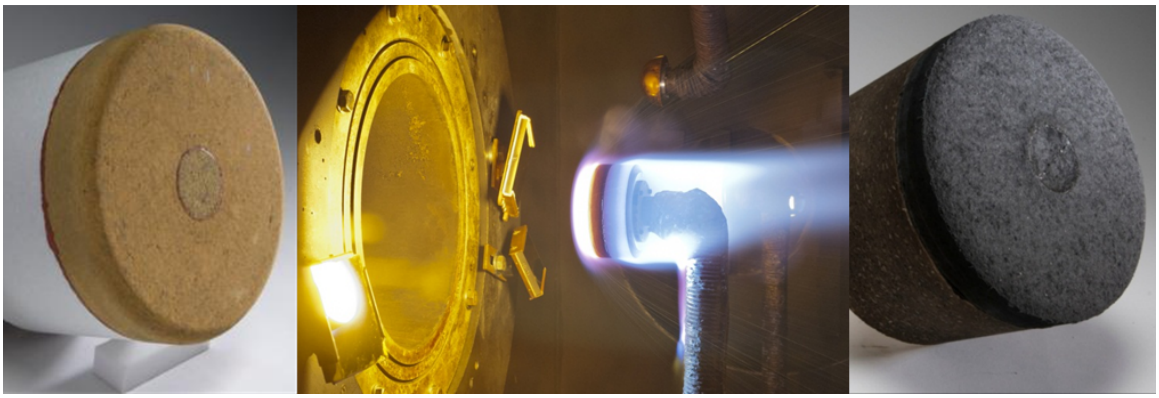

Figure 8: MSL qualification arc jet testing for PICA coupons containing MISP plugs.

tested. Furthermore, combined effects of radiative and convecting heating can not be investigated. Time-varying trajectory-like conditions are also difficult to simulate in arc jets. The freestream conditions of the nozzle exhaust are not always well-characterized and there is often significant uncertainty with the measured enthalpy and heat flux and their distribution along the testing coupon.

Radiative facilities are another class of TPS ground testing techniques. The Sandia solar tower [88] can produce up to 200 W/cm^2 of concentrated solar radiation on very large models. However, this facility is only appropriate for system level testing because flight-like conditions are not matched due to a lack of flow. The Laser-Hardened Materials Evaluation Laboratory (LHMEL) testing facility [89] can be also used to expose a defined spot size of material to very high laser-produced heat fluxes. Testing can be done in CO_2 environments; however, because there is no flow, the convective conditions of the reentry can not be simulated. While ground facilities can provide useful information, flight data is ultimately the best experimental data for code calibration and validation. Relevant flight testing in Earth's atmosphere or instrumentation on planetary entry missions remains the gold standard for reducing the substantial uncertainties in our aerothermal and TPS response models.

1.4 Heatshield Flight Data

1.4.1 Past Flight Data

While MEDLI represents the most Mars aeroheating data ever returned by a planetary mission, a few other entry missions at Mars, Jupiter, Venus and Earth provided ablative TPS temperature data or other means for the assessment of their heatshield performances. However, most of the post flight analyses were concerned mainly with a direct comparison of the model predictions to the temperature data for the purpose of code validation. An inverse estimation analysis, such as the work proposed in this document, was not performed for these entry missions.

1.4.1.1 Mars Entry Data

Viking I and II landers employed 70 degree aeroshells with SLA-561V forebody heatshields. They entered the Martian atmosphere after orbit insertion partly due to concerns about the severity of their heating environment. No forebody TPS thermocouples were used for these missions; however, each vehicle was equipped with two surface-mounted backshell thermocouples on the fiberglass inner cone and the aluminum skin of the outer cone. Pre-flight estimates predicted the backshell heat flux to be about 3% of the forebody nose laminar value while the flight data indicated heating as high as 5%. [90] The surface heat flux was derived from the thermocouple measurements based on analytical techniques which made simplifying assumptions about the thickness and thermal response of the backshell material. [91] Early analysis suggested that the high level of heating and slope changes in the data was evidence for turbulent transition on the base. Figure 9 from Ref. [91] illustrates the observed slope change in the derived heat flux for Viking I. The aftbody heat flux is shown as a percentage of the computed stagnation heat flux.

Recently, Edquist et al. [92] performed a more detailed analysis and obtained Navier-Stokes solutions of the wake flowfield with LAURA and DPLR CFD codes.

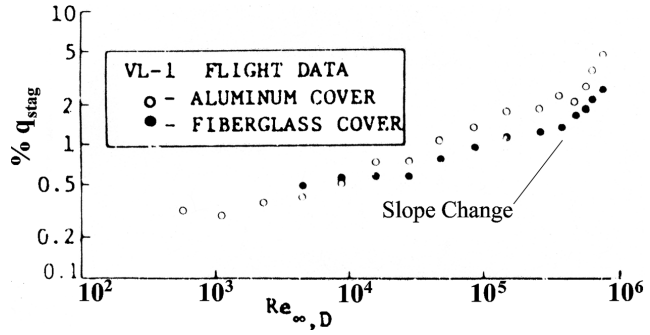

Figure 9: Viking I aftbody heat flux derived from flight temperature data.

The surface heat flux was derived from the flight temperature data using a one-dimensional heat balance formulation which included estimates of material properties, internal heat source and trajectory uncertainties. Based on these uncertainties, lower and upper bounds were obtained for the derived heat flux. The CFD simulations predicted that the wake flowfield was unsteady. Figure 10 from Ref. [92] shows that the averaged CFD-calculated heat flux under predicts the heat flux inferred from flight data. This study also showed that the slope change in the normalized heat flux (observed in the previous study) might not be due to turbulent transition. The slope change could have been exaggerated by the normalization of a rising aftbody heat flux with a declining stagnation point heat flux.

The Mars Pathfinder entry vehicle was a 70 degree sphere-cone with a SLA-561V heatshield equipped with six forebody and three aftbody thermocouples at different locations and depths. Milos et al. [5] performed aerothermal and TPS response analyses for the entry vehicle and compared their results with flight data. In general, the data indicated a good qualitative match with the analysis except at the bondline thermocouples. More recently, Mahzari et al. [93] performed an updated aerothermal and TPS analysis for the entry vehicle, and used inverse methods to reconstruct surface heating profiles for stagnation and shoulder locations that resulted in a much closer match with the data. The details of the Pathfinder instrumentation and the conducted inverse analysis are explained in Chapter 3.

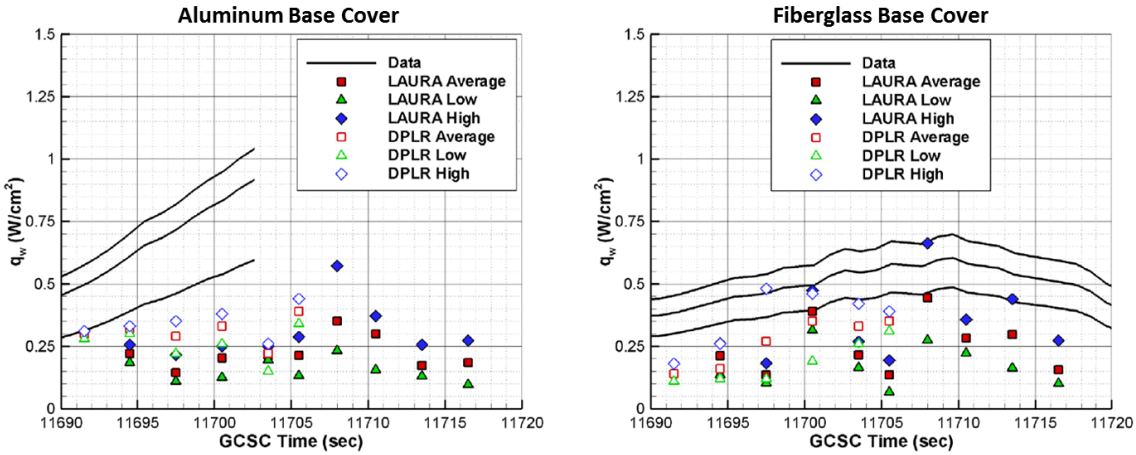

Figure 10: Computed Viking I aftbody heat flux compared to flight-derived values.

Viking and Pathfinder represented the only Mars entry aeroheating flight data. Prior to the work proposed here, a comprehensive inverse analysis of this data was not performed. The previous analyses focused mainly on a direct comparison between model predictions and data, or using simple techniques to analytically derive heat flux from measured temperatures. The application of inverse methods will provide a more accurate reconstruction of the aerothermal and TPS performance.

1.4.1.2 Venus and Jupiter Entry Data

The Pioneer Venus program included four entry probes that descended through the Venusian atmosphere along different trajectories. They were 45 degree sphere-cones with carbon phenolic heatshields. Each probe was equipped with two subsurface forebody thermocouples. [94] These thermocouples were located at the nose and along the conical frustum. The probes were expected to experience high convective and radiative heat rates in the excess of 7,000 W/cm^2. Wakefield and Pitt compared the flight data with temperature calculations from the CMA code based on predicted heating conditions (shown in Figure 11). For the day probe, the predicted and measured temperature rise times were offset by several seconds. This is deemed to be due to the uncertainty in the vehicle's trajectory which was one of the main challenges

of the post-flight analysis. Not considering the time offset, the magnitude and the curvature of the analytical predictions matched the flight data very well. For the night probe, the shoulder predictions agreed well with the thermocouple data but the nose predictions were conservative. [95]

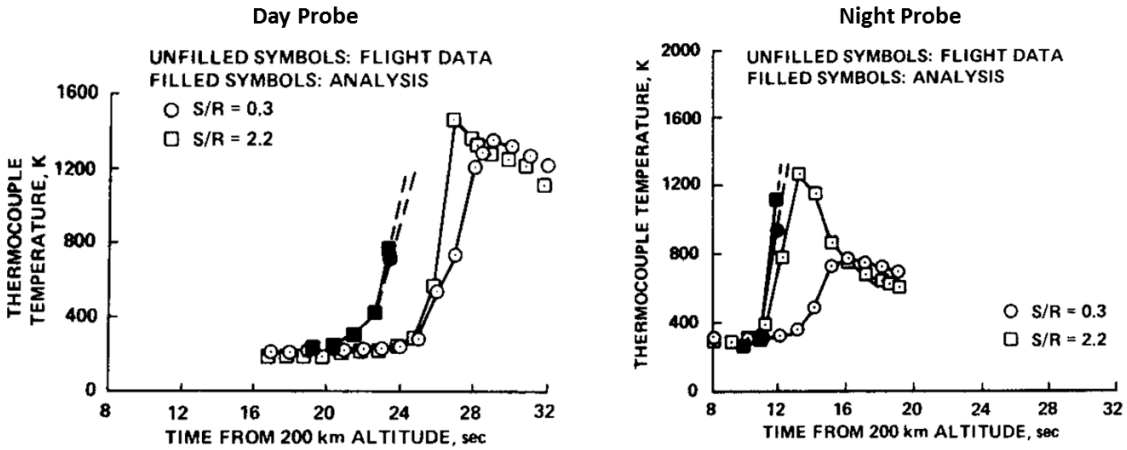

Figure 11: Analytical predictions compared with flight data for Pioneer Venus probes.

The Jupiter Galileo probe was also a 45 degree sphere-cone and the heatshield was made of carbon phenolic. Galileo entered the Jovian atmosphere at a velocity of 47 km/s and experienced the most severe heating environment by any planetary entry capsule. The vehicle was equipped with ten Analog Resistance Ablation Detector (ARAD) sensors that were designed to measure the TPS recession. Four resistance thermometers, two on the forebody and two on the aftbody, were also placed inside the structure which provided temperature measurements. [56] The temperature measurements were recorded every 8 seconds, and six samples were stored in memory overwriting previous measurements. The temperature acquisition was designed to stop after the end of recession data acquisition; however, a software problem resulted in the temperature data acquisition to continue, overwriting the data from the early phase of the entry.

Since the thermometers were inside the structure, they were not strongly affected by surface heating. The nose cap thermometer did not show any response because

the heat pulse was not expected to penetrate the heatshield thickness within the acquisition period. The frustum thermometer showed a 30 K temperature rise. Milos et al. used a combination of the ablation sensor measurements, FIAT and a one-dimensional heat conduction model for the thermometer to show that the recession and temperature data were consistent with 13,400 W/cm^2 peak heating at the frustum.

The ablation sensor performed poorly and an accurate transient heatshield shape analysis was not possible due to the oscillations and noise in the returned ARAD data. Milos et al. performed a direct comparison of the analytical predictions and the ablation sensor data. The main conclusion was that while the stagnation point recession was less than predicted, ablation at the shoulder was significantly greater than predicted. [96] The reasons for this discrepancy are still not known.

1.4.1.3 Earth Entry Data

The Genesis sample return capsule entered the Earth atmosphere in 2004. The entry vehicle was protected with a carbon-carbon heatshield. The parachute failed to open during the descent which resulted in the spacecraft crash landing in Utah. The aeroshell was damaged significantly; however, a portion of the heatshield was undamaged and recovered for analysis. [97] Figure 12 shows that the heatshield region downstream of the forebody attachment points exhibited a more intense charring and streak patterns which are indicative of higher heating. Tang et al. [98] performed laminar and turbulent CFD simulations for the Genesis capsule and concluded that the higher heating in these regions may be caused by turbulent transition.

The Stardust sample return capsule entered the Earth atmosphere in 2008 and was protected with a PICA heatshield. Even though there was no instrumentations in the TPS, the heatshield was recovered (shown in Figure 12) and samples from its nose, flank and shoulder were analyzed in the lab. [60] Different tests were performed to

examine the TPS density profile, surface emissivity profile and recession. The results showed that analytical models tend to overpredict recession which can be partly explained by the equilibrium assumption used in those models. The PICA material density profile generally agreed with model predictions except an unexpected observed drop in the char layer. This can be explained if recession is not treated only as a surface phenomenon and is modeled as a volume process. [84]

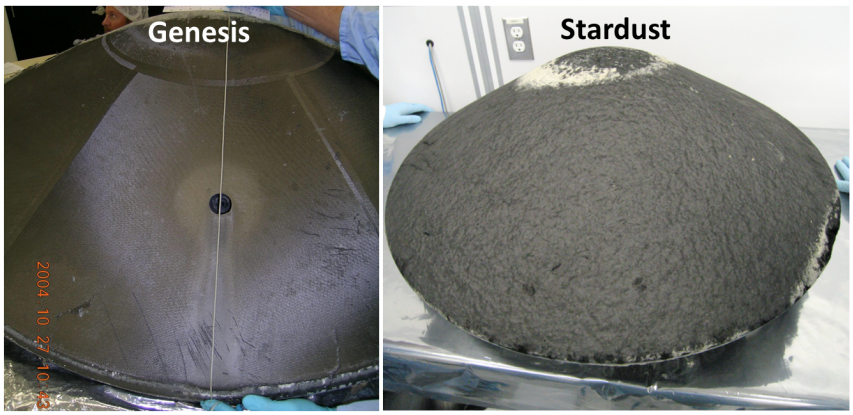

Figure 12: Recovered Genesis and Stardust capsule heatshields.

In addition to these missions, there have been numerous instances of flight data returned by Earth entry vehicles. Some examples are calorimeters and radiometers from the Mercury, Gemini and Apollo 1-3, 4 and 6 missions. Fire II was equipped with forebody calorimeters, radiometers and aftbody thermocouples. Early Space Shuttle missions included heat transfer sensors. Recently, infrared imagery of the Space Shuttle tiles during hypersonic entry was successfully attempted and provided useful data regarding turbulent transition and roughness effects. [99] Other examples include projects Reentry F, MIRKA and ARD. [4] In some instances, the heatshields were recovered for further analysis. A discussion of all the analysis done for these missions is beyond the scope of this work; however, the majority of data analysis work included direct comparisons to investigate model validity. A comprehensive inverse reconstruction, such as the work proposed here for the MEDLI dataset, was

not performed for those datasets. Reference [4] provides a complete review of the data related to afterbody heating predictions.

1.4.2 MEDLI

The MSL entry vehicle landed on Mars in August 2012. It had a 4.5 meter PICA heatshield which was equipped with forebody temperature and pressure sensors called MEDLI. [8] MEDLI provided more TPS data than all the data from Viking and Pathfinder missions combined. MEDLI consists of seven pressure ports and seven PICA plugs at different locations on the MSL heatshield. The suite consists of three subsystems: MISP temperature/isotherm sensors, MEADS pressure sensors, and Sensor Support Electronics (SSE). MISP sensors are installed into PICA plugs that are flush-mounted to the flight heatshield. The MISP plugs (Figure 13, T labels) are strategically placed to cover a broad range of heat flux environments, while the MEADS locations (Figure 13, P labels) are concentrated in the higher pressure and lower heat flux region near the stagnation point and the nose region. The data from the MISP sensors are the focus of this research.

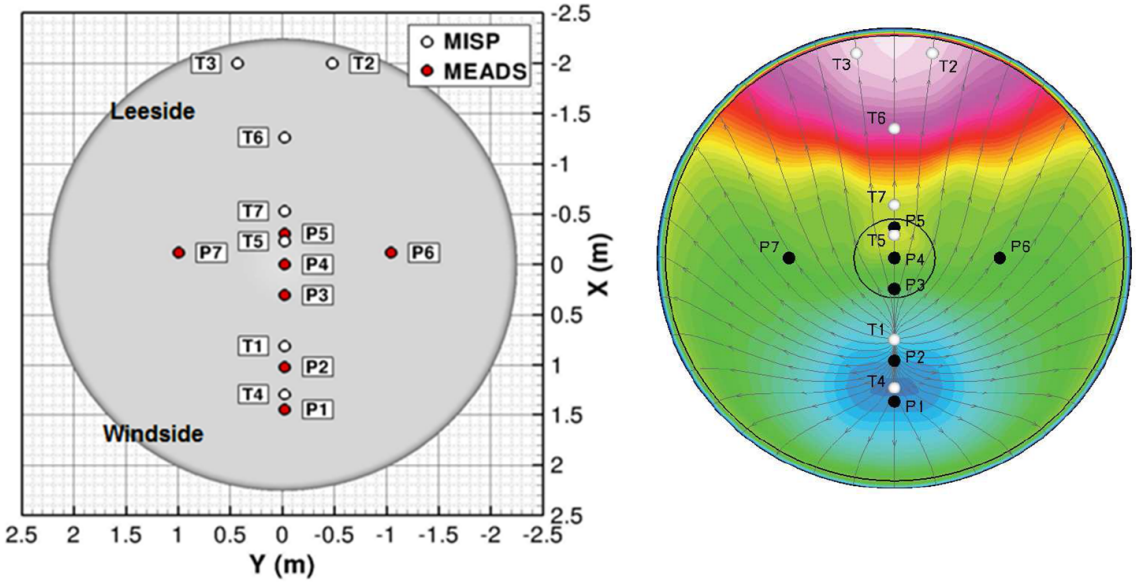

Figure 13: Location of MEDLI sensors on MSL heatshield.

Each MISP plug is 33 mm in diameter with a total depth of 29 mm, and contains four type-K U-shaped thermocouples. The thermocouples are at nominal design depths of 2.54, 5.08, 11.43, and 17.78 mm (0.10, 0.20, 0.45, 0.70 inch) from the surface of the plug. X-ray measured thermocouple depths are shown in Table 1. The top two thermocouples are intended primarily for aerothermodynamic reconstruction, while the two deeper thermocouples are primarily intended for material property reconstruction. The science measurement range requirement for each thermocouple is 100 to 1300 K with an accuracy of $\pm$ 2.2 K or 2.0% below 273 K and $\pm$ 1.1 K or 0.4% above 273 K. The top thermocouple is sampled at 8 Hz while the deeper thermocouples are sampled at 1 or 2 Hz depending on the location. The bottom two thermocouples at plugs 5 and 7 are not wired due to data channel limitations. Figure 14 shows a schematic and an image of a finished MISP plug. [9]

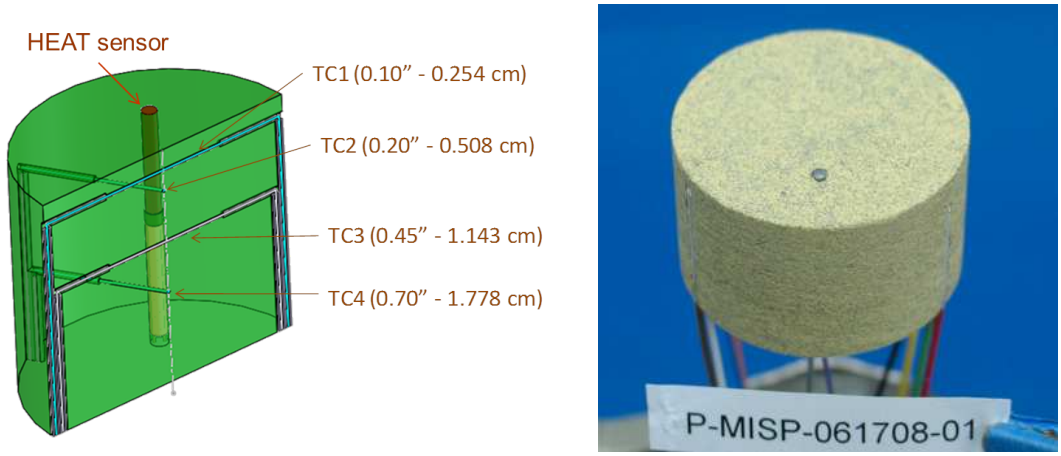

Figure 14: Schematic and image of finished MISP plug.

Table 1: X-ray measured depths of MISP plugs thermocouples.

	Ideal (in)	Plug 1	Plug 2	Plug 3	Plug 4	Plug 5	Plug 6	Plug 7
TC1	0.100	0.104	0.106	0.103	0.097	0.099	0.108	0.094
TC2	0.200	0.200	0.203	0.193	0.212	0.192	0.203	0.193
TC3	0.450	0.452	0.456	0.456	0.446	0.461	0.460	0.442
TC4	0.700	0.704	0.700	0.693	0.706	0.703	0.695	0.699

Each MISP plug also contains an isotherm sensor called Hollow aErothermal Ablation and Temperature (HEAT). [100, 101] It is an improved version of a similar sensor that was used for the Galileo entry probe to determine surface recession.[96] However, at the lower heat rates experienced during Martian entry, it is not expected to provide any information on recession. The sensor elements are conductive, so as the char layer-virgin material interface advances, these elements become shorter and the voltage output decreases. The voltage measurements can be correlated with the sensor length which can then be correlated with char depth. Figure 15 shows a schematic and an image of a finished HEAT sensor. [101] The MSL data analysis study presented in this document focuses mainly on the thermocouple data.

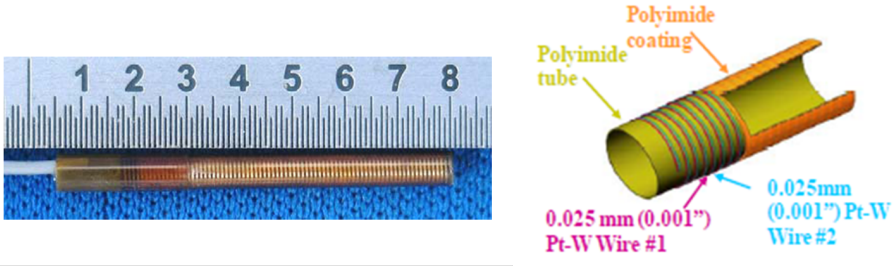

Figure 15: Schematic and image of finished HEAT sensor.

Table 2: MISP science objectives.

Objective	**Accuracy**
Reconstruct aeroheating	$\pm$ 30 W/cm^2
Determine leeside turbulent heating levels	$\pm$ 30 W/cm^2
Determine time of boundary layer transition onset	2 seconds
Determine presence, if any, of stagnation point heating augmentation	$\pm$ 30 W/cm^2
Measure subsurface material temperature response	$\pm$ 12%
Determine total TPS recession	$\pm$ 0.635 cm
Measure depth of isotherm in TPS	720°C $\pm$ 80°C and $\pm$ 0.8 mm

Table 2 shows a list of the MISP instrument science objectives as defined by the MEDLI project. [102] Reconstruction of surface heating will allow investigation of turbulent and catalytic heating augmentation, onset of transition and stagnation point

heating augmentation. The isotherm sensor data is expected to indicate information about TPS total recession.

1.5 Summary of Contributions

The objective of this thesis is to develop an inverse estimation methodology to improve knowledge extracted from aerothermal and TPS data. Significant uncertainty remains in both the surface heating predicted by aerothermal models and TPS material performance. Application of the developed methodology will allow accurate estimation of material properties and reconstruction of the complete surface heating profile from experimental data. Sometimes, estimation parameters are constant in time while other parameters could be time-dependent. When parameters are constant, the inverse problem is a parameter estimation problem. Conversely, if the estimation parameters are time-dependent the problem becomes a function estimation problem. These problems have their own unique challenges and are most effectively treated separately. Therefore, the inverse methodology presented in this thesis is divided into two sections: a multi-parameter estimation framework and a surface heating function estimation framework.

The multi-parameter estimation framework focuses on estimation of multiple constant parameters such as material properties or constant arc jet heating parameters from TPS experimental data. The simultaneous estimation of these parameters is not straightforward. From a large set of possible material and heating parameters, one must first identify a smaller subset that contribute the majority of the uncertainty in TPS response prediction. Some of the input parameters might also be correlated and not simultaneously observable from the data. Therefore, one must also investigate the degree of linear dependency between the parameters prior to performing an inverse estimation. Data quality is another area of concern. Errors in the data can make the estimation process unstable and lead to incorrect estimation results. Consequently, it

is crucial that the framework developed identifies what parameters can be estimated from the experimental data and what range of measurements should be used.

The surface heating function estimation framework provides a means to perform time-dependent estimation of the complete surface heating profile from TPS subsurface temperature data. This framework is appropriate for heating reconstruction in a flight application where surface properties vary in time along the trajectory. Function estimation problems are ill-posed. Small errors in the data or model can cause significant oscillation in the estimated heating profile. Regularization techniques are used to alleviate these oscillations. The framework developed in this work introduces techniques and guidelines for accurate reconstruction of surface heating.

When subsurface temperature data is available at multiple depths, a thermocouple (TC) driver approach can be used to decouple the surface heating problem from the in-depth material response problem. This enables application of both frameworks to the complete dataset to estimate both the material properties and time-dependent surface heating. First, the surface heating profile is estimated from the shallowest TC data using the function estimation framework. Then, the data from the shallowest TC is used as the truth boundary conditions and the heat conduction problem is solved for the TPS block below that TC. In this manner, knowledge of surface heating conditions are not required for the in-depth heat transfer problem. This allows application of the multi-parameter estimation framework to estimate material properties from the remaining deeper TC data.

In this thesis, the multi-parameter estimation framework is first applied to an arc jet dataset. Next, the surface heating function estimation framework is applied to Mars Science Laboratory (MSL) simulated data and Mars Pathfinder flight data. Finally, both frameworks are applied to MSL flight data. The work presented in this thesis is motivated by the goals of the MSL aerothermal environment and heatshield reconstruction efforts. However, the scope of this work is not limited to MSL. The

inverse methodology and tools developed for this purpose can be also applied to other flight projects and ground testing data. The contributions of the work proposed herein are summarized below:

(1) Development of a Multi-parameter Estimation Framework for Application to Atmospheric Entry TPS Experimental Data: This framework employs nominal, uncertainty and sensitivity analyses before inverse estimation to assess the quality of the data, identify the parameters that contribute the most to prediction uncertainty and select the parameters that are simultaneously observable from the data. These analyses provide the prerequisite information for a successful and accurate inverse analysis. Material properties and aerothermal constants are estimated with this framework. The framework is validated with the use of MSL-related arc jet data. This multi-parameter estimation approach provides better results and more flexibility than traditional methods. This framework is also employed to estimate PICA material properties from MSL data using a TC driver approach.

(2) Development of a Surface Heating Function Estimation Framework for Application to Atmospheric Entry TPS Temperature Data: Techniques and guidelines are introduced for estimation of time-dependent surface heating from subsurface TPS temperature data. Traditionally, the nominal surface heating profile was simply scaled to provide a reasonable qualitative match with flight data. The analysis presented here allows a more accurate estimation of the time-dependent surface heating profile. This framework is validated by application to simulate data. The effect of model and measurement errors on the accuracy of surface heating estimation is investigated. Previous inverse analyses of this kind were concerned with simpler materials and heating conditions. This investigation is the first to develop and apply these techniques specifically for a relevant ablative, pyrolyzing TPS at flight conditions.

(3) First Application of Inverse Techniques to Reconstruct a Mars Entry Vehicle's Aerothermal Environment and TPS Material Response from Heatshield Flight Data: Investigation of TPS flight data has been traditionally performed in a direct fashion, where the model predictions are directly compared to the flight data. In this investigation, inverse methods are used to reconstruct surface heating and TPS material properties from Mars flight data. This is completed for both the Mars Pathfinder and MSL missions. In the case of Pathfinder, the flight thermocouples were only available at one depth. As such, only the surface heating profile is estimated. For the MSL vehicle, the TC driver approach is used to estimate both TPS material response and surface heating from flight data.

(4) Investigation and Improvement of TPS Design Margin Policies: Conservative margins have been used in TPS design due to uncertainties in the aerothermal environment and TPS material response. These high margins significantly affect the choice of TPS material and heatshield mass. This work will examine how the findings from MSL data may be used to modify these design margin policies.

1.6 Thesis Outline

Chapter 2 introduces the estimation methodology developed in this thesis for application to aeroheating and TPS experimental data. Both the multi-parameter and surface heating function estimation frameworks are described. **Chapter 3** discusses the application of the multi-parameter estimation framework to an arc jet dataset. **Chapter 4** applies the surface heating function estimation framework to simulated MSL data and Mars Pathfinder flight data. In **Chapter 5**, a detailed inverse analysis of MSL flight dataset is provided followed by a discussion of possible improvements to TPS design margin policy in the light of MSL data. Finally, **Chapter 6** presents the conclusions, lessons learned and future design and placement of TPS instrumentation. Possible augmentations to the methodology are also discussed.

CHAPTER II

INVERSE ESTIMATION METHODOLOGY

2.1 Introduction

The inverse estimation tools and frameworks developed for application to aeroheating and TPS experimental data are examined in this chapter. First, the distinction between "Direct" and "Inverse" for data analysis problems relating to atmospheric entry aeroheating and TPS thermal response is discussed. Next, background on inverse heat transfer problems and their solution methods is presented. The estimation methodology presented in this work comprises of two distinct parts. The first part is a multi-parameter estimation framework developed for inverse problems where multiple constant parameters need to be estimated. This framework helps identify what parameters should be estimated and what range of the measurements should be used. This framework has application to material property estimation or arc jet problems where surface heating is not time-dependent.

The second part of the methodology is the surface heating estimation framework which is aimed at problems where the time-dependent surface heating is reconstructed from in-depth temperature data. Unlike the first part where multiple constant physical parameters need to be recovered, surface heating reconstruction often involves the estimation of one parameter as a function of time. These problems are addressed separately as they each have their own unique challenges. Finally, the last section of this chapter discusses the "TC Driver" approach which is used to decouple surface heating estimation and material property estimation problems. This approach will be most useful for application to flight data where surface heating is not known a priori.

2.2 Direct vs. Inverse Analysis

Most engineering problems are posed for direct analysis, where a physical phenomenon is studied using an analytical model. Model parameters and boundary conditions are known and the goal is to compute the system response or model outputs. In the case of TPS response modeling, the heating boundary conditions are known from aerothermal models and the parameters and material properties defining the thermal response model are also known. The goal of TPS response modeling is to predict the TPS thermal response by calculating variables such as recession or the temporal and spatial distribution of the TPS temperature. This is called the direct problem.

If measurements of a system's response are available, the problem can be approached in an inverse fashion. For these problems, the objective is to estimate the model parameters or boundary conditions from measured outputs. In the case of TPS response modeling, measurement of temperature as a function of time is available at a few locations, and the goal is to accurately estimate model parameters and boundary conditions that result in a predicted system response (temperature) that closely matches the data. This is called the inverse problem.

In the past, all planetary heatshield flight data were analyzed in the direct fashion. Figure 16 illustrates a schematic for direct data analysis. In this approach, CFD tools are used to calculate time-dependent surface heat rate based on the reconstructed flight trajectory. Next, surface heating conditions derived from CFD solutions are fed into a thermal response code such as FIAT. The heatshield in-depth temperature response is then calculated by FIAT using a set of properties previously derived for the heatshield material. The analytical temperature response at the thermocouple locations are then compared to flight temperature data. This comparison will qualitatively indicate how accurate the computational models are with respect to flight data. A small number of parameters in the material model can be modified or the calculated surface heating can be manually scaled to provide a better match

between the computational model predictions and measured temperature data. This approach assumes the computational models are accurate, providing neither a time-dependent surface heating profile nor any material properties directly derived from the flight data. Model or measurement uncertainty must be addressed separately.

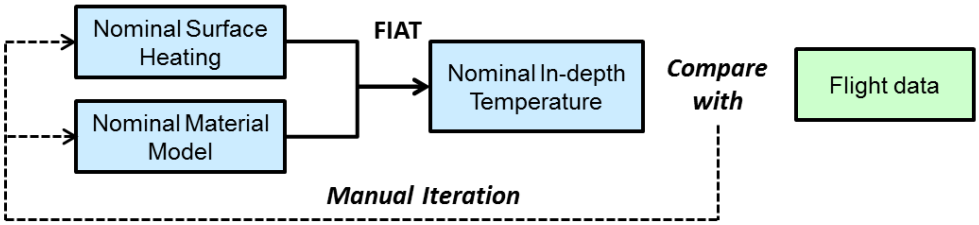

Figure 16: Direct approach for TPS data analysis problems.

Unlike the direct approach, inverse data analysis enables the estimation of the surface heating profile and material properties directly from the flight data. Figure 17 illustrates a schematic for inverse data analysis. The CFD-calculated surface heating and the nominal material model are solely used as initial guesses for the inverse methods. The surface heating solution and/or material properties that provide the closest match between the computational model predictions and flight temperature data are estimated. Model and measurement errors can be easily integrated within the estimation loop to also calculate the uncertainty associated with the heating or property estimates. Using an inverse approach, the complete time-dependent functional shape of the surface heating profile can be estimated in addition to multiple material properties.

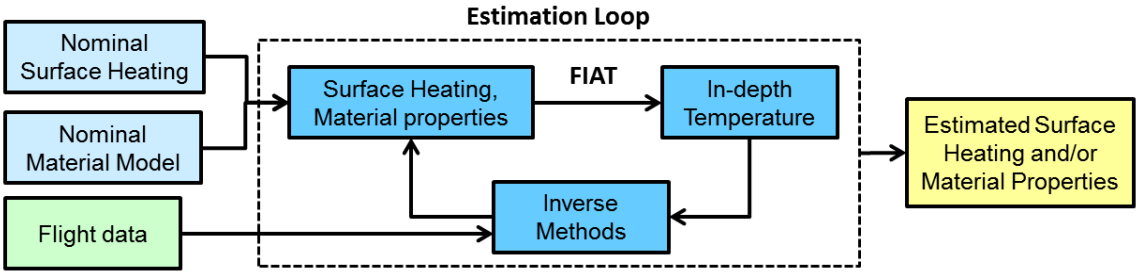

Figure 17: Inverse approach for TPS data analysis problems.

Inverse problems are mathematically ill-posed, meaning that the conditions of solution existence, uniqueness and stability are not generally satisfied with respect to the input data. The solution existence problem stems from the fact that there may be no parameter set that exactly fits the data. This can occur in practice when the mathematical model of the system physics is approximate or when the data contains significant errors. Furthermore, there is significant uncertainty in many model parameters and boundary conditions. In addition, in many physical problems, some input parameters are linearly dependent and have similar effects on the outputs. This correlation results in those parameters not being simultaneously observable from measurements. Finally, the estimation of a time-dependent boundary condition without any information on its functional form can be unstable due to the fact that many dependent parameters have to be estimated. Such instabilities may result in large oscillations in the estimated boundary conditions.

These challenges have motivated the development of optimization and regularization methods for the solution of inverse problems. In this work, estimation frameworks are developed for application to TPS data analysis problems for both material property parameter estimation and surface heating function estimation.

2.3 Inverse Problems Background

During the past decades, extensive research has been conducted on the solution of inverse problems. These problems are encountered in data analysis applications in a broad range of fields such as heat transfer,[103, 104, 105, 106, 107, 108, 109] geophysics,[110] trajectory and orbit reconstruction,[111, 112, 113, 114, 115] remote sensing,[116] medical imaging,[117] mathematics and astronomy. [118] The general methods used for the solution of inverse problems in these fields are similar. However, specific solution techniques are modified from one field to another to serve the purpose of the problem being studied. Since the analysis presented here is concerned

with aerothermal modeling and ablative TPS material response, this work is focused on the class of methods used to solve Inverse Heat Transfer Problems (IHTP). For more details, the reader should consult the work by Orlande [119] which provides a survey of the methods used to solve IHTPs and current research areas.

IHTPs can be categorized in different ways. [106] They can be classified in accordance with the nature of the dominant heat transfer process: conduction, convection or radiation. For example, Inverse Heat Conduction Problems (IHCP) involve the estimation of boundary heating or thermophysical parameters from in-depth temperature measurements while the heat is transferred primarily through thermal conduction. Another classification is based on the type of parameters being estimated: boundary conditions,[104] model parameters (material properties), [103] initial conditions or geometric characteristics. Estimation of the time-dependent surface heating profile is a function estimation problem while estimation of thermophysical properties such as specific heat and thermal conductivity is a parameter estimation problem. Another classification is based upon the differential equations representing the problem: linear or nonlinear. The temperature and spatial dependence of material properties makes the heat conduction problem nonlinear. The inverse methods used for these problems can also be classified based on the time domain of the measurements used in the estimation process: whole-time domain or sequential. Other ways of classification include the dimension of the heat transfer problem (e.g., 1-D, 2-D or 3-D) and the method of solution of the direct heat transfer problem (e.g., finite difference, finite element, finite control volume, Duhamel's theorem). This investigation is concerned with nonlinear Inverse Heat Conduction Problems (IHCP) for the estimation of MSL's surface time-dependent heating boundary conditions and PICA material properties. Therefore, the MSL estimation problem described here is a combination of both function estimation and parameter estimation problems.

The estimation of surface heating from in-depth temperature is a challenging

problem because the temperature response is damped and delayed. This means that a change in the surface heating is felt by the subsurface thermocouples with lower sensitivity and with time delay. Naturally, the sensors need to be closest to the surface to minimize this problem; however, this is not always possible due to surface recession and the operating limits of thermocouples. Figure 18 shows the temperature sensitivity of in-depth thermocouples to a 10% step change in surface heating at 70 seconds as calculated by FIAT. Here, TC1 is the closest to the surface at a depth of 0.1 inch with TC2-TC4 at depths of 0.2, 0.45 and 0.7 inch. The deeper the thermocouple, the more delayed and damped its response is.

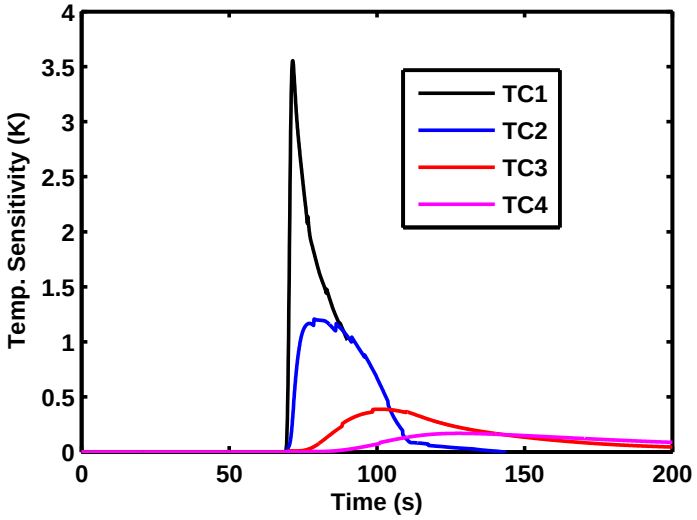

Figure 18: Subsurface temperature sensitivity of 4 thermocouples at depths of 0.1, 0.2, 0.45 and 0.7 inch to a change in surface heating at 70 s.

The main methods used for the solution of IHCPs are the whole-time domain method and the sequential function specification method. Whole-time domain methods estimate all of the parameters characterizing the time-dependent boundary condition profile at the same time using all measurements. The time-dependent heating profile is discretized and treated as multiple control points or parameters. The estimation is done by iterative minimization of an objective function S (ordinary least square), which is equal to the sum of the square of errors between the measurements

and the corresponding temperature predictions. The set of parameters that minimize this function is the solution of the inverse problem. The ordinary least-square objective function is shown in Eq. (12) in both standard and matrix forms.

$$S(\mathbf{P}) = [\mathbf{Y} - \mathbf{T}(\mathbf{P})]^T [\mathbf{Y} - \mathbf{T}(\mathbf{P})] = \sum_{i=1}^{M} (Y_i - T_i)^2 \tag{12}$$

$\mathbf{P}$ is the vector of parameters being estimated (either material properties or discretized time-dependent boundary conditions), $\mathbf{Y}$ is the thermocouple measurements in one vector, and $\mathbf{T}$ is the corresponding vector of temperature predictions by physical models. This is an ordinary least squares estimation. Other variations of this function are possible such as weighted least squares, maximum likelihood and maximum a posteriori estimation. Different methods can be used to perform the minimization for a least squares problem such as Gauss-Newton, [103, 107] Levenberg-Marquardt, [106] Box-Kanemasu [103], variations of the Conjugate Gradient method or more computationally expensive second order methods. [106] The Gauss-Newton method provides the fastest convergence of the first-order methods; however, it can be unstable.

As mentioned before, inverse problems are ill-posed and become unstable in the presence of errors and for small time steps. This results in large oscillations in the boundary condition estimates as the solution is reached. Regularization approaches are used in conjunction with the minimization scheme to make the problem better posed and more stable. Regularization has a smoothing effect on the parameter estimates. Russian mathematician Andrey Tikhonov devised a procedure for the regularization of ill-posed problems. [120, 121] His technique involves the addition of a penalty function to the ordinary least square function to alleviate oscillations in the solution. Doing this results in effectively solving a neighboring problem that has a solution close to the solution of the original problem, with the distinction that the new problem is better posed. The regularization term can take many different forms, but they all include a parameter that has to be determined to obtain a stable solution. An

alternative approach used in literature is the Alifanov's iterative regularization technique. [105] In this method, the number of iterations plays the role of regularization and a termination criterion is chosen such that a stable solution is obtained. [122]

Unlike whole-time domain methods, sequential methods estimate a given parameter using only a limited range of measurements and continue sequentially in time. One of the leading methods is the function specification method with future time algorithm developed by James Beck. [104] It is designed such that the estimation algorithm efficiently takes advantage of the fact that the subsurface temperature is lagged compared to the surface heating. [123] In this method, the boundary condition at a given time is estimated using thermocouple measurements for a limited future time window. The number of future time steps used in the estimation has the same effect as the regularization approach for whole-time domain methods. Tikhonov regularization can also be implemented in this formulation in addition to the future time approach. This method has the advantage of being more computationally efficient than whole-time domain methods, but less stable for small time steps. To benefit from this efficiency, the code used to solve the direct problem must be able to save and restart the solution in time. Without such option, the entire solution has to be calculated at every time step.

In addition to the deterministic regularization methods, statistical techniques within the Bayesian framework are another way to solve sequential inverse problems. These methods belong to the class of state estimation problems and are based on sequential estimation of a set of dynamic variables (state). In this case, dynamic equations are developed to propagate the state and its uncertainty in time. Then, a statistical filter is used to estimate the state variables at a given time from the dynamic equation predictions, the measurements and their uncertainties. Kalman Filter (KF) and other variations such as Extended Kalman Filter (EKF) or Unscented Kalman Filter (UKF) are the most popular Bayesian filters. [124, 125, 126]

While some variations such as EKF address nonlinear problems, the Kalman filter is mathematically limited to linear problems with additive Gaussian noises. Within the EDL field, these methods are widely used for atmospheric and trajectory reconstruction. [111, 112, 113, 114, 115]

Monte Carlo methods use random samples and are not as restrictive as the Kalman filter. These methods are also known as particle filters and can be applied to nonlinear models with non-Gaussian errors at the expense of higher computational cost. Researchers have recently started using Bayesian methods for the solution of IHTPs. Kaipio et al. [127] provides an excellent review of the application of these methods to heat transfer problems; however, the use of statistical methods for this investigation requires significant reformulation of the governing equations in the form of dynamic equations. Furthermore, good knowledge of measurement uncertainties and covariances are required, but are not readily available for thermocouple measurements. Research in the IHTP field has suggested that regularization techniques provide sufficient and accurate results. For these reasons, statistical methods are not pursued in this work.

Inverse methods, specifically regularized whole-time domain and statistical Monte Carlo methods, require solution of the direct problem many times as they iterate to find the solution to the inverse problem. Also, at each iteration many direct runs are required to numerically calculate the Jacobian matrix used in estimation algorithms. Therefore, the solution of inverse problems can be time-consuming if the solution to the direct problem is computationally expensive. Inverse analyses can only be as accurate as the direct model used to describe the physical problem. Any structural uncertainty or deficiencies in the model can not be removed through a simple inverse estimation.

2.4 Multi-parameter Estimation Framework

In a complex ablation and conduction problem with pyrolysis, many parameters can contribute to the overall uncertainty. The goal of this section is to develop a multi-parameter estimation framework which would address the challenges in accurate estimation of multiple constant parameters from in-depth temperature data. This framework can have application to material property estimation from flight temperature data or both material property and surface heating estimation from arc jet data where surface heating is constant in time. The motivation for developing this framework is explained here and the different steps are briefly explained. Chapter 3 will provide a more detailed explanation of the steps while applying them to the estimation of material properties and aerothermal properties from an arc jet dataset.

In order to discuss some of the challenges involved in multi-parameter estimation problems, consider Eq. (13) as a simple representation of the data analysis problem. The vector $\mathbf{Y}$ is the measurement of the system response (thermocouple measurements), vector $\boldsymbol{\eta}$ is the true material thermal response, $\mathbf{P}$ is a vector of constant material and/or aerothermal parameters, and G is the physical model (FIAT). It is assumed that the problem is formulated such that these parameters are constants and not functions of time. In an inverse data analysis problem, the objective is to estimate the true input parameters $\mathbf{P_{true}}$ from the thermocouple measurements $\mathbf{Y}$.

$$\mathbf{Y} = \boldsymbol{\eta} + (\epsilon_{random} + \epsilon_{bias}) = G\left[\mathbf{P_{true}}\right] + \epsilon_{model} \tag{13}$$

This equation shows that the measurements are not exactly the same as the true response due to measurement errors. An example of bias error is thermal lag wherein there is a lag between the temperature reading of the thermocouple and the actual temperature of the material. Additionally, measurement errors due to instrument malfunctions or random noise are possible. The right hand side of the equation shows that the physical model is not always perfect. Theoretical models provide our best

understanding of a physical phenomenon, but do not represent the physics exactly. This difference is called model or structural error. These errors can make inverse estimation unstable. Additionally, different combinations of input parameters can result in similar material response if these parameters are linearly dependent. Such parameters will not be simultaneously observable from the data, making the solution of the inverse problem non-unique.

For complex problems where different parameters contribute to the uncertainty, a comprehensive framework is required to yield an accurate multi-parameter estimation. The results of inverse estimation depend strongly on the range of measurements used in the analysis and input parameters being estimated. It is crucial that the measurement and parameter selections are performed intelligently prior to the inverse estimation. The framework developed here proposes guidelines on how to conduct the parameter estimation via four steps: Nominal Analysis, Uncertainty Analysis, Sensitivity Analysis, and Inverse Analysis.

The first three steps provide the prerequisite information to set up a successful inverse estimation. Nominal Analysis examines the quality of the data and provides a direct comparison between the data and the model predictions. This is analogous to the direct approaches used historically by the TPS community. The range of measurements that are reliable for inverse analysis is identified. Uncertainty analysis narrows down the list of material and aerothermal parameters to an appropriate subset representing the top contributors to the overall uncertainty. Sensitivity Analysis investigates potential dependencies between the parameters which may lead to observability challenges. These steps provide a list of parameters to be estimated and the range of data that must be used in the estimation process. In the last step, inverse methods are used to estimate the selected parameters from the data.

2.4.1 Nominal Analysis

Nominal analysis can be thought of as a direct analysis. The goal is to examine the quality of the data and perform a direct comparison between the data and nominal model predictions before proceeding with inverse analysis. Model and measurement errors can lead to inaccurate solution of the inverse problem and introduction of bias errors in the estimated parameters. Nominal analysis is performed to identify such errors and determine the range of measurements that are reliable for inverse analysis by examining the flight data and performing a direct comparison of predictions to flight data. The objectives and steps of the nominal analysis are as follows:

- Examine the data quality to identity measurement errors, anomalies or sensor malfunctions.
- Correct for measurement errors, if possible. If not, determine what range of the data is reliable for inverse analysis.
- Compare the data to the predictions from the physical model based on nominal parameters.
- Examine the model fidelity by identifying where the data trends are fundamentally different from model predictions.
- Select the measurement range that will be used in the inverse analysis.

2.4.2 Uncertainty Analysis

Uncertainty analysis is performed to identify what parameters need to be estimated by the inverse method and what range of measurements are most sensitive to these parameters. This process defines a hierarchy of the aerothermal and material property parameters based on the largest uncertainty contribution to the in-depth temperature predictions. This step also provides insight into the direct problem and expected qualitative trends. The approach employed to accomplish these goals is probabilistic, and is accomplished with Monte Carlo (MC) simulations. The objective is to start

with a complete list of material and aerothermal parameters and down select to a smaller subset containing parameters of most importance.

Historically, aerothermal and TPS design and analysis has been conducted in a deterministic fashion. One of the first examples of probabilistic TPS design was the use of MC techniques in determining TPS margins by Dec and Mitcheltree [128] for the proposed Mars Sample Return Earth Entry Vehicle. However, only a small number of input parameters were studied. Studies performed by Bose et al. [129] and Wright et al. [130] also showed the potential of MC simulation as a technique to predict the uncertainties in aerothermal environments. Chen et al. [131] demonstrated a general MC technique for establishing appropriate TPS thickness margins and for performing sensitivity studies, applying this technique to the TPS design for several space entry vehicles. Building on this work, Sepka and Wright [132] developed a MC analysis software tool and applied it to the MSL aeroshell TPS design. This tool was used to determine the parameters that have the greatest influence on the MSL bondline temperature. Copeland et al. [133] used experimental data for PICA to generate Probability Distribution Functions (PDF) for its material properties and performed MC and sensitivity analyses for MSL relevant conditions. Most of the past work was focused on the use of MC techniques for design margin quantification. In this work, Monte Carlo techniques are used to identify the most influential parameters in thermal response modeling, for subsequent use in inverse analysis.

Gaussian distributions are defined for many aerothermal and TPS modeling parameters. The standard deviations used for these input parameters are generally derived from material property testing, aerothermal tool uncertainty studies or engineering judgment. The MC simulation involves 10,000 direct FIAT runs with dispersed input parameters to ensure statistical accuracy. The temperature response calculated by FIAT is saved for each MC run.

Post-processing is traditionally done using linear regression analysis by calculating the relative contribution of each input's variability to the overall output variability. [132] This is done by calculating the correlation coefficient between the vector containing all instances of an input parameter and the vector containing the corresponding instances of any output (e.g., predicted thermocouple temperature). The square of the correlation coefficient is the fractional contribution to the uncertainty in the output due to the uncertainty in the input parameter. The fractional contribution can be plotted as a function of time for the input parameters at different thermocouple locations. Examination of these plots lead to the identification of a smaller subset of parameters which contribute the most to temperature uncertainty, or in other words, the parameters that are most important to estimate.

2.4.3 Sensitivity Analysis

Sensitivity analysis is used to determine which parameters can be independently estimated. Knowledge of the correlation between the input parameters is crucial for inverse analysis because most inverse algorithms are gradient-based and use sensitivity coefficients in order to update the parameters. If the magnitudes of these sensitivity coefficients are small or if they are correlated with each other, it may cause numerical problems with solution stability and uniqueness of the inverse method. Parameters that are strongly correlated are not independently observable from the data.

Sensitivity analysis is performed by examining the change in the outputs (temperature predictions at thermocouple locations) due to a small one-by-one change in each input parameter. The smaller subset of variables identified by the Monte Carlo analysis is used here. The sensitivity is calculated numerically using central differencing. These values can be then plotted as a function of time for all parameters and one can examine the level of linear dependency between these traces. In addition to the graphical method, correlation coefficients between sensitivity coefficient can be

calculated. A high correlation coefficient (a value close to 1) indicate high linear dependency between the two parameters, meaning that they can not be independently estimated from data.

2.4.4 Inverse Analysis

The objective of inverse analysis is to provide a better match between the data and FIAT predictions through the estimation of the identified input parameters using inverse methods.

This goal is accomplished by minimizing an objective function containing both the measured and predicted thermocouple temperatures. The objective function usually used in parameter estimation problems is the ordinary sum of square of errors which was shown earlier in Eq. (12). Other variations such as weighted least-squares, maximum likelihood, and maximum a posteriori are also possible, but not pursued in this work. Inverse methods iteratively minimize this objective function by adjusting the input parameters (material or aerothermal parameters). This is also called a nonlinear least-squares problem because the model is nonlinear in terms of the inputs.

Minimization of nonlinear least-squares problems has been conducted with many methods. Some of the gradient methods used for this minimization are: steepest descent, conjugate gradient and Gauss-Newton. Levenberg-Marquardt and Box-Kanemasu methods are variations of the Gauss-Newton method. Second-order methods such as Newton's minimization can also be used; however, calculation of second derivatives can be challenging and time consuming for most problems. In addition to gradient methods, stochastic methods such as a genetic algorithm or random walk have been also used for these problems. In this work, three methods are considered: Levenberg-Marquardt, Box-Kanemasu and conjugate gradient. The Levenberg-Marquardt method has been successfully used for many parameter estimation problems in the heat transfer field. It is selected here as the initial reference method.

Levenberg-Marquardt method was originally derived by Levenberg [134] and later modified by Marquardt. [135] It was devised for application to nonlinear parameter estimation problems but has since been successfully applied to a wide range of linear and nonlinear problems. This iterative technique tends to the Gauss-Newton method in the neighborhood of the minimum and to the steepest descent method in the neighborhood of the initial guess. This is done using a damping parameter which reduces oscillations and instabilities due to ill-conditioning. References [103, 106] explain in detail the derivation of the Gauss-Newton method and the Levenberg-Marquardt modification. In summary, the method is derived by calculating the gradient of the objective function S given in Eq. (12), linearizing the vector of predicted temperatures $\mathbf{T}(\mathbf{P})$ with a Taylor series expansion around the current solution $\mathbf{P}$ and setting the gradient of S to zero. The iterative algorithm for the estimation of parameters using this method is given below.

1. Solve the direct problem with the current estimate of parameters $\mathbf{P}^k$ to obtain the predicted temperatures $\mathbf{T}\left(\mathbf{P}^k\right)$.
2. Compute the sum of square of errors using Eq. (12).
3. Compute the sensitivity matrix $\mathbf{J}$ using the following equation. The sensitivity coefficients are calculated using central difference approximations.

$$\mathbf{J} = \begin{bmatrix} \frac{\partial T_1}{\partial P_1} & \cdots & \frac{\partial T_1}{\partial P_N} \\ \vdots & \ddots & \vdots \\ \frac{\partial T_M}{\partial P_1} & \cdots & \frac{\partial T_M}{\partial P_N} \end{bmatrix} \tag{14}$$

4. Solve the following linear system of equations to find the change in parameters $\Delta\mathbf{P}^k$, where μ^k is the Levenberg-Marquardt damping parameter.

$$\left[\mathbf{J}^{k^T}\mathbf{J}^k + \mu^k\mathbf{I}\right]\Delta\mathbf{P}^k = \mathbf{J}^{k^T}\left[\mathbf{Y} - \mathbf{T}\left(\mathbf{P}^k\right)\right] \tag{15}$$

5. Compute the new estimate $\mathbf{P}^{k+1}$.

$$\mathbf{P}^{k+1} = \mathbf{P}^k + \Delta\mathbf{P}^k \tag{16}$$

6. Solve the direct problem with the new estimate of parameters $\mathbf{P}^{k+1}$ to obtain the predicted temperatures $\mathbf{T}\left(\mathbf{P}^{k+1}\right)$. Compute the new sum of squares of the errors $S\left(\mathbf{P}^{k+1}\right)$.
7. If $S\left(\mathbf{P}^{k+1}\right) \geq S\left(\mathbf{P}^{k}\right)$, replace μ^k by $10\mu^k$ and return to step 4.
8. If $S\left(\mathbf{P}^{k+1}\right) < S\left(\mathbf{P}^{k}\right)$, accept the new estimate $\mathbf{P}^{k+1}$ and replace μ^k by $0.1\mu^k$.
9. Check the stopping criteria. If the stopping criterion is satisfied, stop the iterative procedure; otherwise replace k by $k+1$ and return to step 3.

The iterative procedure is stopped once the change in parameters has stabilized to a small value. A possible stopping criterion is shown in the equation below.

$$\left\|\mathbf{P}^{k+1} - \mathbf{P}^{k}\right\| < 10^{-4} \tag{17}$$

It should be noted that numerical calculation of the sensitivity matrix $\mathbf{J}$ could be time consuming because it requires multiple solutions of the direct problem. The $\mu^k\mathbf{I}$ term in Eq. (15) is the Levenberg-Marquardt modification term. If this term is removed, the algorithm transforms into the Gauss-Newton method. One problem with the Gauss-Newton method is that the matrix $\mathbf{J}^T\mathbf{J}$ has to be non-singular to obtain a solution. Problems where the determinant of this matrix is close to zero are ill-conditioned. Inverse heat transfer problems are generally ill-conditioned near the initial guess and the application of Gauss-Newton method alone can cause instabilities and oscillations. The Levenberg-Marquardt modification alleviates such difficulties by adding the extra term. In practice, this modification has a similar effect as the Tikhonov regularization technique. First, a small damping parameter is chosen. If the objective function is not reduced, the damping parameter is increased which makes the method tend toward the steepest descent method and away from Gauss-Newton.

Another modification of Gauss-Newton is the Box-Kanemasu method. Gauss-Newton uses a linear approximation and could be ill-conditioned in the region around initial guess. In the case of a strongly nonlinear problem, the linear assumption is

valid only for a small region. Therefore, a large step in the minimum direction could lead to an unwanted increase in the objective function. The Box-Kanemasu method alleviates this problem by selecting a step size that ensures a reduction in the objective function. The derivation and algorithm for this method are provided in Ref. [103]. The algorithm is similar to the Levenberg-Marquardt method (without the damping term) while Eq. (16) is modified to include a step size restriction in addition to the direction $\Delta \mathbf{P}^k$. Interpolation methods using polynomial approximations are employed to find a step size that guarantees the minimization of the objective function.

The conjugate gradient method is another powerful iterative technique used for the solution of nonlinear inverse problems. In this method, a suitable step size is taken along a direction of descent in order to minimize the objective function. The direction of descent is a linear combination of the negative gradient direction at the current iteration and the direction of descent of the previous iteration. This linear combination is such that the angle between the direction of descent and the negative gradient direction is less than 90 degrees so that minimization is assured. This linear combination is calculated using a variable called the conjugate coefficient. There are many different formulations in literature for the calculation of this direction of descent such as Fletcher-Reeves, Polak-Ribiere or Powell-Beale. [136]

All these methods are valid for the multi-parameter estimation framework. In Chapter 3, these three methods will be compared when the multi-parameter estimation framework is applied to an arc jet dataset.

2.5 Surface Heating Function Estimation Framework

In the case of flight applications, the vehicle descends through the atmosphere on a trajectory where freestream conditions such as density, velocity and angle of attack change in time. This causes the resulting aerothermal environment to be a time-dependent function. In this case, estimation of surface heating from subsurface

thermocouple data is no longer a straightforward parameter estimation problem. Instead, a time-dependent profile for the surface heating needs to be estimated. This is a function estimation problem.

The inverse methods used to solve parameter estimation and function estimation problems are similar; however, function estimation problems have their own unique challenges. Sometimes, they can be simplified by making certain assumptions about the functional form of the heating profile and using *a priori* information in the estimation process. However, such information is often not available and could limit the accuracy with which the surface heating is estimated. In the case where no *a priori* information is available, the entire profile needs to be determined.

Typically, function estimation problems can be solved by decomposing the time-dependent variable into multiple discrete points in time and treating each point as a separate parameter. In this approach, since the parameters are only related in time and are not correlated with each other, the non-uniqueness problem, which is common for parameter estimation problems and was discussed in the previous section, does not exits. However, since many points have to be estimated to recover the time-dependent function at a reasonable resolution, some unique challenges arise. For example, if one needs to estimate surface heating for a 150-second trajectory at 1-Hz resolution, the problem involves the estimation of 151 parameters. Problems that require the estimation of many parameters are sensitive to measurement and model errors and can become unstable. Often, this results in large oscillations in the estimated heat rate profile. As mentioned before, regularization techniques are typically used to make these problems better posed.

In the following subsections, the components of the time-dependent surface heating estimation framework are discussed with specific application to subsurface temperature data collected from the ablative heatshield of a planetary entry vehicle. Chapter 4 will discuss the application of this framework to MSL simulated heatshield

data and Mars Pathfinder heatshield flight data.

2.5.1 Temperature Data

In most experimental settings, whether it is an arc jet test or a flight experiment, thermocouples are used to record the subsurface temperature of the TPS material at different locations on the heatshield. A surface thermocouple is not generally used for ablative materials because the surface recedes and its temperature rises above the operating range of most available thermocouples. In some experiments, only one subsurface thermocouple is used at a given location while in other experiments multiple thermocouples are inserted at varying depths to record the material response throughout the TPS thickness. For the purpose of surface heating estimation, the data from the shallowest thermocouple should be used due to the delayed and damped nature of heat transfer. As was shown in Figure 18, the deeper the thermocouple the less sensitive the material temperature response is to a change in surface heating. Additionally, the shallowest thermocouple is the least affected by uncertainties in material model.

The only exception to this rule is when the data from the shallowest thermocouple is not reliable or not available for the entire estimation period. For example, if the surface recedes past the shallowest thermocouple in the middle of the trajectory and it ceases to provide data, then data from the second shallowest thermocouple should be used. However, the deeper the thermocouple, the more lagged and damped the temperature response is compared to any change in surface heating, which reduces the accuracy of surface heating estimation and the stability of inverse methods. This is discussed in more detail in Chapter 4 for the simulated MSL data test problem.

Often, there is uncertainty in measured temperature data which should be taken into consideration in surface heating estimation. To mitigate this situation, the major sources of uncertainty are identified and their effects on the heating estimation

results are quantified. One example is the thermocouple location uncertainty. Once thermocouples are inserted into the material, their accurate depths are measured using an X-ray technique. While this method is accurate, there is a small level of uncertainty associated with it which could be significant due to high temperature gradients close to surface. Another source of error is random noise. Sometimes thermocouple measurements have some inherent noise which could affect the estimation results and stability. Thermal lag is another source of uncertainty which is defined as the difference between thermocouple reading and actual TPS material temperature. Thermocouple temperature often lags the actual TPS temperature due to its thermal mass. The effect of these uncertainties on the estimated surface heating have to be quantified.

In this work, the NASA code FIAT will be used to simulate the in-depth TPS temperature and material response. There is always some level of uncertainty in the computational code and the material model. The effect of these uncertainties on the heating estimation results must also be quantified in a surface heating estimation problem.

2.5.2 Estimation Parameters

For an ablative material, surface heat rate is not a direct input to FIAT. As shown earlier, surface heating is modeled with a surface energy balance equation which represents many physical phenomena that occur at the surface of an ablative material. This equation (called "option 1" in FIAT) is:

$$\begin{aligned} C_H(H_r - h_w) + \dot{m}_g h_g + \dot{m}_c h_c - (\dot{m}_c + \dot{m}_g)\, h_w \\ +\alpha_w q_{rad} - \sigma \epsilon_w (T_w^4 - T_\infty^4) - q_{cond} = 0 \end{aligned} \tag{18}$$

The first term represents the sensible convective heat rate. The sum of the second, third and fourth terms defines the total chemical energy at the surface due to the ablation products and pyrolysis gas. The fifth and sixth terms are the incoming radiative

heat rate absorbed by the material and the reradiation to the environment. The last term in Eq. (18) represents the rate of heat conduction into the TPS material. The nominal surface heating is calculated by CFD tools assuming radiative equilibrium wall and certain catalytic and turbulence models. Based on CFD solutions, the total recovery enthalpy, H_r, and wall enthalpy, h_w, can be determined. Knowing these values and the CFD-predicted convective heat flux, the surface heat transfer coefficient, C_H, is calculated. C_H, H_r, surface pressure, and the blowing reduction parameter are input to FIAT as functions of time. It should be noted that the CFD heat transfer coefficient values are unblown, and FIAT corrects the input C_H for heating reduction due to pyrolysis gas blowing. [47] Pre-calculated equilibrium wall chemistry solutions (B' tables) are input to FIAT for a given material and the surface energy balance is solved iteratively using the boundary condition inputs from CFD and the B' tables. In doing so, FIAT calculates its own wall enthalpy and temperature which are often not equal to the CFD-calculated values due to the usage of different surface energy balance approaches.

Many of the parameters in Eq. (18) can affect the subsurface thermocouple temperature and the surface heating estimate. Some of these parameters are inputs to FIAT while others are calculated internally by FIAT. While it is desirable to have accurate knowledge of all these terms, they are not all directly observable from flight data and any attempt to simultaneously estimate multiple parameters leads to non-unique solutions. In this work, the inverse problem is defined as the estimation of the time-dependent heat transfer coefficient profile, C_H. Inverse methods are used to estimate heat transfer coefficient as a function of time while keeping recovery enthalpy fixed to the CFD-calculated value and allowing FIAT to internally calculate surface ablation chemistry and material decomposition. Once the heat transfer coefficient is estimated, the resulting heat rate can be calculated using the other parameters. The net surface heat rate is the sum of the first four terms in Eq. (18) which includes the

convective and chemical heating contributions.

Since heat transfer coefficient is time-dependent, it is estimated by discretization in time. The estimation frequency is a balance between the desired resolution and computational resources. Higher estimation frequency results in the reconstruction of surface heating at a higher time resolution; however, it requires more computational resources. Surface heating is usually estimated at a frequency of 0.2-1 Hz depending on the desired resolution for a given problem and available computational resources. It should also be noted that the estimation problem must be over-determined meaning that there must be always more data points available than estimation parameters. For example, if the temperature measurements are available at only 1 Hz, the surface heating has to be estimated at a frequency lower than 1 Hz.

However, in some applications, there are certain limitations with the surface heat transfer coefficient estimation approach. This approach relies on FIAT equilibrium models for the calculation of surface chemistry terms. As long as the material ablation model is accurate, the heat transfer coefficient estimation is reliable. However, the equilibrium chemistry model is not accurate for some materials at certain heating conditions and results in inexact calculation of wall enthalpy. In the absence of validated finite-rate chemistry models, an alternative surface energy balance option, implemented in FIAT (called "option 3"), is used which can be reformulated into the following equation:

$$q_s + \alpha_w q_{rad} - \sigma \epsilon_w (T_w^4 - T_\infty^4) - q_{cond} = 0 \tag{19}$$

The first term in this equation represents heating at surface and is analogous to the sum of the first four terms in Eq. (18) which includes the convective heat flux and chemical heating contributions. The surface heating can be directly estimated using this equation. This approach does not require the calculation of surface chemistry terms, therefore, it does not have the limitation of heat transfer coefficient estimation approach. However, use of this equation implies that surface recession can not be

calculated and must be assumed zero. Chapter 5 discusses the application of this approach to MSL flight data.

2.5.3 Inverse Methods

The inverse methods used for surface heating estimation are similar to the methods used for parameter estimation. In this work, the Gauss-Newton method is used in conjunction with Tikhonov regularization to estimate surface heating.

The Gauss-Newton algorithm is widely used to solve nonlinear least squares problems. It is a modification of Newton's method which does not require the knowledge of second derivatives. The algorithm for this method is very similar to the Levenberg-Marquardt method described earlier. Gauss-Newton iteratively minimizes the ordinary least square objective function, S, shown in Eq. (12). The algorithm is developed by deriving the gradient of the objective function, linearizing the vector of predicted temperatures with a Taylor series expansion around the current solution and setting the gradient of S to zero. The expression can be rewritten to derive the change in parameters, $\Delta\mathbf{P}$, required to minimize S:

$$\mathbf{J^{k^T}J^k\Delta P^k} = \mathbf{J^{k^T}}\left[\mathbf{Y} - \mathbf{T}\left(\mathbf{P^k}\right)\right] \tag{20}$$

This equation is similar to Eq. (15) shown earlier for the Levenberg-Marquardt method. $\mathbf{J}$ is the Jacobian matrix which is equal to the derivative of the predicted TC temperatures to estimation parameters (discretized points along the C_H profile) shown earlier in Eq. (14). The calculation of this Jacobian matrix is computationally expensive because its numerical approximation requires many solutions of the direct problem.

2.5.3.1 Tikhonov Regularization

Surface heating estimation problems require identification of many parameters in time which cause instabilities in the estimation process and large oscillation in surface

heating estimates. The Tikhonov technique is used to regularize the ill-posed inverse problem and alleviate non-physical oscillations that occur in the boundary condition estimates. [104, 120] This technique involves addition of a penalty function to the ordinary least-squares objective function to alleviate oscillations in the solution. This penalty term is composed of a squared difference function of the surface heating profile estimation points and can take various forms (0^{th},1^{st} and 2^{nd} order), shown in the generalized form in Eq. (21). For example, the zero-order function is equal to the sum of squares of estimation points while the first-order function is equal to the sum of squared differences of consecutive estimation points. By assigning appropriate values to the weighting parameters (W_0, W_1 and W_2), the order of regularization can be controlled. First-order Tikhonov regularization ($W_0 = W_2 = 0, W_1 = 1$) has proved to be the most effective for the surface heating estimation problems and is therefore used as the baseline method in this work. Equations (12) and (20) need to be modified accordingly:

$$\begin{aligned} S = [\mathbf{Y} - \mathbf{T}]^T [\mathbf{Y} - \mathbf{T}] + \mu \left[W_0 (\mathbf{IP})^{\mathbf{T}} \mathbf{IP} \; + \right. \\ \left. W_1 (\mathbf{H_1 P})^{\mathbf{T}} \mathbf{H_1 P} + W_2 (\mathbf{H_2 P})^{\mathbf{T}} \mathbf{H_2 P} \right] \end{aligned} \tag{21}$$

$$\left[\mathbf{J}^{\mathbf{T}} \mathbf{J} + \mu (W_0 \mathbf{I} + W_1 \mathbf{H_1}^{\mathbf{T}} \mathbf{H_1} + W_2 \mathbf{H_2}^{\mathbf{T}} \mathbf{H_2}) \right] \Delta \mathbf{P} = \mathbf{J}^{\mathbf{T}} [\mathbf{Y} - \mathbf{T}] \tag{22}$$

$$\mathbf{H_1} = \begin{bmatrix} -1 & 1 & 0 & 0 & \cdots & 0 \\ 0 & -1 & 1 & 0 & \cdots & 0 \\ \vdots & \ddots & \ddots & \ddots & \ddots & \vdots \\ 0 & \cdots & 0 & -1 & 1 & 0 \\ 0 & \cdots & 0 & 0 & -1 & 1 \\ 0 & 0 & \cdots & 0 & 0 & 0 \end{bmatrix} \quad \mathbf{H_2} = \begin{bmatrix} 1 & -2 & 1 & 0 & \cdots & 0 \\ 0 & 1 & -2 & 1 & \cdots & 0 \\ \vdots & \ddots & \ddots & \ddots & \ddots & \vdots \\ 0 & \cdots & 0 & 1 & -2 & 1 \\ 0 & 0 & \cdots & 0 & 0 & 0 \\ 0 & 0 & \cdots & 0 & 0 & 0 \end{bmatrix} \tag{23}$$

The level of regularization can also be adjusted using the regularization parameter, μ. Small values of μ ensure rapid minimization of the ordinary least squares function, but result in large oscillations in the C_H profile. Larger values of μ reduce oscillations, but slow down the minimization of the objective function. In this work, a small value of μ is used initially and increased until the obtained estimate is satisfactory and the degree of oscillation is reduced sufficiently. Qualitatively, a good solution is a solution that traces through the unregularized oscillatory solution. Both regularized and unregularized surface heating estimation results will be shown and compared for the problems described in Chapters 4 and 5.

2.6 Thermocouple Driver Approach

The multi-parameter estimation framework is applied to an arc jet dataset to estimate constant material and aerothermal parameters in Chapter 3. In Chapter 4, the surface heating estimation framework is applied to simulated MSL data. Mars Pathfinder surface heating will also be reconstructed using the same framework.

The MSL entry vehicle was well instrumented, providing subsurface temperature data at different depths. This will enable estimation of both material properties and surface heating in a decoupled fashion. First, the surface heating estimation framework is applied to reconstruct the MSL time-dependent surface heating from the shallowest thermocouple data (TC1). A technique called the thermocouple driver (TC driver) approach is then applied to decouple the surface heating and material property estimation problems. This technique enables the estimation of material properties from the deeper thermocouple data (TC2-4) without the knowledge of surface heating. The analysis of MSL flight data through this approach is discussed in more detail in Chapter 5.

In the past, a TC driver approach has been used with arc jet data in cases where the surface boundary conditions were not well characterized. In this approach, the

data from the thermocouple closest to the surface is used as the wall temperature boundary condition and the in-depth heat transfer and pyrolysis problem is solved for the material stack beneath that thermocouple. This technique removes the effect of surface heating on the subsurface thermal response.

The diagram in Figure 19 shows the TC driver approach that will be used to estimate PICA thermal response and MSL surface heating from flight data. The top box in Figure 19, denoted as the "Surface Heating Problem", represents the application of the time-dependent surface heating estimation framework. The MSL time-dependent surface heating will be estimated from TC1 data using inverse methods and the nominal PICA material model. The effect of material model uncertainty on the surface heating estimation results is examined separately.

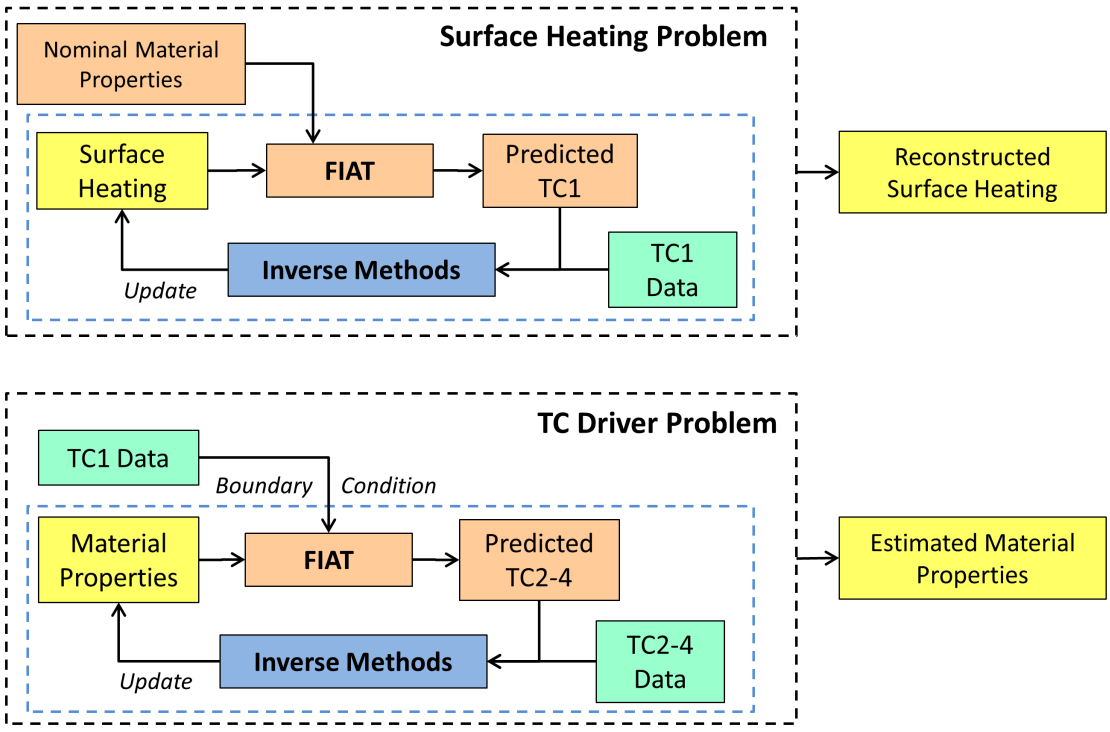

Figure 19: Flow diagram illustrating the TC driver approach that will be used for the reconstruction MSL surface heating and material response from MISP data.

The bottom box in Figure 19, denoted as the "TC Driver Problem", is where TC1 flight data is used as the true wall boundary condition and the material response

is calculated for the material stack below TC1 using FIAT. The multi-parameter estimation framework, described earlier in this chapter, can be used to identify what material response parameters should be estimated from the deeper thermocouple data (TC2-4).

2.7 Summary

The inverse estimation methodology and tools developed in this thesis for application to TPS material experimental data were described in this chapter. A discussion of direct vs. inverse analysis was presented illustrating the advantages of inverse data analysis. A background review of inverse heat transfer problems was also given. The inverse estimation methodology is comprised of two parts: the multi-parameter estimation framework and the surface heating function estimation framework. The multi-parameter estimation framework is developed for application to problems where multiple constant aerothermal and material properties have to be estimated from TPS temperature data. Within this framework, multiple supporting analyses are performed to identify what parameters should be estimated and what range of measurements should be used. This framework can be applied to heating parameters only when they are constant in time, as is usually the case in arc jet experiments.

In a flight mission, surface heating is time-dependent and its reconstruction becomes a function estimation problem. A surface heating function estimation framework is developed for application to such problems. This framework identifies the temperature data and the surface heating parameters that are appropriate for these estimation problems. Inverse methods and regularization techniques used in function estimation problems were also discussed. Finally, the TC driver approach which enables independent estimation of material properties and time-dependent surface heating for flight missions is discussed. The following chapters will present multiple studies where the feasibility and applicability of the developed inverse estimation

frameworks are tested for applications relevant to atmospheric entry ablative heat-shields. These frameworks will be used to estimate surface heating and material properties from measured or simulated subsurface temperature data.

CHAPTER III

APPLICATION OF THE MULTI-PARAMETER ESTIMATION FRAMEWORK TO ARC JET DATA

3.1 Introduction

The multi-parameter estimation framework, introduced in Chapter 2, will be applied to an arc jet dataset relevant to MSL design conditions. The objective is to estimate multiple constant material properties and aerothermal variables from subsurface temperature measurements of a PICA test coupon exposed to arc jet flow.

Traditionally, arc jet experiments have been used for material qualification or model validation where at most, one material parameter is manually adjusted to provide a qualitative match between model predictions and experimental data. However, in a complex ablation and pyrolysis problem, many parameters can contribute to the overall uncertainty, and a multi-parameter estimation capability is required to accurately estimate material properties. Furthermore, the surface heating conditions, despite being constant in time, are not always well-characterized and uncertainty can lead to incorrect estimation of material properties. One needs to also consider the simultaneous estimation of constant aeroheating parameters in order to ensure that the estimated material parameters are accurate.

The developed multi-parameter estimation framework is a four-step process which performs supporting analyses prior to inverse analysis in order to identify which parameters can be estimated from data and what range of measurements should be used in the estimation process. The nominal analysis examines the data quality and computational model fidelity by performing a direct comparison of the data and model predictions. This step will determine the range of measurements that is reliable for

inverse analysis. Uncertainty analysis identifies the parameters that contribute the most to temperature prediction uncertainty. These are the parameters that need to be estimated to reduce uncertainty. Sensitivity analysis examines the linear dependency between the parameters to determine which parameters are simultaneously observable and can be estimated independently. Finally, inverse methods will be used to estimate the selected constant material and aerothermal parameters.

For the current analysis, FIAT will be used to solve the ablation and thermal response problem. Refer to Chapter 1 for more information on the underlying equations in FIAT and its limitations. The aerothermal boundary conditions and material performance parameters are inputs to this program. The uncertainty and sensitivity analyses will be conducted using FIAT based on the nominal estimates for these parameters. In inverse analysis, a wrapper code will be used with FIAT to perform an estimation of the material and aerothermal parameters resulting in a better match between FIAT predictions and measured data.

3.2 Arc jet Test Case

Multiple tests were performed at the NASA Ames arc jet facilities in support of MSL heatshield development and qualification. Some of these tests were specific to qualification and characterization of the MISP instrument. The test selected for this investigation is from the IHF-205 MISP qualification arc jet test series conducted in October and November of 2008 at the NASA Ames Interaction Heating Facility (IHF). The specific test used here is run-4, identified by model number MQ08-2. The test model was a 6-inch flat face coupon with a PICA thickness of 1.25 inches. The use of a 6-inch coupon minimizes two-dimensional and lateral heat conduction effects, and thus makes a one-dimensional tool like FIAT appropriate for the analysis. A 0.8-inch MISP plug was inserted in the center of the PICA test model. The MISP plug was equipped with four subsurface thermocouples at X-ray measured depths of

0.1027, 0.1841, 0.4473 and 0.6959 inch. Figure 20 provides a diagram and a picture of the test model illustrating its key components.

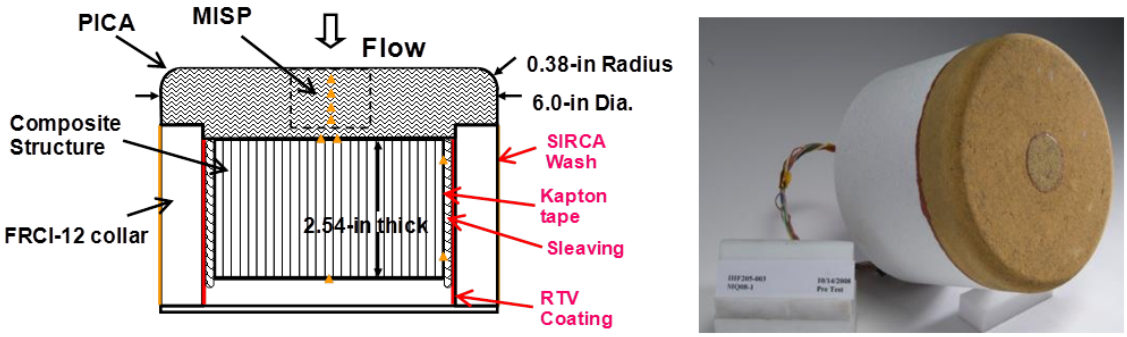

Figure 20: Diagram and picture showing key components of the arc jet test model.

The test was designed to experience a cold wall heat flux of 175 W/cm^2, a heat load of 4712 J/cm^2 and surface pressure of 0.28 atm for 31 seconds. However, there is significant uncertainty with arc jet aerothermal conditions, therefore this work will consider the estimation of some aerothermal parameters in addition to material properties. The MISP plug thermocouple temperature measurements will be used in this work to perform the estimation.

3.3 Nominal Analysis

As mentioned in Chapter 2, the nominal analysis can be thought of as a direct analysis. The quality of the data is examined by performing a direct comparison between the data and nominal model predictions before proceeding with inverse analysis. Model and measurement errors can lead to inaccurate solution of the inverse problem and introduction of bias errors in the estimated parameters. The nominal analysis can identify such errors and determine the range of measurements that are reliable for inverse analysis. The plot in Figure 21 shows the arc jet PICA coupon subsurface temperature measurements at the four thermocouple locations compared to the corresponding FIAT predictions using facility heating estimates and the nominal PICA material model.

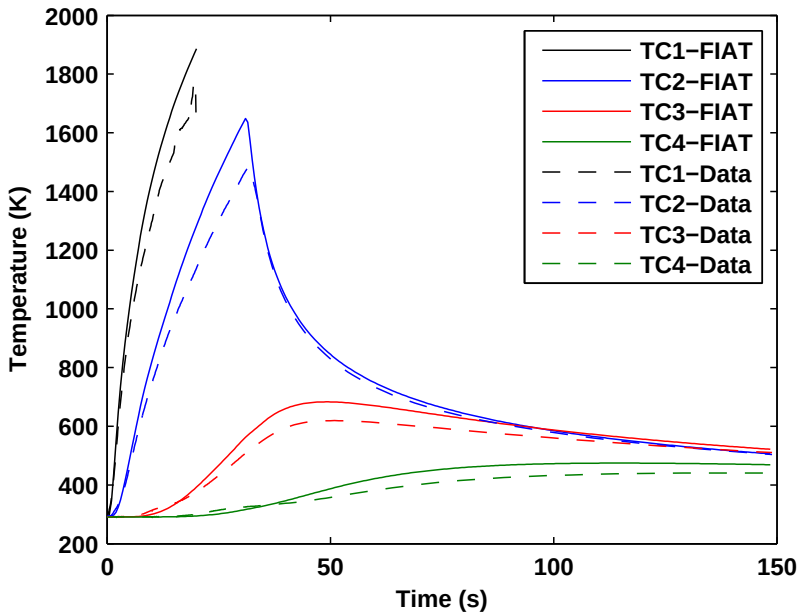

Figure 21: Arc jet temperature measurements at 4 TC locations compared to corresponding FIAT nominal predictions.

It can be seen that while the general trends match, there is significant difference between the data and FIAT predictions. Overall, FIAT calculations overpredict the arc jet data. In this step, the focus remains on data features and errors that can not be modeled with our theoretical model. Fortunately, the level of random noise in the data is very low; however, some data anomalies were observed for this arc jet test case which are highlighted in Figure 22. The data is down sampled to provide measurements at 0.5 second intervals. This provides some inherent smoothing; however, if significant random noise exists in the data, smoothing techniques such as a simple moving average method can be used to smooth the data before inverse analysis.

In Figure 22a, it can be seen that TC1 stops giving useful data around 20 s. This is due to the fact that the recession front has reached or is very close to TC1. Examining the slope changes, it can be seen that any temperature provided by TC1 after the time of 15 seconds is likely not reliable and should not be used for inverse analysis. Figure 22b shows the initial temperature for the TC and FIAT predictions. The TCs

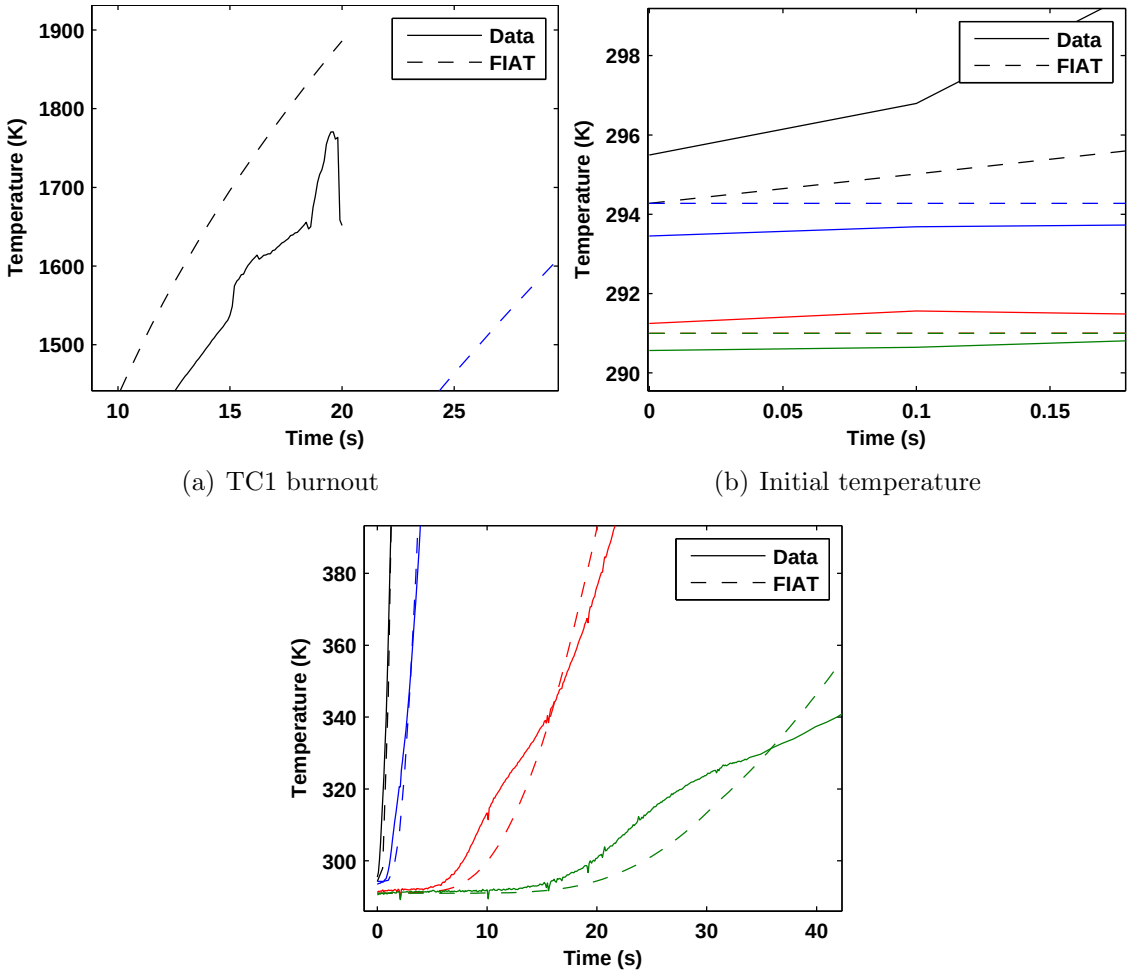

(a) TC1 burnout

(b) Initial temperature

(c) Deep TC preheating effect

Figure 22: Arc jet data and FIAT prediction comparison highlighting identified data anomalies (see the previous figure for TC labeling).

have different initial temperatures since they are located at different depths. It will be shown in the uncertainty analysis that the initial temperature has a significant effect on the temperature profile, especially for the deeper TCs. However, in FIAT different initial temperatures cannot be specified for different thermocouples. Initial temperature can only be specified for a block of material. Therefore, in order to have the best match with the data, the PICA coupon is divided into two separate blocks with different initial temperatures in FIAT. The first block, 0.3 inch in thickness, is set to the average of TC1 and TC2 initial temperatures while the second block, 0.5

inch in thickness, is set to the average of TC3 and TC4 initial temperatures. Another way to approach this problem would be to use a manual grid and provide an estimated initial temperature for each grid point.

Figure 22c shows an unexpected trend seen in TC3-4 data in the 290-360 K temperature range. The measured temperature abruptly rises, then changes slope and shows no resemblance to the predictions. This unusual TC pre-heating behavior has been seen in many arc jet tests, thermal flash tests and Pathfinder flight data. Modelers have not been able to fully understand this phenomenon, but it has been attributed to either the evaporation of absorbed moisture [137] or direct transmission of thermal radiation to the bondline. [5] For inverse analysis, our current model, FIAT, cannot recreate this behavior; therefore, including this range of data will only add bias error to the estimation process. For the purpose of this analysis, the data in this range will not be used. Furthermore, type-K TCs used in this test are calibrated only up to 1500 K. This is not a concern in this case because the TC1-2 data used for inverse analysis are below this limit.

Based on the nominal analysis performed here, the recommended data range that should be used for inverse analysis is given in Table 3. This data range is selected to minimize the effect of model and measurement errors on the accuracy of parameter estimation.

Table 3: The measurement range selected through nominal analysis.

	TC1	**TC2**	**TC3**	**TC4**
Start time (s)	2	4	20	50
End time (s)	15	150	150	150

3.4 Uncertainty Analysis

The nominal analysis provided the range of reliable data for inverse analysis. An uncertainty analysis is performed to identify what parameters need to be estimated

by the inverse method and what range of measurements are most sensitive to these parameters. The objective is to start with a complete list of material and aerothermal parameters and down select to a smaller subset containing parameters of most importance. As explained in Chapter 2, this is accomplished through Monte Carlo simulation and linear regression analysis of the simulation results. Monte Carlo analysis also provides insight into the direct problem and expected qualitative trends, which is a prerequisite for any inverse analysis.

In this investigation, the software tool used to perform Monte Carlo simulations is called McFIAT [132] which is a PERL-scripted code for use with FIAT. These simulations are performed for specified uncertainties in aerothermal variables and material properties. Gaussian distributions are used for the input parameters. Ten thousand runs are performed to ensure statistical accuracy. The nominal values used in this study for the input parameters are the current design values for PICA material properties and CFD predictions of the arc jet heating parameters. The material property uncertainties are primarily determined via expert judgment and results from past experiments. [138] The aerothermal uncertainties are based on previous work on the probabilistic analysis of the uncertainties in the CFD models. [130] Table 4 shows the 2σ uncertainty values normalized by the nominal value, (Δ), for both aerothermal and material input parameters varied in this Monte Carlo study. Uncertainty in virgin density is included to account for localized variability in material density. While the material bulk density can be measured prior to testing, the localized density can vary slightly due to non-uniform manufacturing of PICA.

One modification was made to McFIAT for this study. In McFIAT, the uncertainty values are independently defined and the code does not take into account correlations between the different parameters. Furthermore, the code has a built-in check to ensure that the random value generated for char density is always less than the value generated for virgin density. In doing so, the code creates artificial skewness in the

Table 4: Normalized 2σ uncertainties for the input parameters in the Monte Carlo analysis.

Material Parameter	Δ	**Aerothermal Parameter**	Δ
Virgin density, ρ_v	0.05	Surface pressure, P_w	0.15
Char density, ρ_c	correlated	Blowing reduction, λ	0.20
Virgin specific heat, Cp_v	0.05	Heat transfer coefficient, C_H	0.15
Char specific heat, Cp_c	0.10	Recovery enthalpy, H_r	0.20
Virgin conductivity, κ_v	0.15		
Char conductivity, κ_c	0.15		
Virgin emissivity, ϵ_v	0.03		
Char emissivity, ϵ_c	0.05		
Pyrolysis gas enthalpy, h_g	0.20		
Resin decomposition rate, A	0.20		
Char recession rate, B'_c	0.04		
Initial material temp., $T_{initial}$	0.05		

char density distribution. Figure 23a shows the virgin and char density scaling factors (with respect to the defined nominal values) as generated by a Monte Carlo run with the original McFIAT; this skewness can be clearly seen. A skewed distribution for an input parameter invalidates the normal distribution assumption used in the analysis of the results. Since these two material properties are not physically independent and are correlated, correlations were implemented in McFIAT for these parameters. Many tests have been conducted to measure virgin and char densities of PICA samples. The results from these tests were fit with a linear regression equation with added uncertainty bars. Using this information, random values of virgin density can be generated and the char density can be calculated from the derived equation with added random uncertainty. This capability was added to McFIAT. Figure 23b shows the virgin and char density scaling factors as generated by a Monte Carlo run with the modified version of McFIAT.

The Monte Carlo post-processing is traditionally done using linear regression analysis by calculating the relative contribution of each input's variability to the overall output variability. [132] This is done by calculating the correlation coefficient between

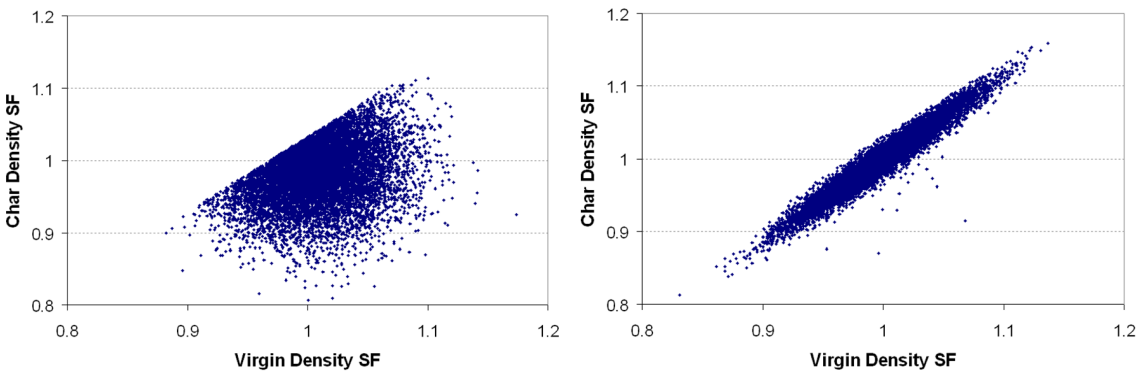

(a) Uncorrelated (b) Correlated

Figure 23: Addition of correlation to McFIAT removes the skewness problem.

the vector containing all instances of an input parameter (any of the parameters in Table 4) and the vector containing all corresponding instances of any output (e.g., predicted thermocouple temperature). The square of the correlation coefficient is the fractional contribution to the uncertainty in the output due to the uncertainty in the input parameter. Traditionally, a pie chart is used to illustrate the percent contribution of the input parameters for a certain output. This illustration is useful when the outputs are single-valued numbers such as final bondline temperature or final recession. This has been the case in the Monte Carlo work done in literature. However, a thermocouple measures the temperature as a function of time and it is important to show the time evolution of these uncertainty contributions. Therefore, in this work, for the first time, this regression analysis is done in a time-dependent manner. To illustrate time dependent results, area charts (sand charts) are used instead of pie charts. Each vertical slice of the area chart represents a pie chart. These charts help determine what parameters are the most important parameters and what time range is most sensitive to those parameters. The Monte Carlo results for the arc jet test problem are shown in Figure 24. The plot for TC1 does not cover the entire time range due to the fact that it burns out early.

When interpreting these plots, it is important to know the state of the material

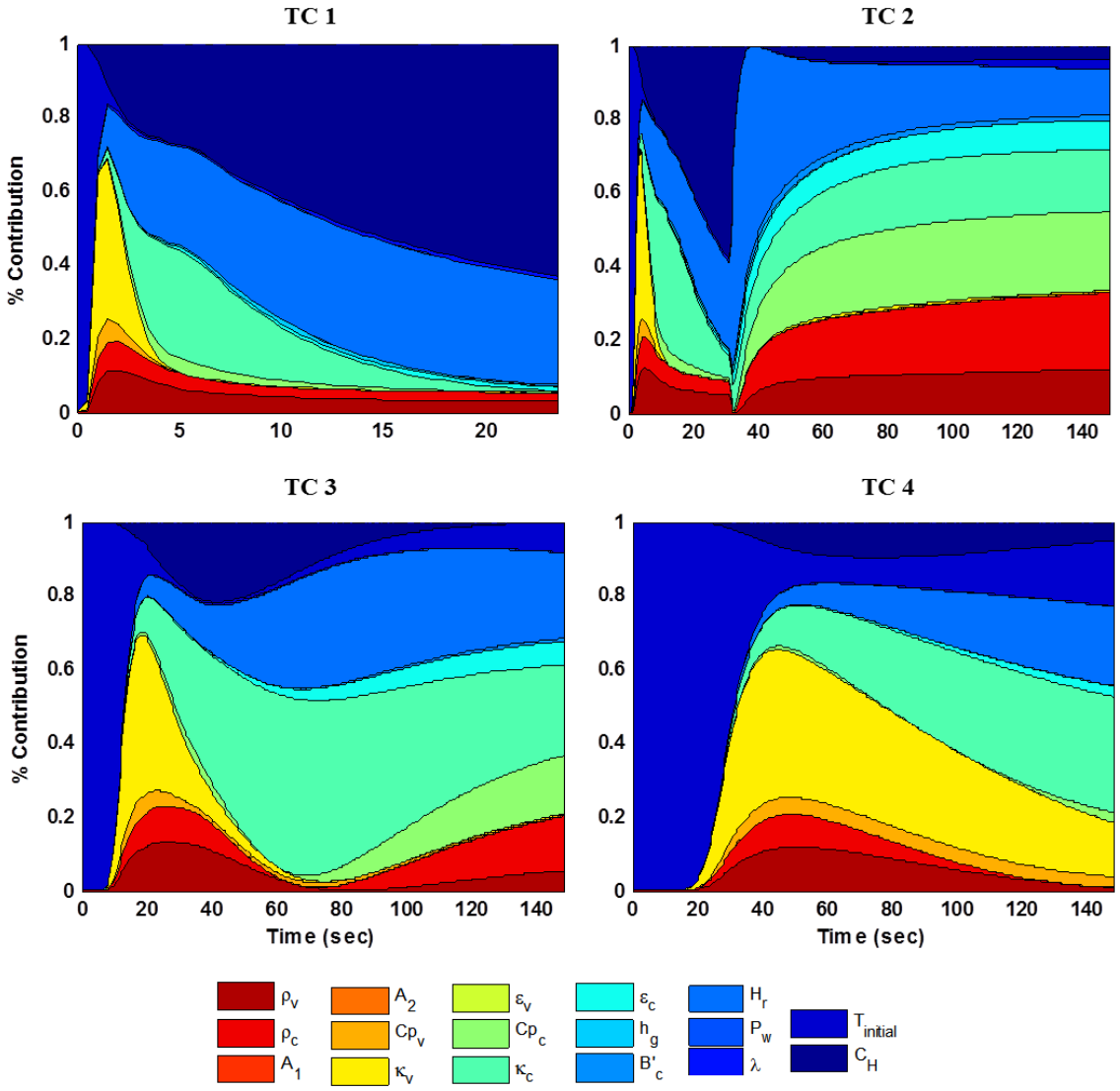

Figure 24: Uncertainty analysis results for the four subsurface thermocouples.

at each thermocouple as a function of time. Different input parameters become important whether the thermocouple is in the char zone, pyrolysis zone or virgin zone. Figure 25 shows the time-evolution of the recession, char and virgin fronts as predicted by FIAT for this arc jet case. Looking at this plot, the Monte Carlo results shown in Figure 24 can be put in the context of material state. Note that the same trend shifted in time is seen across all the thermocouples. This is indicative of the time that it takes for the heat to transfer in the material.

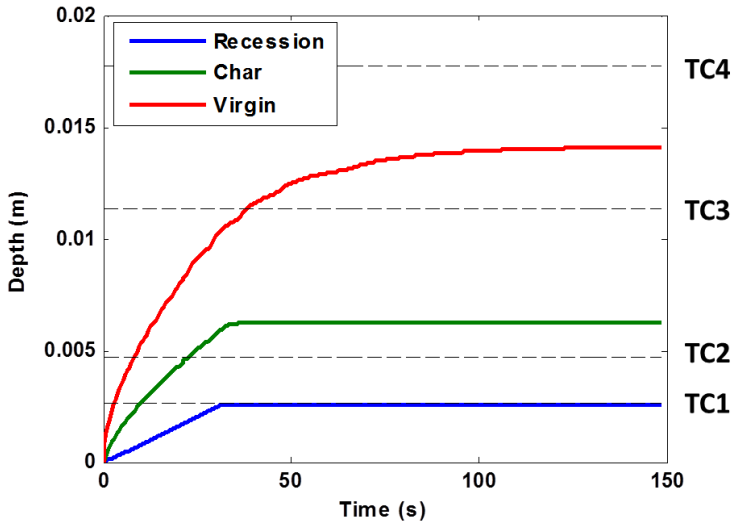

Figure 25: Time evolution of recession, char and virgin fronts as predicted by FIAT.

For each thermocouple in Figure 24, it can be seen that the initial material temperature is the top contributor in the beginning. This parameter is not important for inverse analysis, because it is known from the data and as it was shown in the nominal analysis it can be approximately set for the TPS block. As the time increases, the virgin properties become important. Initially, the material is mainly virgin and the heat transfer is therefore governed mainly by these parameters. In particular, the virgin conductivity and density are the top contributors (15-40s for TC3). These two parameters control the thermal diffusivity and the material's heat absorption.

As expected the heating-related parameters such as heat transfer coefficient, recovery enthalpy and char emissivity become more important, especially for the shallower thermocouples. In addition, the char properties, specifically char thermal conductivity and specific heat, are significant (40-100s for TC3). At this point, the material is charring from the top and pyrolyzing in the middle. This creates char and pyrolysis zones in the material in addition to the virgin zone. The pyrolysis zone material properties depend on both virgin and char properties which explain why the char

properties are more important. Figure 25 for TC3 demonstrates the connection between the material state and the Monte Carlo results clearly. TC3 enters the pyrolysis zone some time around 35 seconds. Now, if the area chart for TC3 is examined in Figure 24, it is evident that char thermal conductivity's contribution becomes significant around the same time. Additionally, it can be seen that in general the deeper thermocouples are more affected by material properties while the shallower ones depend more on heating parameters.

From the Monte Carlo results, 9 parameters are identified as the top contributors to output uncertainty: virgin density ρ_v, char density ρ_c, virgin specific heat Cp_v, char specific heat Cp_c, virgin thermal conductivity κ_v, char thermal conductivity κ_c, char emissivity ϵ_c, heat transfer coefficient C_H and recovery enthalpy H_r. While the percent contribution of these parameters is sensitive to the input uncertainties used in the Monte Carlo analysis, the list of parameters identified as top contributors does not change if these input uncertainties are slightly perturbed. For example, if the uncertainty for char conductivity is increased, its relative contribution will also increase. However, the top 9 parameters will not change.

The identified parameters are used in the sensitivity and inverse analyses. It should be noted that scaling factors of these parameters normalized by the nominal values are used in the following analyses. Additionally, virgin and char density are combined into one parameter for the inverse analysis so that virgin density always remains greater than char density. The use of one scaling factor for both density variables makes intuitive sense because a PICA block with lower virgin density is expected to have a similarly lower char density (also evidenced by the linear relation between the two parameters shown earlier from PICA sample measurements, Figure 23b).

3.5 Sensitivity Analysis

While Monte Carlo analysis helps determine what parameters need to be estimated, sensitivity analysis identifies what parameters can be independently estimated by examining the linear dependency between parameters. The parameters that are highly correlated are not simultaneously observable from the data and can not be estimated independently.

The sensitivity analysis is performed by examining the change in the outputs due to a small one-by-one change in each input parameter. The smaller subset of variables identified by the Monte Carlo analysis is used here. The sensitivity is calculated numerically using central differencing. The plots in Figure 26 show the change in FIAT-predicted TC temperatures for a 1% change in each input parameter. Examining the shape and magnitude of these plots provides insight about the effect of each input variable on the outputs and also the degree of correlation between the input parameters. In addition to the sensitivity plots, the same results can be calculated in terms of correlation coefficients between the traces seen on the plots. For the sake of brevity, only the correlation table for TC1 (Table 5) has been provided here.

The magnitude of the sensitivity traces are lower for the deeper thermocouples and their maximum values happen at a later time. This is an indication of the damped and delayed nature of heat conduction problems. Examining the sensitivity plots and the correlation tables, a strong correlation between many parameters is observed. Some of these correlations are: between virgin specific heat and virgin conductivity and between char specific heat and char conductivity. There is also strong correlation between density and virgin specific heat and conductivity for the deeper TCs, and between density and char specific heat and conductivity for the top TCs. The reason for this behavior is that the heat transfer through the material is mainly driven by thermal diffusivity which is directly proportional to the thermal conductivity and

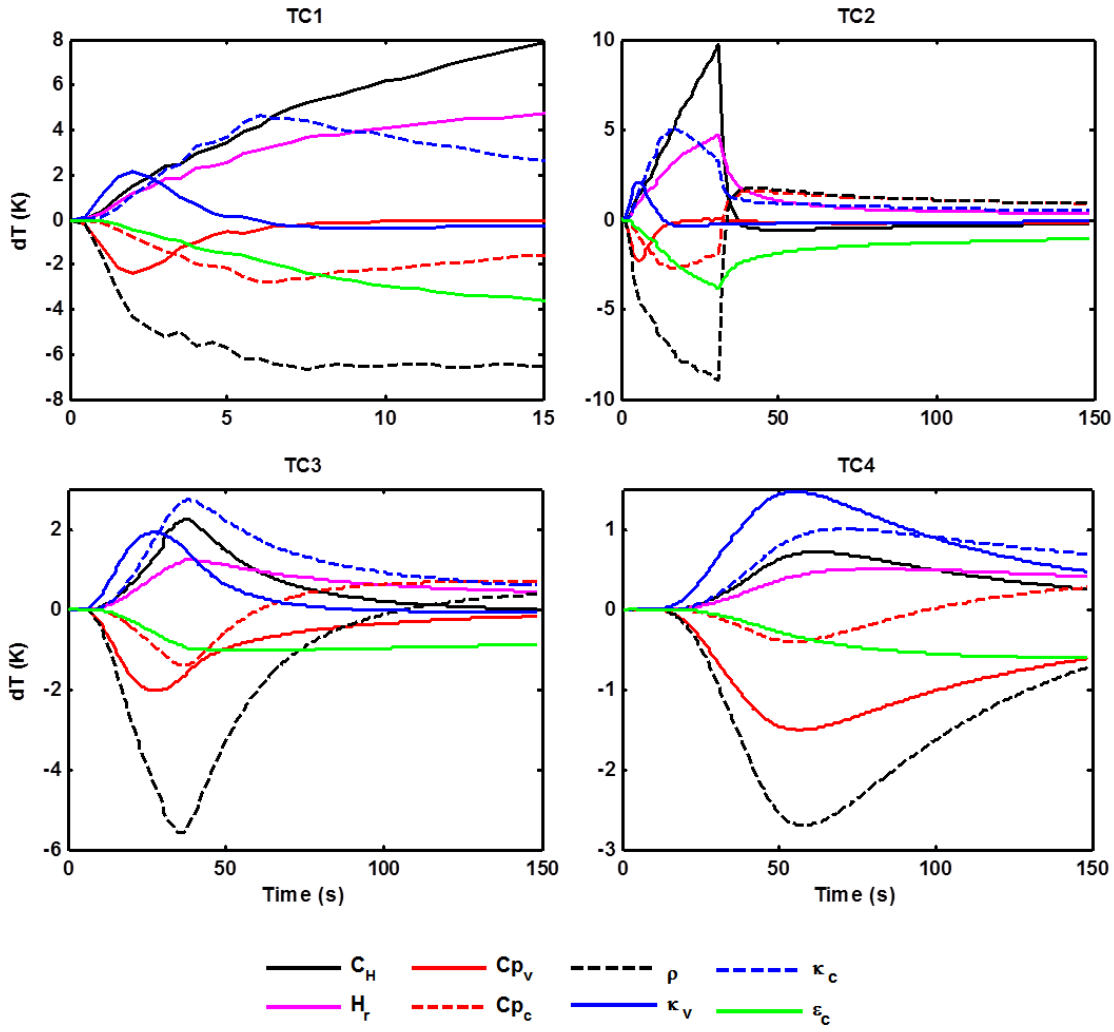

Figure 26: Sensitivity analysis results for the four subsurface thermocouples.

inversely proportional to the specific heat and density. In the FIAT governing equations, thermal conductivity always shows up as a quantity that is divided by the specific heat and density. Therefore increasing one or reducing the other one will have the same effect on the TC response. These strong correlations mean that in the presence of measurement errors these parameters cannot be simultaneously estimated. Different combinations of these parameters can result in similar objective functions in inverse analysis, specifically in the presence of noise.

It should be noted that the correlation trends observed here are problem dependent and the analysis has to be repeated for other applications. For example, if the surface

Table 5: Correlation coefficients showing the linear dependency between different parameters.

TC1	C_H	H_r	Cp_v	Cp_c	ρ	κ_v	κ_c	ϵ_c
C_H	1							
H_r	0.6913	1						
Cp_v	0.6708	0.6576	1					
Cp_c	-0.6285	-0.7220	-0.4245	1				
ρ	-0.8383	-0.8917	-0.3386	0.8745	1			
κ_v	-0.7243	-0.7299	-0.9850	0.5700	0.4679	1		
κ_c	0.6492	0.7406	0.4721	-0.9978	-0.8710	-0.6131	1	
ϵ_c	-0.9971	-0.9862	-0.7128	0.6097	0.8090	0.7596	-0.6347	1

heat rate was higher, recession and decomposition would be more significant than the conduction effects resulting in a smaller correlation between specific heat and thermal conductivity.

3.6 Inverse Analysis

The purpose of inverse analysis is to provide a better match between the data and FIAT predictions through the estimation of certain input parameters. This is accomplished by minimizing the sum of square of errors objective function using the inverse methods discussed in Chapter 2. The estimation results using the Gauss-Newton, Levenberg Marquardt, Box-Kanemasu and Conjugate Gradient methods will be compared. The parameters used here are the scaling factors for the subset of parameters identified by the previous steps (dimensional values normalized by the nominal value). Estimation of scaling factors instead of dimensional values is useful because it clearly shows the change from the nominal values without disclosing the actual values of restricted PICA material properties.

There are many different options for the range of the data to be used in the estimation process and the variables that should be estimated. The previous steps helped with intelligent selection of the data range and the estimation parameters. Considering the correlation between the specific heat and thermal conductivity observed in

the sensitivity analysis, these parameters can't be estimated simultaneously. Specific heat is typically known with more confidence than thermal conductivity since it is more difficult to measure thermal conductivity. Therefore, in this work it is assumed that specific heat is known with good confidence and thermal conductivity is estimated. There is also a strong correlation between material density and heat transfer coefficient. Since the density of material is straightforward to measure and typically known with more confidence, heat transfer coefficient is estimated while fixing density.

Table 6 shows multiple inverse analyses that were performed using different sets of estimation variables. In all cases, the initial guess for the parameters was the nominal values and then an inverse algorithm is employed to obtain a better estimate of these parameters by reducing the objective function. The sum of the square of errors objective function, S shown earlier in Eq. (12), can be also calculated in terms of the root-mean-square (RMS) error as shown in Eq. (24).

$$RMS = \sqrt{\sum_{i=1}^{4}\sum_{j=1}^{M}\frac{\left(Y_{ij}-T_{ij}\right)^2}{4M}} \tag{24}$$

RMS error has a more intuitive physical meaning because it has the units of Kelvin and is of the same order as the average difference between the TC temperatures and FIAT predictions. The RMS error is given for each inverse analysis. As shown in Table 6, the RMS error for the initial set of parameters (the nominal set) is about 51 K. The results show that this RMS error decreases through the estimation of the parameters.

It can be clearly seen from cases 1-6 that different parameter estimates can be obtained depending on what parameters are estimated. In Cases 1 and 2, only the heating parameters are estimated. The estimation of C_H alone in case 1 results in a significant reduction in the RMS value to about 20 K. In a single-parameter estimation approach, this might lead to the incorrect conclusion that an accurate estimation is obtained for the value of heat transfer coefficient. However, it is evident in case 2 that

Table 6: Inverse analysis results showing different parameter set estimations.

Case	Parameters	Method	Estimates	RMS (K)
	Initial		$[1 \cdots\cdots 1]$	**50.905**
1	$[C_H]$	Leven	[0.7645]	19.892
2	$[C_H,\ H_r]$	Leven	[0.8855, 0.8059]	17.050
3	$[\kappa_c]$	Leven	[0.7306]	14.476
4	$[\kappa_v,\ \kappa_c]$	Leven	[0.9377, 0.7380]	13.330
5	$[C_H,\ \kappa_v,\ \kappa_c]$	Leven	[0.9013, 0.9059, 0.8282]	9.705
6	$[C_H,\ H_r,\ \kappa_v,\ \kappa_c]$	Leven	[0.9021, 0.9844, 0.9016, 0.8375]	9.675
7	$[C_H,\ H_r,\ \kappa_v,\ \kappa_c]$	Conj	[0.9028, 0.9756, 0.8996, 0.8445]	9.687
8	$[C_H,\ H_r,\ \kappa_v,\ \kappa_c]$	Box	[0.9028, 0.9802, 0.9012, 0.8398]	9.676
9	$[C_H,\ H_r,\ \kappa_v,\ \kappa_c]$	Gauss	[0.9040, 0.9808, 0.9032, 0.8375]	9.678

once recovery enthalpy is simultaneously estimated, a further reduction is achieved in the RMS value and the parameter estimates change. Cases 3 and 4 show the same results but for the estimation of material properties alone. Case 3 illustrates the traditional approach that scales char thermal conductivity in order to match the arc jet data. Once aerothermal and material properties are simultaneously estimated in cases 5 and 6, the RMS value is reduced even further and the parameter estimates change.

These results clearly show the advantage of a comprehensive methodology for the intelligent selection of parameters and data range. Furthermore, the advantage of a multi-parameter estimation as opposed to the traditional single-parameter estimation is clear. Cases 7, 8 and 9 are the same as case 6, but the estimation is performed using the conjugate gradient, Box-Kanemasu and Gauss-Newton methods. These cases show that the estimation results are consistent across a range of minimization methods. Additionally, similar results are obtained if the estimation starts at a different initial guesses for the parameters.

The plots in Figure 27 and Figure 28 show the results for case 6. Figure 27 illustrates the TC measurements compared to FIAT predictions for both the nominal parameters and the best estimate parameters. Figure 28 shows the temperature

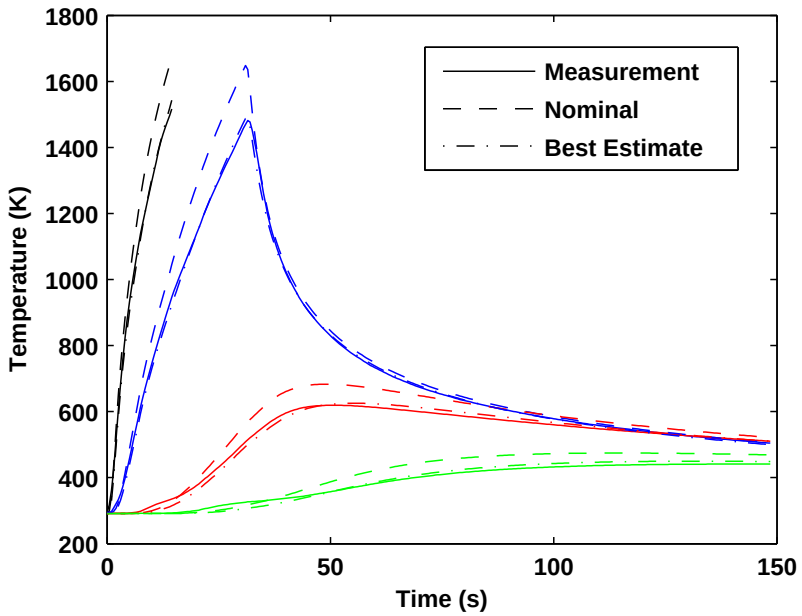

Figure 27: A closer match between the data and FIAT predictions is achieved through the inverse analysis.

residuals between FIAT predictions and TC measurements at the four thermocouple locations. A closer match with the data is obtained through the inverse estimation of parameters. The residuals for TC1 have been reduced from the original maximum of 150 K to within 30 K. The examination of residual plots is very important in inverse analysis. [103] The distribution of the residual errors provides information on model fidelity and sufficiency. If residuals are random and have no specific shape or bias, it is an indication that the model is sufficient and the errors are related to instrument measurement random errors. However, the presence of bias in the residuals indicates significant model structural error. For example, it is not a surprise that the residuals in Figure 28 are not random and have a biased shape, as it is known that FIAT has significant model error.

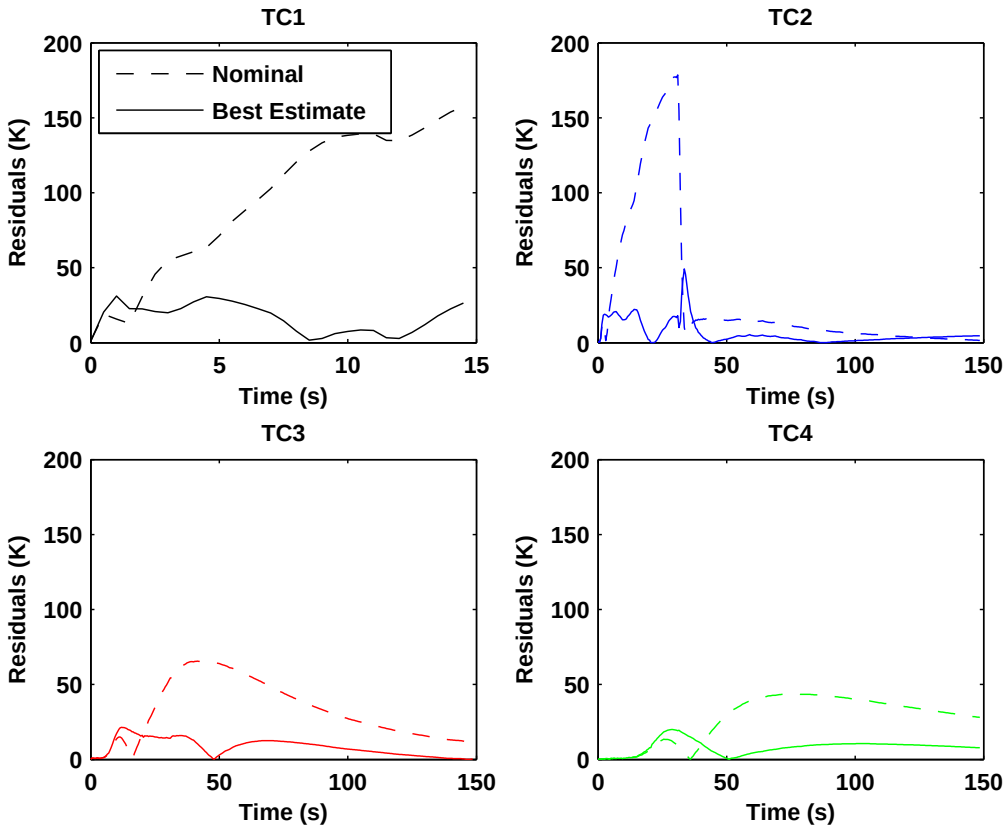

Figure 28: Nominal and best estimate residuals between data and FIAT predictions.

3.7 Summary

In this chapter, the developed multi-parameter estimation methodology is applied to a set of MISP-relevant arc jet data. Multiple analyses are performed in preparation for the inverse analysis. These steps provide the prerequisite information required in a successful inverse analysis. In the nominal analysis, the quality of the data is examined and possible sources of measurement errors are identified and corrected where possible. The nominal model predictions are compared to the data through a direct analysis to assess model error and identify areas where the model is fundamentally different than the experimental data. Based on these analyses, the region of validity for inverse analysis is determined.

In the uncertainty analysis, the contribution of many aerothermal parameters and

material properties to the uncertainty in the subsurface temperature prediction is calculated through a Monte Carlo analysis. This allows determination of a hierarchy of parameters and down selection from the original list to a subset of parameters that are significant for the inverse analysis. Simultaneous estimation of all these parameters can lead to incorrect results due to linear dependency between some parameters. Therefore, a sensitivity analysis is performed to determine the correlation between these parameters and identify which parameters can be simultaneously estimated. Finally, based on the information provided by these prerequisite steps, an inverse analysis is performed to obtain an accurate match between the model predictions and the data through the estimation of input parameters. The inverse analysis was performed for many different parameter subsets to illustrate the advantage of the multi-parameter estimation methodology as compared to the traditional single-parameter analyses.

CHAPTER IV

APPLICATION OF THE SURFACE HEATING ESTIMATION FRAMEWORK TO MARS HEATSHIELD DATA

4.1 Introduction

In arc jet environments, the surface heating conditions are often constant during the testing. However in a flight case, the vehicle aerothermal environment vary as a function of time. In this case, estimation of surface heating from subsurface thermocouple data is no longer a straightforward parameter estimation problem. The entire time-dependent profile for the surface heating needs to be estimated. This is a function estimation problem.

In this chapter, the surface heating function estimation framework, introduced earlier in Chapter 2, will be applied to simulated and flight Mars heatshield data. The objective is to demonstrate the feasibility of the developed framework in reconstructing time-dependent surface heating of entry vehicles. First, the estimation of MSL surface heating from simulated MISP data is investigated. Because the true solution is known for simulated problems, this analysis allows the examination of the effect of measurement and model errors on the accuracy of the estimated surface heating profile. Next, the same methods are applied to the Mars Pathfinder flight heatshield temperature data as a proof of concept with relevant Mars flight data.

4.2 Investigation of MSL Surface Heating Estimation from Simulated MISP Data

In this section, the estimation of MSL time-dependent surface heating from simulated MISP data is investigated. Multiple cases are examined where different types of model and measurement errors are simulated to determine the effect of such errors on the accuracy of the estimated heating profile. A known heating profile is used to generate the simulated data. Similar to all inverse problems, the MSL surface heat rate estimation problem has three parts: direct model, estimation parameters, and simulated data. Like the previous analyses, the direct model used in this work is FIAT.

4.2.1 Estimation Parameters

As described earlier in Chapter 2, heat rate is not a direct input to FIAT for ablative materials. Therefore, the time-dependent surface heat transfer coefficient profile, C_H, is estimated from the temperature data. Once the heat transfer coefficient is estimated, the surface heat rate can be calculated using other parameters in the surface energy balance. Please refer to Chapter 2 to review the discussion of surface energy balance terms for ablative material modeling.

In this study, the time-dependent C_H profile is discretized every 1 second. This discretization is a balance between the desire to have a higher resolution C_H profile, computational resources and the stability of the inverse methods. Figure 29 shows a plot of the nominal heat rate and heat transfer coefficient for two plug locations, T2 and T4 (highest and lowest heating) for the entire MSL trajectory. These surface conditions were calculated using the CFD code DPLR from MSL's nominal design trajectory. [9] This study limits the estimation of the surface conditions for the time range where heat rate is approximately greater than 1 W/cm^2, which corresponds to the time range shown with the black vertical lines (20-150 s).

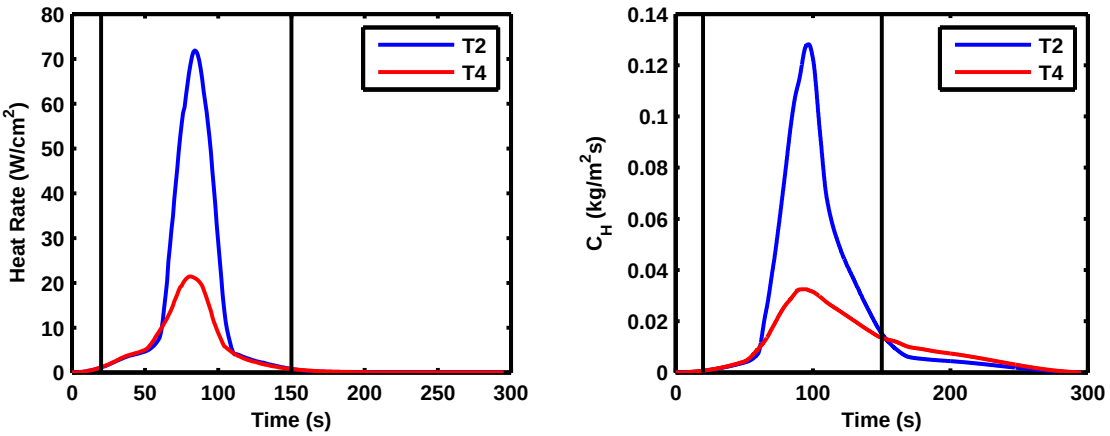

(a) Heat Rate (b) Heat Transfer Coefficient

Figure 29: The nominal CFD-calculated surface heating conditions for T2 and T4 locations showing the estimation range.

4.2.2 Simulated Data

MISP consists of seven plugs at different locations on the heatshield each containing four thermocouples (TC) and an isotherm sensor. In this work, the analysis is limited to the plugs that are expected to experience the highest and lowest surface heating, T2 and T4 respectively, to bound the range of surface heating expected by MISP plugs in flight. The top two TCs are closest to the surface and therefore are most sensitive to the boundary conditions. Furthermore, the actual flight data will carry some bias due to the uncertainty in the material properties. The deeper TCs are affected more by the material properties. For these reasons, only the top two TCs are used in this work for estimation of surface conditions. For plug T2, the recession front reaches the top TC; therefore, the simulated data for this TC is only used up to the vicinity of the burnout point.

Figure 30a shows a plot of the simulated measurements as a function of time for both plug locations. These measurements were simulated using FIAT and the current nominal heating and material parameters for the MSL vehicle. This plot shows the measurement without any noise/errors. Simulated random and bias noises can be

added to the data to study their effect on the estimation results. Random errors are sampled from a normal distribution with a mean of zero and standard deviation of 0.5% of TC temperature, and are added to the simulated data. Figure 30b shows an example of simulated noisy data for the T4 location.

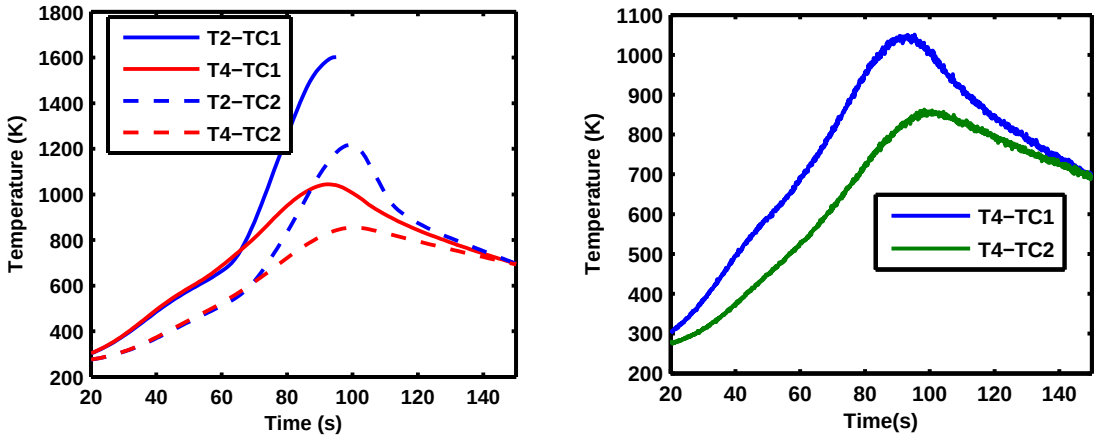

(a) Noise-free data

(b) Noisy data (T4)

Figure 30: Simulated TC measurements for the two plug locations.

An example of data bias error is TC thermal lag. Thermal lag is implemented by lagging the simulated TC temperatures using a simple lump capacitance model for an infinitely long wire. At any time step, given the current temperature of the host material (original simulated TC temperature) and the initial wire temperature, the heat transferred from the host material to the wire can be calculated for a given contact conductance, h_c, wire properties, volume and surface area. The change in wire temperature for the current time step is then solved using the equation below:

$$\left[\rho C_P V \frac{\Delta T}{\Delta t}\right]_{wire} = h_c A_s \left(T_{host} - T_{wire}\right) \tag{25}$$

For this problem, the properties of a type-K thermocouple are used for the wire properties. Figure 31 shows the lagged TC measurements for different contact conductance values for plug T4. It can be seen that higher contact conductance, h_c, results in smaller thermal lag in the TC measurements. In this work, whenever thermal lag is added to the data, a nominal contact conductance of 350 W/m^2K is used.

The effect of varying this parameters on the estimation results are shown later for plug T4.

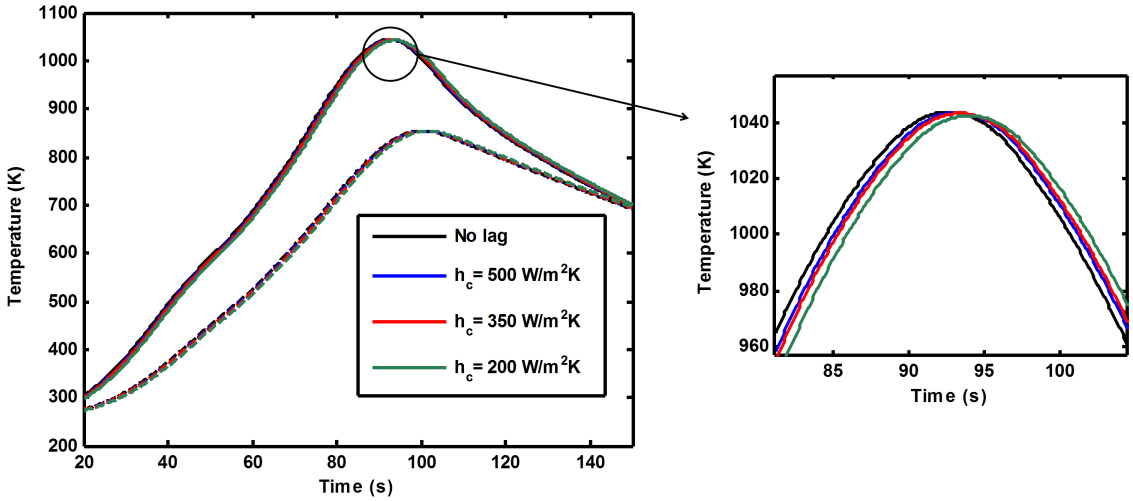

Figure 31: Implementation of TC thermal lag using a simple lump capacitance model for plug T4.

4.2.3 Investigation Process

The TC measurements are simulated using the nominal surface conditions and PICA material response model. The surface C_H profile that generates this data is taken to be the truth or known solution. A simple Gaussian function is used for the initial guess. As shown in Figure 32, this initial guess looks very different from the known solution and it does not have some of the asymmetry present in the known solution curve. The effect of using a different initial guess is shown later for one of the cases.

The investigation process begins with simulation of the TC measurements using the nominal C_H profile and nominal material response model. The simulated data are then used either in this form or with added noise and thermal lag. Once the data is generated, the inverse method starts with the initial guess and estimates the C_H profile that achieves the best match between the TC temperature predictions and simulated data. This is done by iterative minimization of the sum of square of errors between the TC predictions and simulated measurements. This process is

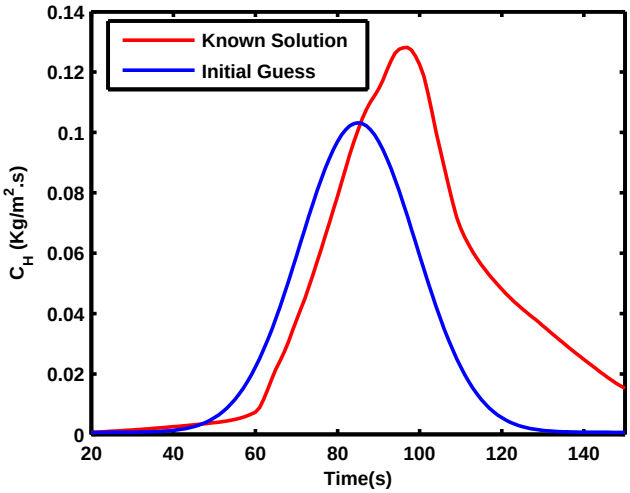

Figure 32: Initial guess compared to the known solution for plug T2.

continued until convergence is reached and the best-estimate C_H profile is obtained. In addition to random noise and thermal lag, the effect of material property bias on the estimation results is also investigated. This is done by simulating the measurements with a perturbed material response model while performing the estimation using the nominal model. It simulates the situation where our knowledge of material properties is inaccurate, which is expected for flight data. For this study the material response model is perturbed by increasing PICA density (all components) by 10% or decreasing thermal conductivity by 10%.

The estimated C_H profiles and the corresponding reconstructed surface heat rate are compared to the known solutions. Another criterion used for comparison is the Normalized Absolute Difference (NAD), which is the absolute difference between the known solution and best-estimate C_H profiles as a percentage of the peak C_H value (shown in Eq. (26)). This criterion is used instead of percent error because a small absolute error when the C_H value is small itself could lead to a large percent error. This criterion can be similarly defined for surface heat rate. Another criterion used for comparison is the Relative Integrated Error (RIE) which is the integrated square of differences between the nominal (known solution) and best-estimate C_H profiles as

a percentage of the integrated square of the nominal C_H profile (shown in Eq. (27)). This criterion can be similarly defined for the surface heat rate.

$$\text{Normalized Absolute Difference} = 100 \times \frac{\left(C_H^{BE} - C_H^{Nom}\right)}{max\left(C_H^{BE}\right)} \tag{26}$$

$$\text{Relative Integrated Error} = 100 \times \frac{\int \left(C_H^{BE} - C_H^{Nom}\right)^2 dt}{\int \left(C_H^{BE}\right)^2 dt} \tag{27}$$

4.2.4 Inverse Estimation Method

A discussion of the inverse methods used for the estimation of time-dependent surface heating is provided in Chapter 2. Here, the Gauss-Newton method is employed to minimize the sum of square of errors objective function. Tikhonov first-order regularization technique is used to make the problem better posed and alleviate oscillations in the estimated heat rate profile.

The minimization procedure is continued until a stopping criterion is reached. A range of convergence criteria can be used for this problem. Iteration can be stopped when S reaches a small number or when the percent or absolute change in S is small. Another criterion could be to stop the iteration once the absolute or percent change in estimation parameters is smaller than a specified value. A maximum number of iteration is another termination criterion. In this investigation, the iterations are continued for a specified maximum number and the best estimate is taken when the solution is stable. The maximum number of iterations is set to 200 to make sure that a converged solution is reached. The regularization parameter values, μ, that worked for this problem ranged from 10^9 to 10^{12}. This might seem large compared to the values seen in literature, but most of the work in literature involves the estimation of heat rate which is orders of magnitude greater than C_H. In the case of simulated data with no noise, regularization was not needed and an almost perfect estimate was obtained using the Gauss-Newton method alone.

4.2.5 Implementation and Results

Figure 33 shows the estimation results for the simulated data without any noise. Only normalized absolute difference is shown here because the best estimate profile is almost the same as the known solution. It is evident that the C_H profile is estimated very well and the normalized absolute difference is very close to zero across the profile, with errors in the order 10^{-5} %.

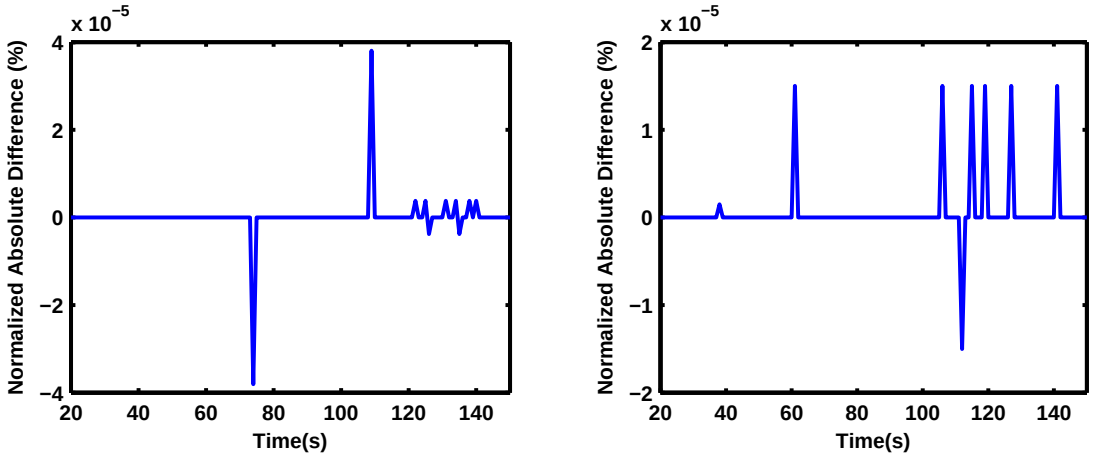

(a) Plug T2 (b) Plug T4

Figure 33: Error in the best estimate C_H profile for the case of simulated data without noise.

These results are obtained with the Gaussian initial guess. In order to study the effect of the initial guess on the estimated profile, the estimation is also repeated for a constant C_H initial guess (10% of the peak C_H value) for the T2 location. Figure 34 compares the estimation results and convergence behavior for these two initial guesses. The Gaussian initial guess is labeled as "Gaussian IG" while the constant 10% initial guess is labeled as "Constant IG". It is evident that in both cases the estimated profile is close to the known solution and similar estimates are obtained. However, as expected, a more difficult initial guess takes longer to converge. The right plot shows that the Gaussian initial guess case takes 7 iterations to converge while the constant initial guess case takes 24 iterations.

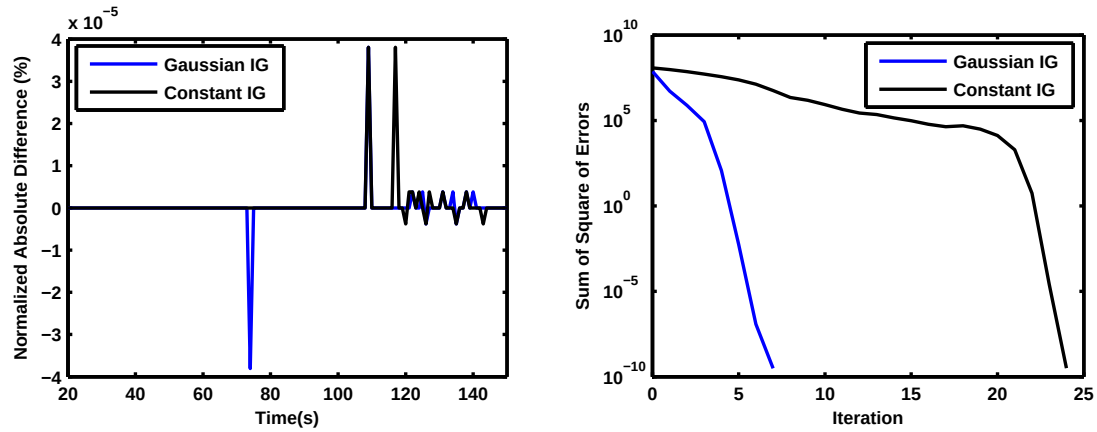

(a) Error (b) Convergence behavior

Figure 34: The effect of initial guess on the estimation results and convergence behavior.

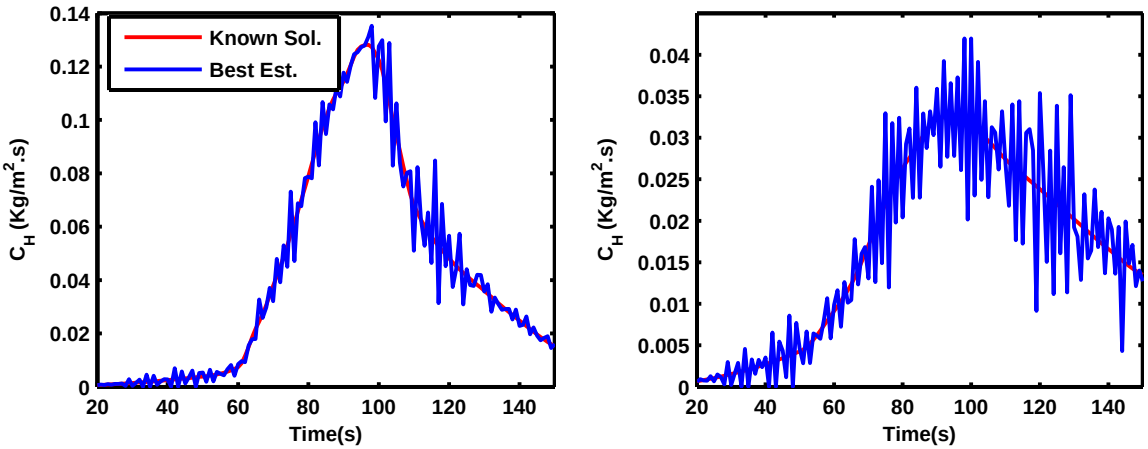

(a) Plug T2 (b) Plug T4

Figure 35: Estimation in the case of simulated data with random noise with no regularization.

Figure 35 shows the estimation result for the case of simulated data with random noise for both plug locations. Without regularization, the solution is oscillatory. Figure 36 shows the results for the same estimation performed with Tikhonov regularization. The oscillations have been substantially reduced and the best-estimate C_H profile is very close to the known solution. Figure 36b shows the residuals between best estimate temperature predictions and the measurements. As expected, it can be seen that the difference in temperatures after estimation is random around zero,

and with similar distribution as the added random noise to the data. Figures 36c & d illustrate the normalized absolute difference between the best-estimate and known solution C_H profiles for both plug locations. It is clear that even in the presence of relatively substantial random noise the estimation results are within 1% of the peak value.

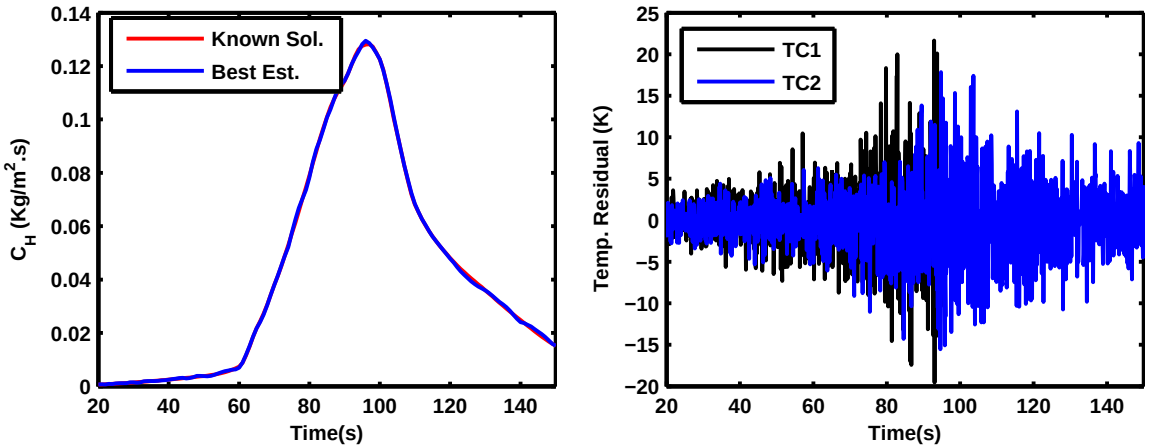

(a) T2 C_H profile

(b) T2 Temperature Residuals

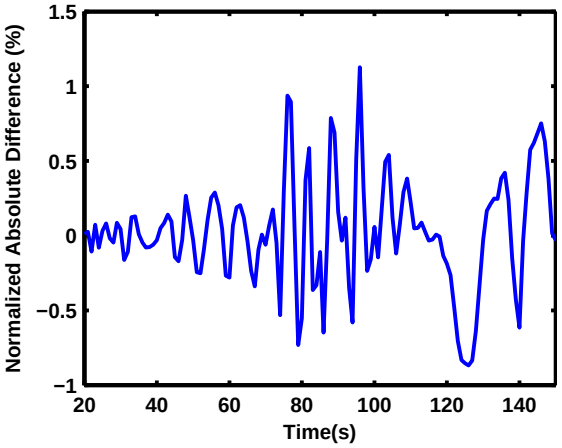

(c) T2 error

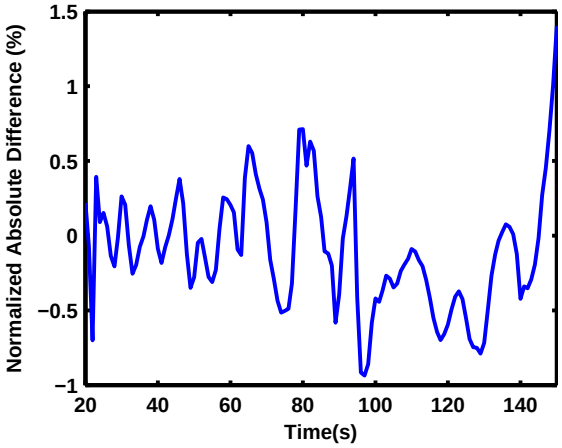

(d) T4 error

Figure 36: Estimation results in the case of simulated data with random noise with regularization.

In Figure 37, the effect of regularization parameter on the estimated profile for plug T2 is presented. The estimation is performed for two values: 10^9 and 10^{11}.

It can be observed that the estimate for the higher regularization parameter is less oscillatory. Comparing these results with the unregularized estimate ($\mu = 0$) shown in Figure 35, it is clear that increasing μ reduces the oscillations in the solution. However, it should be noted that there is a diminishing return where high values of μ over-penalize the solution and substantially slow down the reduction of the objective function and solution convergence. Therefore, a good strategy for the selection of the regularization parameter is to increase it until the oscillations in the final estimate have been reduced enough and the estimate still traces the general trend of the unregularized estimate closely. The results for the remaining cases are shown only for the regularized estimates, but the same trend is observed.

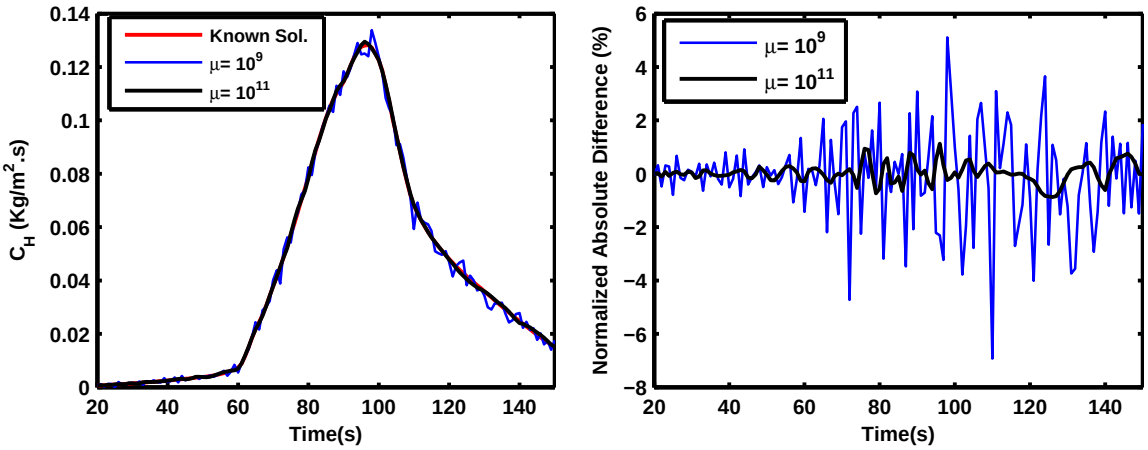

(a) C_H profile

(b) Error

Figure 37: The effect of regularization parameter on the estimation results for Plug T2.

Figure 38 demonstrates the estimation results for the case of simulated data with thermal lag for both plugs. The simulated data are lagged with a thermal conductance of 350 W/m^2K. Thermal lag in the data is a bias error and it can be observed that there is a bias error in the estimated C_H profile. The estimated profile lags the original C_H curve the same way the simulated TC measurements lag the original

TC measurements. The lag is more pronounced on the decreasing half of the C_H curve because the effective heat rate is lower compared to the increasing side (see Figure 29).

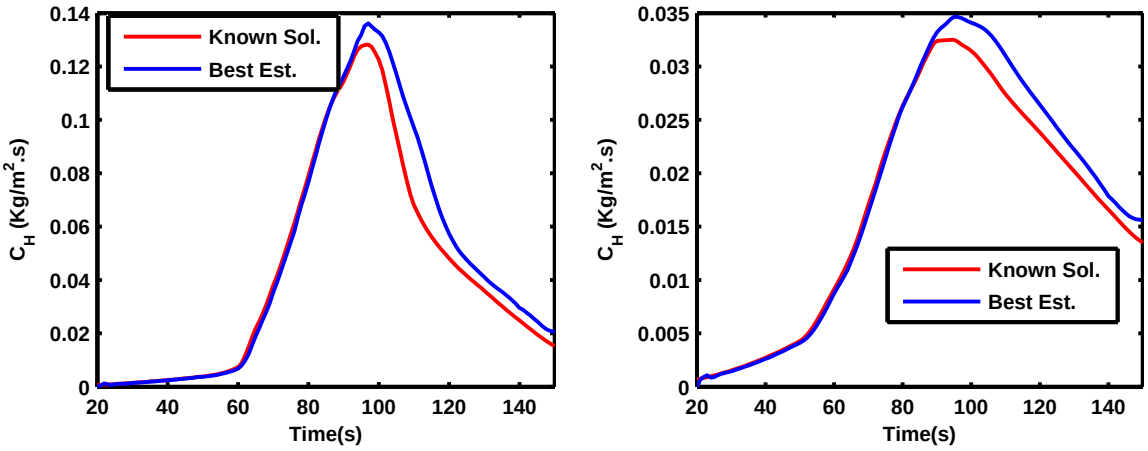

(a) Plug T2 (b) Plug T4

Figure 38: Estimation results in the case of data with thermal lag.

In Figure 39, the estimation is performed for the simulated data with thermal lag at plug T4 for three different values of contact conductance. This is done to show the effect of the magnitude of thermal lag on the estimated C_H profile. It was shown earlier that the thermal lag in the simulated data increases with a lower contact conductance (Figure 31). As expected, the higher lag in the subsurface thermocouple data results in a larger bias error in the estimated surface C_H profiles. The estimated profile lags the original one in the same way that the lagged data lags the original simulated data. Estimated C_H is initially lower than original C_H and then it crosses over and exceeds the original curve after about 80 s. The results from Figures 38 and 39 confirm that a large thermal lag in the TC data could result in a large error in the estimated profile. Therefore, in the case of the analysis of flight data, it is best to model TC lag as accurately as possible, either implementing this effect within FIAT or correcting the data.

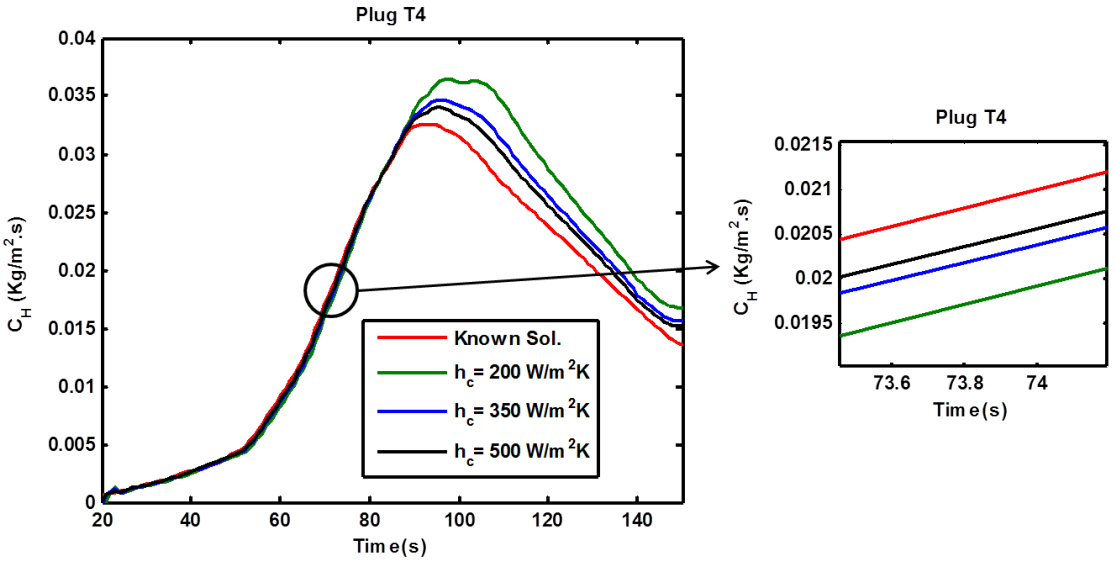

Figure 39: The effect of contact conductance in lag modeling on estimation results for plug T4.

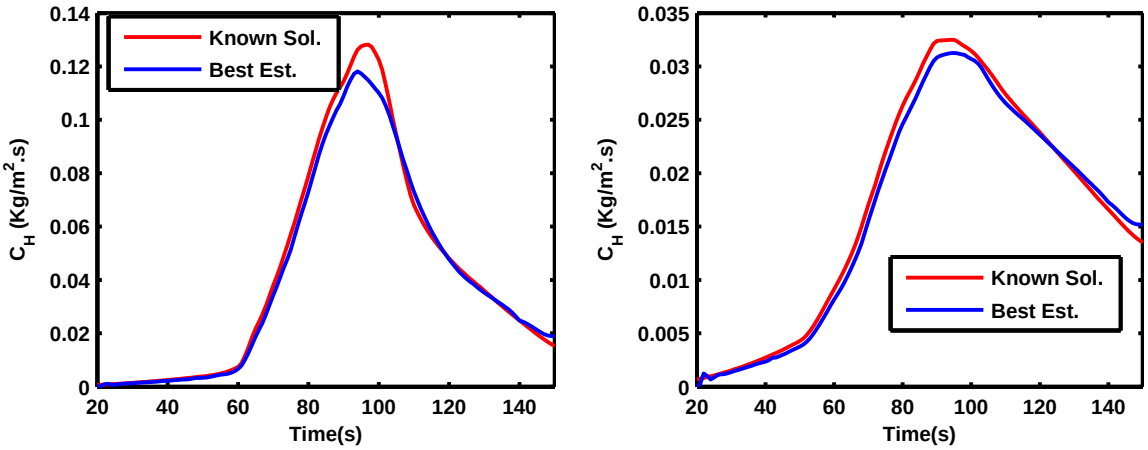

(a) Plug T2

(b) Plug T4

Figure 40: Estimation results in the case of data with PICA density perturbation.

Figure 40 demonstrates the effect of the PICA density perturbation on estimation results for both plugs. In this case, the data is simulated using a perturbed PICA thermal response model with 10% higher density (all components for virgin and char) and then the nominal response model is used in the estimation of C_H curve. C_H and

material density have similar but opposite effects on the in-depth material temperature response. Generally, higher surface C_H results in higher subsurface temperatures while higher material density results in lower subsurface temperatures. Therefore, if a lower density material model is used in the estimation process compared to the one used to generate the data, the predicted subsurface temperatures will be higher, and the estimated C_H will need to be lower to compensate for the higher subsurface temperatures. This is exactly what is seen in the estimation results, showing that a strong linear dependency between C_H and material density results in a direct translation of the bias error in material density to a bias error in estimated C_H profile.

Figure 41 shows the effect of the PICA thermal conductivity perturbation on the estimation results for both plugs. The simulated data are generated with a material model with 10% lower conductivity (virgin and char) and then the original material model (higher conductivity) is used in the estimation process. Higher conductivity

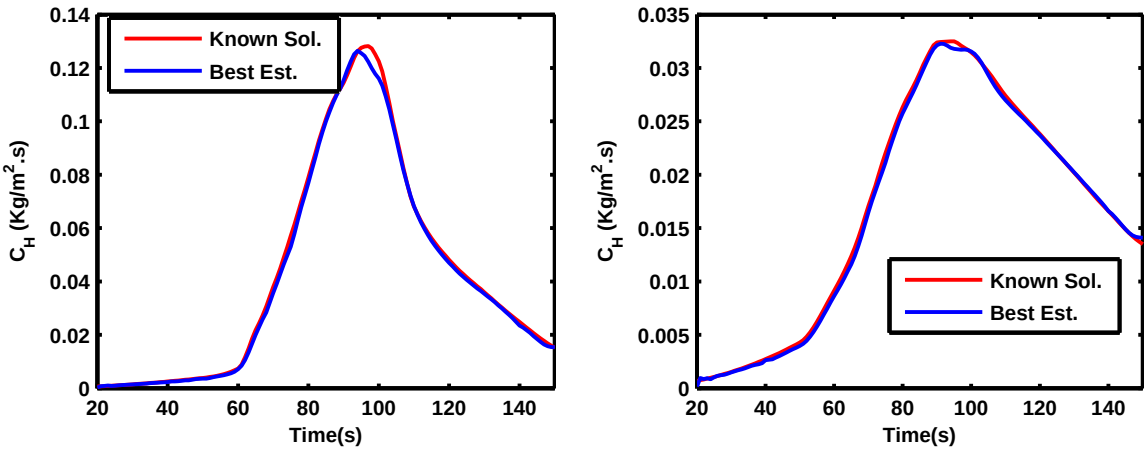

(a) Plug T2 (b) Plug T4

Figure 41: Estimation results in the case of data with PICA conductivity perturbation.

results in higher predicted subsurface temperatures and a bias error in the estimated C_H profile should be expected. However, C_H and thermal conductivity are not as linearly dependent as C_H and density; therefore, even though there is a bias error

in the estimated profile, this bias is not as large as in the density perturbation case. In other words, due to the lower linear dependency between C_H and conductivity, a large reduction in C_H profile does not completely compensate for the bias error in the data, and the estimated profile is closer to the original curve.

Figures 42 and 43 show the estimation results for both plugs for the simulated data with random noise, thermal lag ($h_c = 350\ W/m^2K$) and material property bias (density perturbation). The estimated C_H profile shows a combination of lag and material property biases. These errors result in a C_H profile that is not exactly the same as the profile used to generate the data.

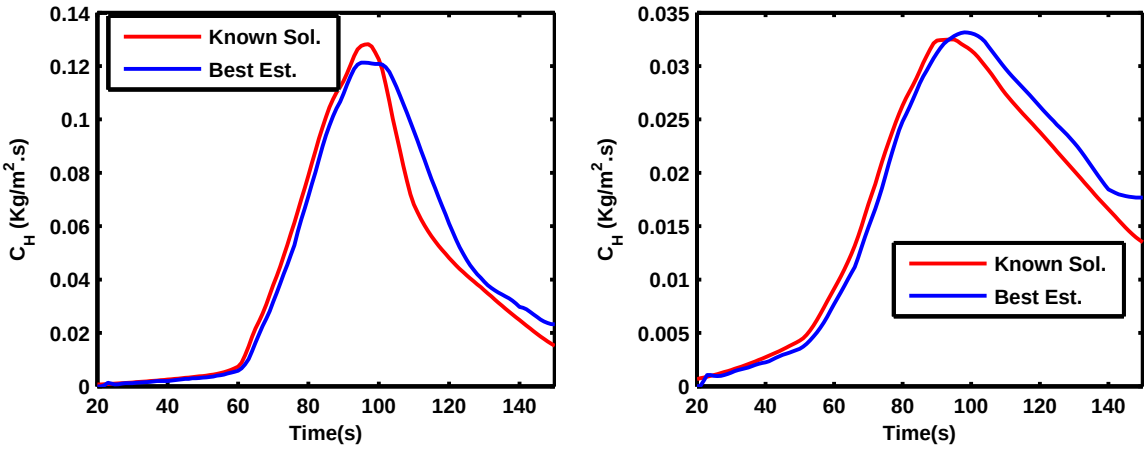

(a) Plug T2

(b) Plug T4

Figure 42: Estimated C_H profile in the case of data with combined errors.

Surface heat transfer coefficient is the parameter that is estimated in this study because the surface heat rate is not a direct input for ablation modeling in FIAT. All the results above were shown for the reconstructed C_H profile. Once the surface C_H is estimated, the heat rate can be calculated by adding the surface convective heating term and the chemical heating term from FIAT outputs (as shown in Eq. (18)). The reconstruction of the surface heat rate is of the primary concern for the MEDLI post-flight analysis and the reconstruction accuracy requirements are stated for heat

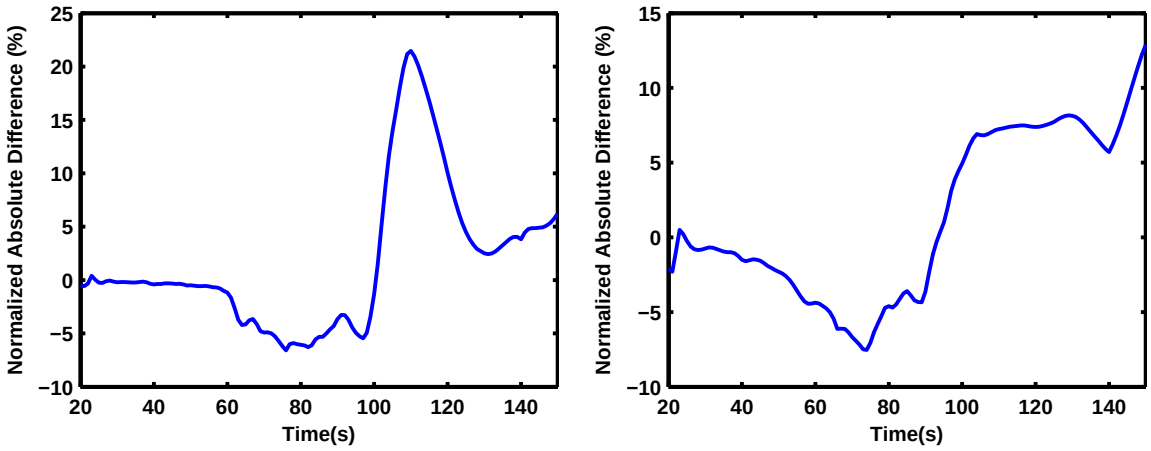

(a) Plug T2 (b) Plug T4

Figure 43: Estimated C_H normalized absolute difference in the case of data with combined errors.

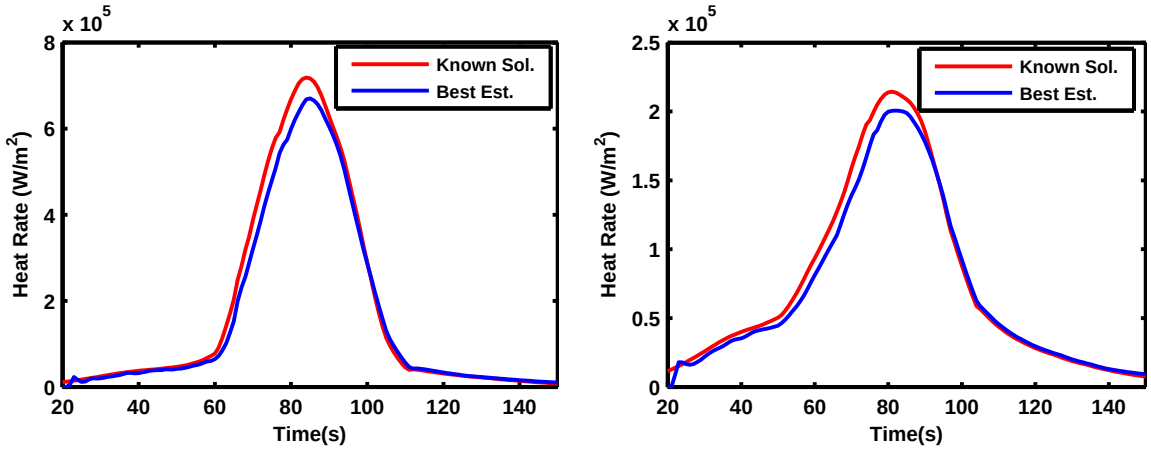

(a) Plug T2 (b) Plug T4

Figure 44: Estimated surface heat rate for the case of combined errors.

rate not C_H. Therefore, in this study, the final accuracy criteria will be given for the surface heat rate. Figures 44 and 45 show the reconstructed surface heat rate for the case with combined errors for both plugs (corresponding to C_H estimation in Figure 42). The difference between the known solution and best estimate profiles look somewhat different from the trends observed for C_H profiles mainly due to the fact that the peak times are shifted for these two variables. Based on these results, it can be stated that the errors in heat rate profile are smaller than C_H profile.

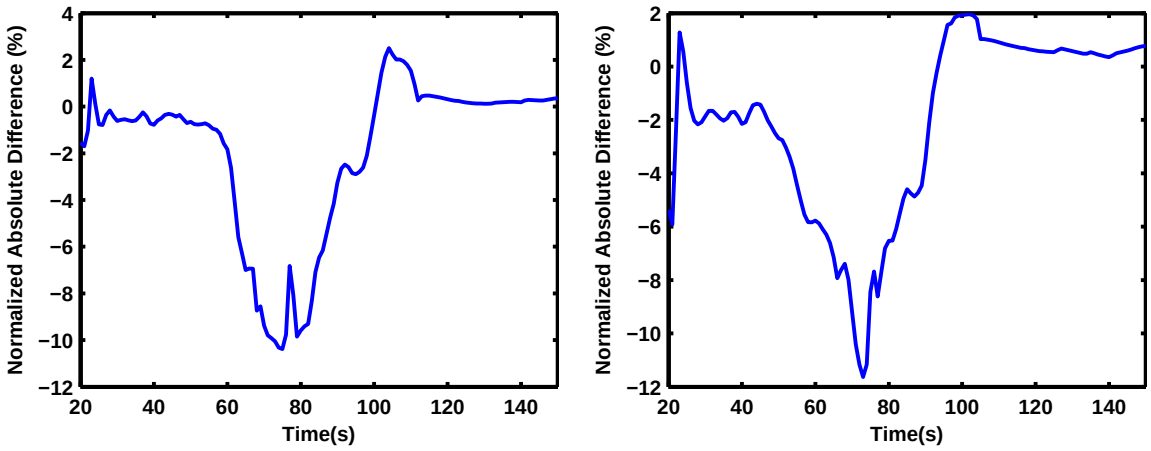

(a) Plug T2 (b) Plug T4

Figure 45: Estimated surface heat rate normalized absolute difference for the case of combined errors.

Table 7: Accuracy of surface heat rate estimation in the presence of different types of errors.

	Plug T2		**Plug T4**	
	NAD Range (%)	RIE (%)	NAD Range (%)	RIE (%)
No Noise	[-6 e-5, 1 e-5]	2.0 e-12	[-1 e-5, 5 e-5]	2.0 e-13
Random Noise	[-1.2, 1.5]	0.0070	[-0.7, 1.0]	0.0061
Thermal Lag	[-4.0, 3.0]	0.1727	[-3.5, 3.5]	0.1143
ρ **Perturbation**	[-7.5, 0.5]	0.5230	[-8.0, 0.5]	0.4986
κ **Perturbation**	[-5.0, 1.2]	0.1076	[-3.5, 0.5]	0.0909
Combined Errors	[-10.5, 2.5]	0.9151	[-11.0, 2.0]	0.6084

Table 7 provides a summary of the accuracy of the heat rate estimation results. These estimation accuracy criteria are shown for both plugs for the six cases studied: no error, random noise, TC thermal lag, density perturbation, conductivity perturbation and the combined error cases. In addition to the observations made for each case, it can be seen that the estimation results for T2 are generally less accurate than T4. This is expected due to the fact that the top TC burns around 95 seconds for T2 and less thermocouple data is available for the rest of the period. Because the lower thermocouples are deeper and less sensitive to the surface conditions, T2 estimation is more prone to uncertainty than T4. The heat rate error for the combined case is

in the order of 10%. In this case, multiple measurement and model errors are added to the estimation process which results in their individual effects to compile.

4.2.6 Summary

The estimation of MSL surface heat transfer coefficient from simulated subsurface temperature data was investigated. The whole-time domain Gauss-Newton least square minimization method in conjunction with Tikhonov first-order regularization was used to perform the estimation. The performance of the inverse method and the accuracy of the estimated boundary conditions were investigated in the presence of measurement errors such as random noise, TC thermal lag and model bias errors such as TPS material density and thermal conductivity perturbation. These study results inform the level of accuracy with which the surface conditions can be reconstructed from subsurface temperature measurements using inverse techniques.

It was observed that regularization was crucial in reducing oscillations in the estimated C_H profiles. Regularization was required in order to obtain a smooth estimate in all cases, except the case without any errors. A good estimate was obtained in the case of data with random noise. Bias errors in the data such as TC thermal lag resulted in a large bias in the estimated boundary conditions. This demonstrates the necessity of implementing accurate lag models in FIAT or correcting the TC data for thermal lag.

A simple capacitance model was used in this study to simulate TC lag; nevertheless, this analysis can be repeated once more accurate Finite Element Analysis (FEA) lag modeling or experimental lag data is available for the MISP plugs. Bias error in the model, such as PICA density or conductivity perturbations, resulted in a bias in the estimated surface C_H profile. Such bias is larger in the case of density perturbations compared to conductivity perturbations. This is due to the stronger linear dependency between C_H and material density.

4.3 Mars Pathfinder's Surface Heating Estimation from its Heatshield Flight Data

In this section, the developed methods are applied to the Mars Pathfinder flight temperature data. Unfortunately in the case of Pathfinder, thermocouple data were available only at a single depth at different locations on the heatshield. As a result, this analysis is limited to estimation of time-dependent surface heating from the subsurface temperature data, excluding the estimation of material parameters.

Mars Pathfinder entered the atmosphere of Mars on July 4, 1997. The entry vehicle was a 70° spherecone with a 46.6° conical backshell. The forebody heatshield material was SLA-561V, with a nominal thickness of 1.90 *cm*. The aeroshell was equipped with nine type-K thermocouples and three platinum resistance thermometers at different depths and locations in the heatshield and backshell. Milos et al. [5] performed Navier-Stokes heating calculations for the Pathfinder entry vehicle using the CFD code GIANTS. They calculated the heatshield material response using three different one-dimensional charring models and directly compared the subsurface temperature flight data and the material response results. The main conclusion of that work was that the stagnation point temperature data was consistent with CFD assuming about 85% of fully catalytic laminar heating. Also, the shoulder temperature data was consistent with fully catalytic laminar heating with early onset of turbulence. The bondline temperature data were not of good quality for quantitative analysis and differed greatly from the model predictions.

Building on the work of Ref. [5], the Pathfinder entry vehicle's aerothermal heating is reconstructed here using updated modeling tools and approaches in both direct and inverse manners. In the direct analysis, a newly estimated trajectory is used which is believed to be closer to the flight trajectory. Based on this new trajectory, updated CFD calculations are performed to characterize the vehicle's heating conditions. The heating boundary conditions are then used with FIAT to calculate the

in-depth material response at TC locations. In the inverse analysis, Pathfinder's heat transfer coefficient profile is estimated at the stagnation and shoulder locations from the thermocouple data using the methods described in the previous section. This work advances our knowledge of the Mars Pathfinder aerothermodynamic environment and TPS material response by employing: (1) a newly reconstructed trajectory and associated CFD simulations, (2) updated SLA thermal response and ablation model and (3) inverse analysis in addition to direct comparison.

4.3.1 Description of the Mars Pathfinder Flight Instrumentation

The Mars Pathfinder Aeroshell contained nine type-K thermocouples (TC1-TC9) and three platinum resistance thermometers (PRT1-PRT3). Figure 46 from Ref. [5] shows a profile view of the aeroshell and the location of the TCs and the PRTs. The PRTs were attached to aluminum blocks and served as isothermal reference junctions for the nine TCs. The TCs were placed at different locations and depths in the TPS material. Reference [5] provides tables detailing the material stack-up at each TC location. There are a number of challenges in the application of this flight data. TC1, TC7

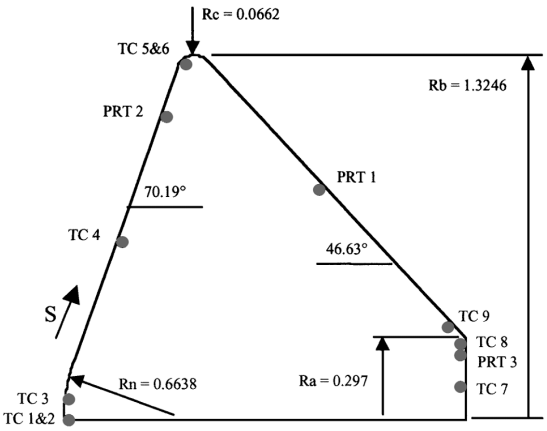

Instrument	r, cm	S, cm	Depth, cm
T1	0.00	0.00	0.400
T2	0.00	0.00	0.953
T3	7.62	7.64	1.905
T4	66.44	69.7	1.905
T5	130.4	138.0	0.953
T6	130.4	138.0	1.905
T7	12.0		0.038
T8	27.6		0.038
T9	34.0		0.038
PRT1	83.9	212.5	1.340
PRT2	110.0	(inside structure)	
PRT3	23.5	(inside structure)	

Figure 46: Pathfinder instruments locations and depths.

and TC8 did not return any usable data. In addition, the temperature data returned from TC2-6 are known to be incorrect due to the fact that PRT2 measurements were pegged at the low-temperature cutoff of the calibration curve and were used for the

TC data reduction. Reference [5] explains how results from the solar thermal vacuum tests were used to correct the TC data. The conclusion was to uniformly subtract 18 $\pm$ 2 K from the temperature measurements for TC2-TC6. The analysis done by Milos et al. [5] suggests that the data returned from the bondline thermocouples (TC3, 4 and 6) did not match the temperature profiles predicted by the thermal response models. The measured temperature abruptly rises, then changes slope and shows no resemblance to the predictions. As mentioned in the previous chapter, this unusual TC pre-heating behavior has also been seen in arc jet and thermal flash tests and can be attributed to evaporation of absorbed moisture [137] or direct transmission of thermal radiation to the bondline. [5] As a result, the focus of this study will be on the mid-TPS thermocouples at the nose, TC2, and at the shoulder, TC5.

4.3.2 Direct Analysis

The previous Mars Pathfinder analysis performed in Ref. [5] employed a trajectory reconstructed by Spencer et al. [111] In this work, a new three degree-of-freedom reconstructed trajectory by Dutta et al. [113] is used. This reconstruction is based on a backward estimation approach which processes the data from sensors with lower uncertainty such as the altimeter earlier in the estimation. The backward estimation also has the advantage of not containing the discontinuity jumps that are typically observed in forward trajectory estimations when the altimeter data becomes available.

Based on this trajectory, CFD simulations are performed for the vehicle using the DPLR code and current models for the Martian entry (explained in Chapter 1). The CFD simulations presented here were performed by Todd White from NASA Ames Research Center [93] using a similar methodology as described in Refs. [9, 139]. DPLR is a modern, parallel, structured non-equilibrium Navier-Stokes flow solver developed and maintained at NASA Ames Research Center. [43, 140] The code employs a modified Steger-Warming flux-splitting scheme, for higher-order differencing of the

inviscid fluxes, and is used here with 2^{nd} order spatial accuracy and to steady-state 1^{st} order in time. [9] DPLR has been validated over a wide spectrum of flight and ground-based experimental simulations. The flow around the heatshield is modeled as thermochemical non-equilibrium flow, using the Mitcheltree and Gnoffo 8-species 12-reactions Mars model (CO_2, CO, N_2, O_2, NO, C, N, and O). [24] The Mars atmosphere is modeled as 97% CO_2 and 3% N_2 by mass. The TPS surface is modeled as an unblown non-slip radiative equilibrium wall with constant emissivity and Mitcheltree surface catalycity model. [41] Species diffusion is modeled using the Self-Consistent Effective Binary Diffusion (SCEBD) method. [141] Turbulent flow is simulated via Menter's SST vorticity-based turbulence model. [28] The Wilcox blended compressibility correction [46, 29] is used.

A total of 21 points along the trajectory are used for CFD analysis, spanning the time range of 25 s to 150 s. Early in the trajectory the flow is expected to be non-continuum; therefore, Navier-Stokes solutions are not obtained earlier than 25 seconds. The freestream temperature is taken from a separate atmospheric reconstruction done by the Atmospheric Structure Investigation/Meteorology (ASI/MET) experiment science team. [142] For the following analysis, the flow is solved axisymmetrically which enforces a zero angle of attack and sideslip. The grid employed has 160 cells along the body, and 128 from the surface to the freestream. Each simulation includes several grid alignments to adapt the shock to the strong bow-shock. Figure 47 shows the flowfield temperature distribution at the peak heating point, and laminar and turbulent surface heating predictions. Heating from shock-layer radiation at the stagnation point is calculated using the same technique as Refs. [5, 143], and is neglected at the shoulder.

Surface conditions for material response simulations are extracted from the CFD solutions at the stagnation point and shoulder locations (wetted lengths of 0.00 and 138.0 cm, respectively). These quantities are then fit in time with tight monotonic

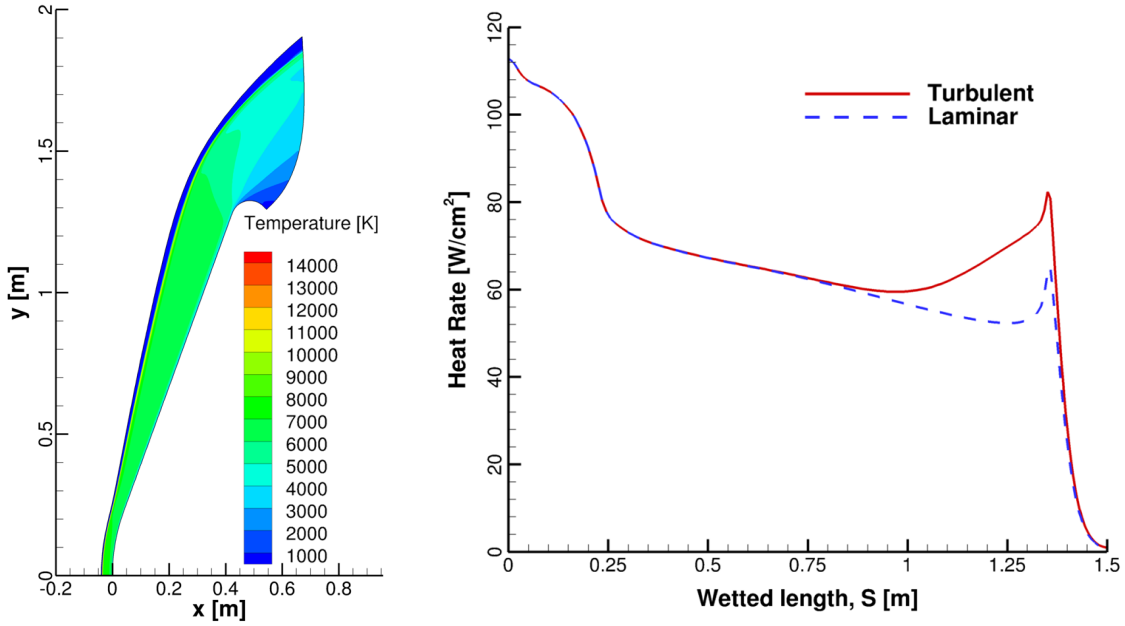

(a) Flowfield temperatures

(b) Surface heat flux

Figure 47: Pathfinder heat flux at peak heating (t = 65 sec).

cubic splines, and provided as inputs to the FIAT material response code at half second intervals. As noted in Ref. [5], it is difficult to reliably model convective cooling later in the vehicle's trajectory ($t > 100s$). While the overall heating is low, CFD simulations were performed after 100 s to provide an initial guess for the inverse analysis. For the current analysis, the recovery enthalpy (H_r) for FIAT is defined at each CFD point as the free-stream total enthalpy, as shown in Figure 48. Since the formation enthalpy of CO_2 at 0 K is negative (-8.93 MJ/kg), the freestream total enthalpy becomes negative as the vehicle slows down, and the velocity component of enthalpy decreases.

These heating boundary conditions are used with FIAT to calculate the in-depth material response at TC locations. An important advancement of this work compared to the previous Pathfinder data analysis done by Milos et al. is that an updated thermal response and ablation model is used for SLA-561V. This higher-fidelity model was developed by Laub et al. based on data taken from extensive testing conducted

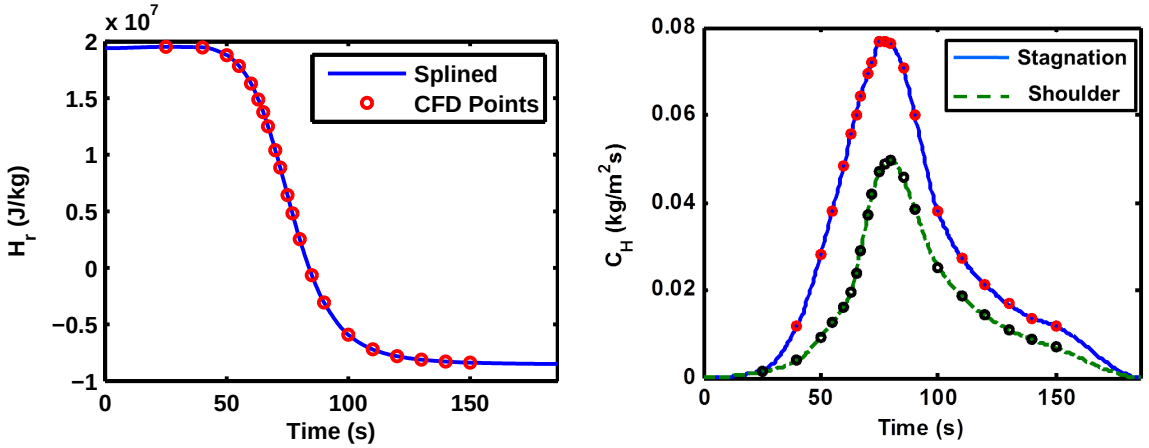

(a) Recovery enthalpy

(b) Heat transfer coefficient

Figure 48: Pathfinder nominal heating extracted from DPLR simulations.

in the NASA Ames IHF and AHF arc jet facilities during 2004-2005. [57] The updated model consists of two elements: a thermal response model to predict in-depth temperature response and a surface ablation model to predict surface temperature and surface recession.

The material stack up and thicknesses given in Ref. [5] for both nose and shoulder locations are used in this study. Most of the inside surface of the spacecraft structure was covered by a multilayer blanket insulation; therefore, the back face boundary condition is taken to be insulated with a heat transfer coefficient of zero. The flight data shows variations in initial temperature from one location to another; however, the temperature gradient across the TPS thickness at a given location is negligible. Therefore, the initial thermocouple measurement from the flight data is used as the initial temperature of the entire TPS block at each location. Reradiation is modeled to an environment with an effective temperature of 180 K (consistent with the reconstructed atmospheric temperature). A spherical geometry with radius equal to the nose radius is used for the nose location while a cylindrical geometry with radius equal to the corner radius is used for the shoulder location. A blowing correction parameter of 0.5 is used for the nose which is consistent with the laminar assumption.

The blowing parameter is switched to 0.3 for the shoulder to account for transition to turbulence.

Figure 49 shows the subsurface FIAT temperature predictions compared to the flight data for the nose and shoulder locations. For the nose, in the current analysis, the FIAT predictions exceed the flight data for the entire time span; while in the previous analysis by Milos et al., FIAT underpredicts the data up to about 100 s and then rises abruptly. This behavior is partly due to the fact that in the analysis by

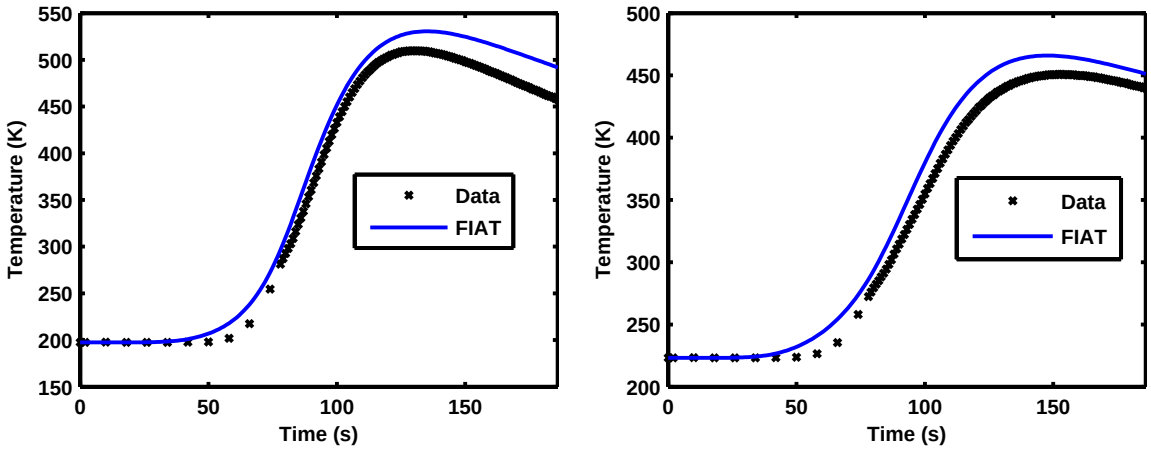

(a) Stagnation TC2 (b) Shoulder TC5

Figure 49: Pathfinder's subsurface temperature predictions compared to flight data.

Milos et. al. the heat transfer coefficient was extrapolated to zero at 20 s and 101 s while in this study they are spline interpolated to a small value at 0 s and 186 s. In the same figure, the subsurface FIAT temperature predictions can be seen compared to the flight data for the shoulder location. The same trends observed for the nose can be also seen for the shoulder location. However, at the shoulder, the previous analysis overpredicts the data more than the current analysis. It should be noted that there remains some uncertainty with the substructure aluminum honeycomb properties at the shoulder location. In addition, these results may be impacted by the validity of using 1-D conduction at shoulder. Overall the nose FIAT predictions are within 35 K of the flight data while the shoulder predictions are within 25 K of the data. The

RMS residuals for the nose and shoulder temperature response with respect to flight data are respectively 19.97 K and 15.33 K.

4.3.3 Inverse Analysis

The heat transfer coefficient, C_H, is discretized every 2.5 seconds and is estimated here at the stagnation and shoulder locations from the TC data. The flight data is available from 0 to 186 seconds; therefore, the estimation is performed for the same range of C_H profile. The plots in Figures 50 and 51 show the C_H estimation results for the nose location. The red and blue traces correspond to the nominal CFD-calculated heating conditions and the inversely estimated heating conditions. Figure 50 shows the C_H profile and the corresponding surface heat rate profile for both nominal and reconstructed environments. Figure 51(a) compares the nominal and estimated in-depth temperature predictions with the flight data at the nose TC location. Figure 51(b) shows the residual of in-depth temperature response at the nose with respect to the flight data for the nominal and reconstructed environments.

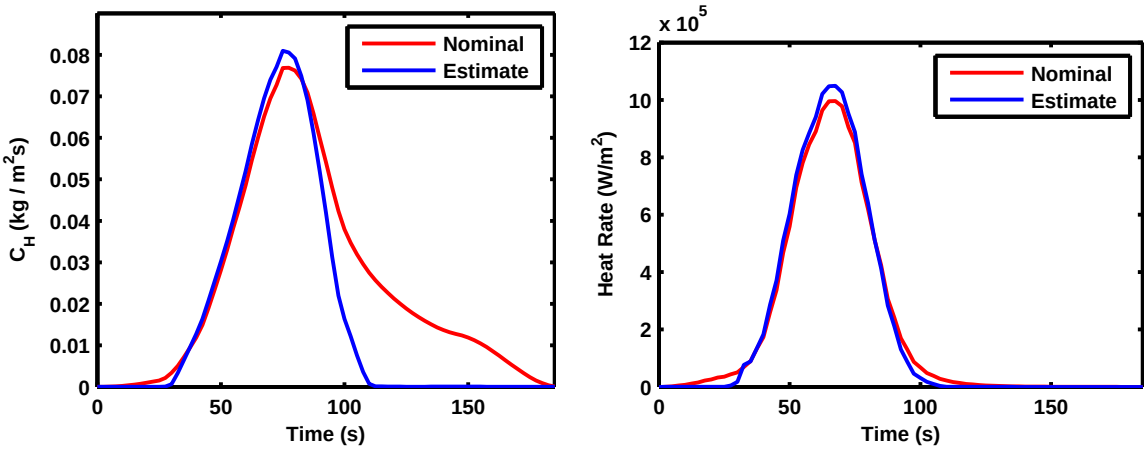

(a) C_H profile (b) Heat rate profile

Figure 50: Comparison of Pathfinder's stagnation nominal and inversely estimated heating environments at the nose.

Figure 51 shows that after the inverse estimation of C_H, FIAT predictions match

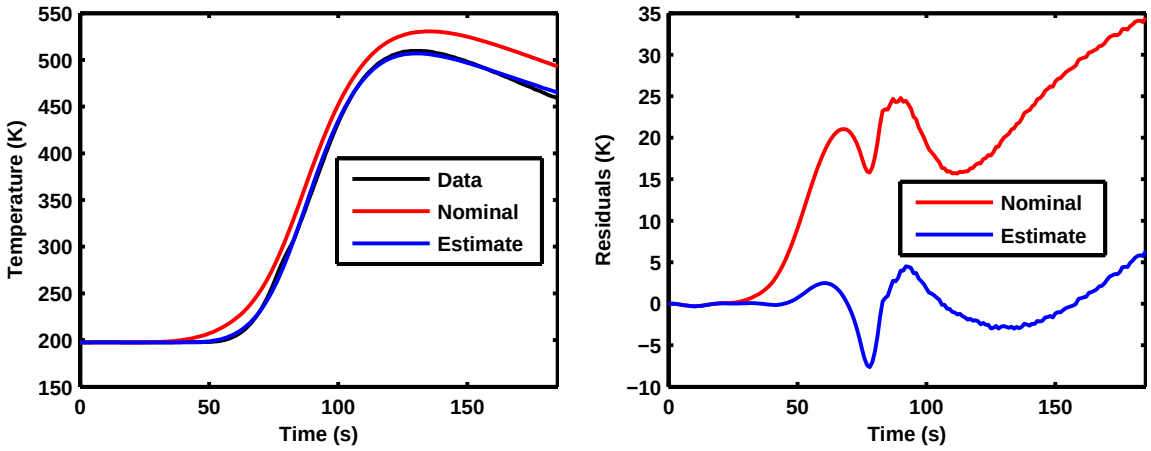

(a) TPS temperature at TC2 location

(b) Residual from flight data

Figure 51: Inversely estimated environments result in a much closer match between FIAT and TC2 flight data.

the data. The maximum difference is reduced to within 7 K of the flight data. The temperature response RMS residual with respect to flight data is reduced to 2.50 K from the previous 19.97 K. The objective function (sum of square of errors between FIAT temperatures and flight data) is reduced by almost two orders of magnitude. In Figure 50(a), it is evident that in order to achieve an agreement with the data, the estimator attempts to reduce C_H to small values in the pre-pulse and post-pulse regions of the C_H profile while slightly increasing it in the rising region of the heat pulse.

Figures 52 and 53 show the C_H estimation results for the shoulder location. Figure 53 shows that after the inverse estimation of C_H, FIAT predictions match the data. The maximum difference is reduced to within 5 K of the flight data from the previous 25 K. The temperature response RMS residual with respect to flight data is reduced to 2.20 K from the previous 15.33 K. The objective function is reduced by almost a factor of 40. Figure 52(a) shows that in order to match the data, the estimator reduced the pre-pulse C_H to small values and reduced the rising region of the pulse by about 5%. The decreasing regions of the pulse and the post-pulse C_H

region have not been changed significantly from CFD predictions. However, there is higher uncertainty at the shoulder due to uncertainty in the substructure material properties and limitations of 1-D conduction effects in this high-gradient region. It should be noted that the results achieved through inverse estimation for both shoulder and stagnation point ($\pm 5K$, $\pm 7K$) are better than matches between the new SLA-561V model and arc jet data it is based on, particularly in cool-down (see TC3 and TC4 in Ref. [57], Figures 23 and 24).

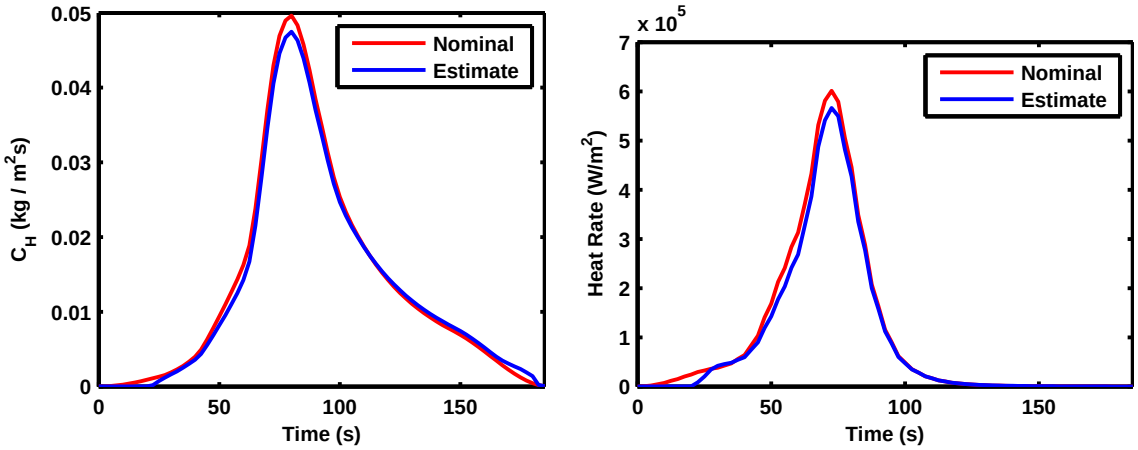

(a) C_H profile (b) Heat rate profile

Figure 52: Comparison of Pathfinder's shoulder nominal and inversely estimated heating environments.

In Figures 54 and 55, inversely estimated and nominal environments from this study are compared to digitized environments from Ref. [5] at the nose (TC2) and shoulder (TC5) locations. For the nose location, the nominal thermal response from new CFD simulations overpredicts the temperature, whereas both the inverse estimate and Ref. [5] environments result in a good match with the data. Visually, these C_H profiles appear similar, though there are other differences in these environments besides just C_H, such as the trajectory and the enthalpy profile. It is thought that some differences in the enthalpy profile are due to limitations in older versions of FIAT that constrained the recovery enthalpy to be positive. However, our conclusion

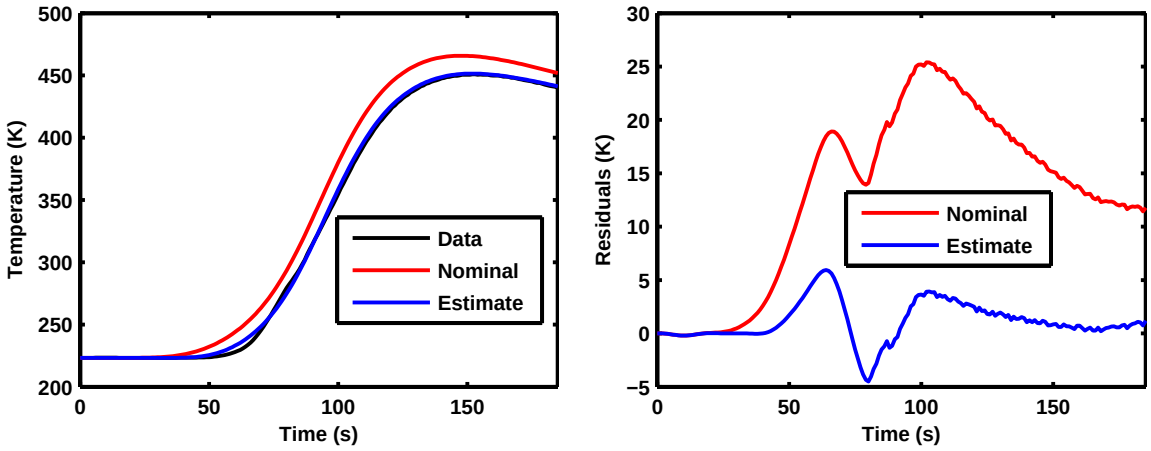

(a) TPS temperature at TC5 location (b) Residual from flight data

Figure 53: Inversely estimated environments result in a much closer match between FIAT and TC5 flight data.

is that the Milos et al. [5] environments, combined with the new SLA-561V material model match the TC2 data well without any scaling of the surface heat rate profile. Furthermore, the inversely estimated environment results in a better match with the data, particularly for the period between 50-75 seconds.

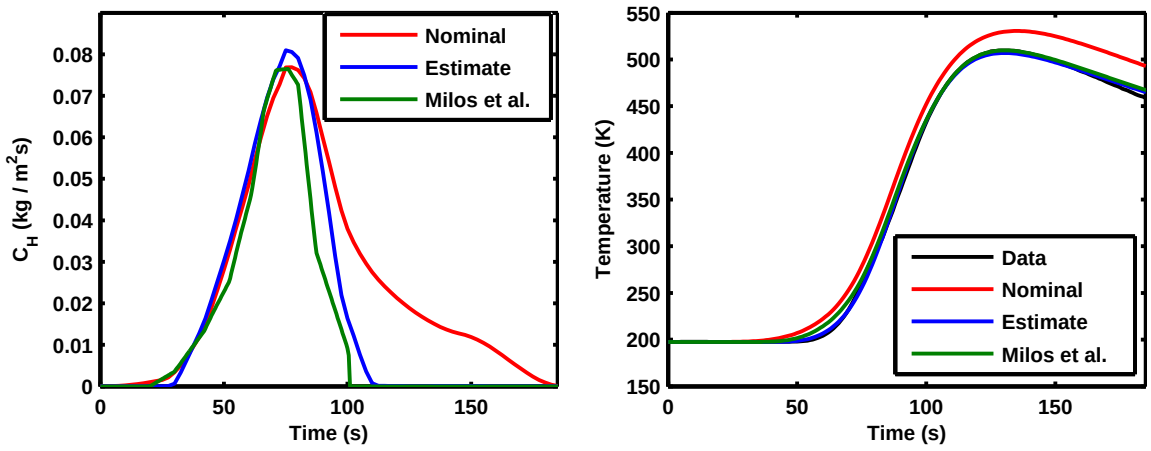

(a) C_H profile (b) TPS temperature at TC2 location

Figure 54: C_H estimation results for the nose location, including predictions from Milos et al.

At the shoulder location (Figure 55), it can be seen that the inversely estimated environments result in the best match with the data, with a reduction of pre-pulse

C_H, and peak reduction of around 5%.

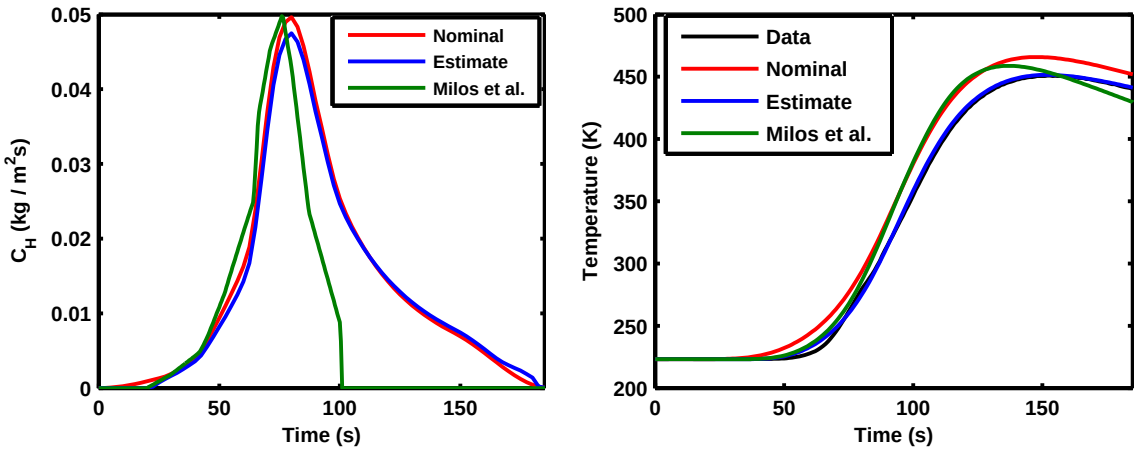

(a) C_H profile (b) TPS temperature at TC5 location

Figure 55: C_H estimation results for the shoulder location, including predictions from Milos et al.

4.3.4 Summary

The Mars Pathfinder aerothermal environment and heatshield material response were reconstructed using updated modeling tools and approaches. A newly computed reconstructed trajectory was used which is expected to be closer to the true trajectory. Updated CFD simulations were performed using DPLR for selected points along the reconstructed trajectory to characterize the vehicle's heating environment. The shoulder environments employed a turbulence model with transition. The heating boundary conditions were used with the thermal response code FIAT to calculate the forebody heatshield in-depth temperature response at the location of nose and shoulder mid-depth thermocouples. An updated thermal response and ablation model for the TPS material, SLA-561V, was used in this study. The direct FIAT predictions match the general trend of the flight data with a maximum difference of 35 K for the nose and 25 K for the shoulder locations.

In addition to this direct comparison, an inverse analysis was also completed. A Gauss-Newton minimization algorithm in conjunction with Tikhonov regularization

technique was employed to reconstruct the time-dependent unblown heat transfer coefficient. The estimator was able to reconstruct the C_H profile such that the corresponding temperature response was a good match with the flight data. The maximum difference was reduced to 7 K for the nose and 5 K for the shoulder. In order to achieve this close match for the nose location, the estimator reduced the pre-pulse and post-pulse C_H profile to small values while slightly increasing it in the rising region of the pulse. This demonstrates an advantage of inverse methods where the surface properties can be estimated as a function of time and are not limited by a simple uniform scaling. In order to match the TC data at the shoulder location, the estimator reduced the pre-pulse C_H to small values while maintaining the post-pulse C_H and slightly decreasing the peak value. This inverse solution at the shoulder is plausible. However, there is higher uncertainty here due to uncertainty in the substructure materials and the limitations of the 1-D conduction effects in this high-gradient region.

In general, the CFD models perform a good job of predicting the heating conditions in the high heat pulse region, but are not as accurate in the off-pulse regions. Furthermore, the starting and ending values used in spline interpolation for CFD should be revisited as they can result in an overestimation of the heating conditions in the off-pulse regions. It should be noted that in the previous analysis by Milos et al. this interpolation was not done and the heat transfer coefficient was set to zero in the beginning and end regions of the trajectory. Considering this, it can be concluded that the updated SLA ablation and thermal response model combined with the inverse solution techniques result in improved agreement with the Mars Pathfinder flight data.

Iterative coupling between CFD and current material response codes may improve the match between CFD predictions and inverse reconstructed environments. Also, blowing of ablation products could be included in the DPLR simulations, though this would substantially increase the complexity and computational cost of the inverse

analysis process. Inverse analysis revealed a strong dependence of the reconstructed shoulder environment to substructure properties. In addition to material uncertainties, 1-D conduction modeling may not be sufficient for the shoulder region where there is both high curvature and strong heat rate gradients along the surface. An inverse analysis process coupled with a 2-D material response code could increase confidence in the shoulder results, though with an associated increase in computational cost.

CHAPTER V

APPLICATION TO MSL HEATSHIELD FLIGHT DATASET

5.1 Introduction

The Mars Science Laboratory successfully landed the Curiosity rover on the Martian surface on August 6, 2012. The MSL aeroshell was a 4.5-meter diameter spherically-blunted 70-degree half-angle cone with a PICA forebody heatshield. As mentioned in Chapter 1, the MSL heatshield was instrumented with a comprehensive set of pressure and temperature sensors called MEDLI. The aeroheating subsystem, MISP PICA plugs, provided subsurface temperature measurements of the TPS material at four depths and at 7 locations on the heatshield. Refer to Chapter 1 for a more detailed explanation of MISP instruments and their locations.

In this chapter, the tools and methodologies developed in Chapter 2 will be applied to the MSL heatshield flight data. First, the flight data are presented followed by a discussion of turbulent transition observed directly from the data. A direct analysis is performed where FIAT temperature predictions based on nominal CFD heating environments are compared with the flight data. Next, the surface heating function estimation framework is employed to reconstruct MSL's time-dependent surface heating at plug locations from the shallowest thermocouple flight data. The sensitivity of the estimated surface heating profile to estimation tuning parameters, measurement errors, recession uncertainty and material property uncertainty is investigated. A Monte Carlo analysis is conducted to quantify the uncertainty bounds associated with the nominal estimated surface heating. Next, the TC driver approach is employed to apply the multi-parameter estimation framework to conduct PICA material

property estimation from the deeper thermocouple data.

In the final section of this chapter, the margin methodology that was used in the MSL heatshield design is reviewed. A discussion of how findings from MSL flight data may improve the margin process for future missions follows.

5.2 Heatshield Flight Data

The MEDLI data were recorded and stored successfully during the atmospheric entry. A limited part of the data was transmitted in real-time and the full dataset was received from the rover within a week after landing. The thermocouples behaved as expected and the data contained a low amount of noise. The HEAT sensor did not behave as expected and the recorded transient data were very noisy. [144, 145] For this reason, the analysis of HEAT data is not pursued in this work. Figure 56 shows the MISP thermocouple flight data at all 7 plug locations. Time zero is the entry interface time based on a spacecraft time (SCLK) of 397501714.953125 seconds. Thermocouple temperatures at this time ranged from 170 to 203 K depending on TC depth and plug location.

Peak temperatures for the shallowest thermocouple (TC1) ranged from 1094 K at plug 4 to 1322 K at plug 7. Note that having the highest temperature does not necessarily mean that plug 7 experienced the highest heating as there is some variation in TC1 depth across different plugs (see Table 1 from Chapter 1 for X-ray measured thermocouple depths). Peak temperatures for the deepest thermocouple (TC4) ranged from 393 K at plug 4 to 402 K at plug 2. However, it should be noted that TC3 and TC4 were not wired at plugs 5 and 7 due to data channel limitations. Figure 57a shows TC1 temperature plotted as a function of time for all the plug locations. Examination of the TC1 temperature profile across different plugs provides insight regarding the aeroheating environment distribution along the surface of the heatshield. It can be seen that up to 65 seconds, plug 5 has the highest temperature

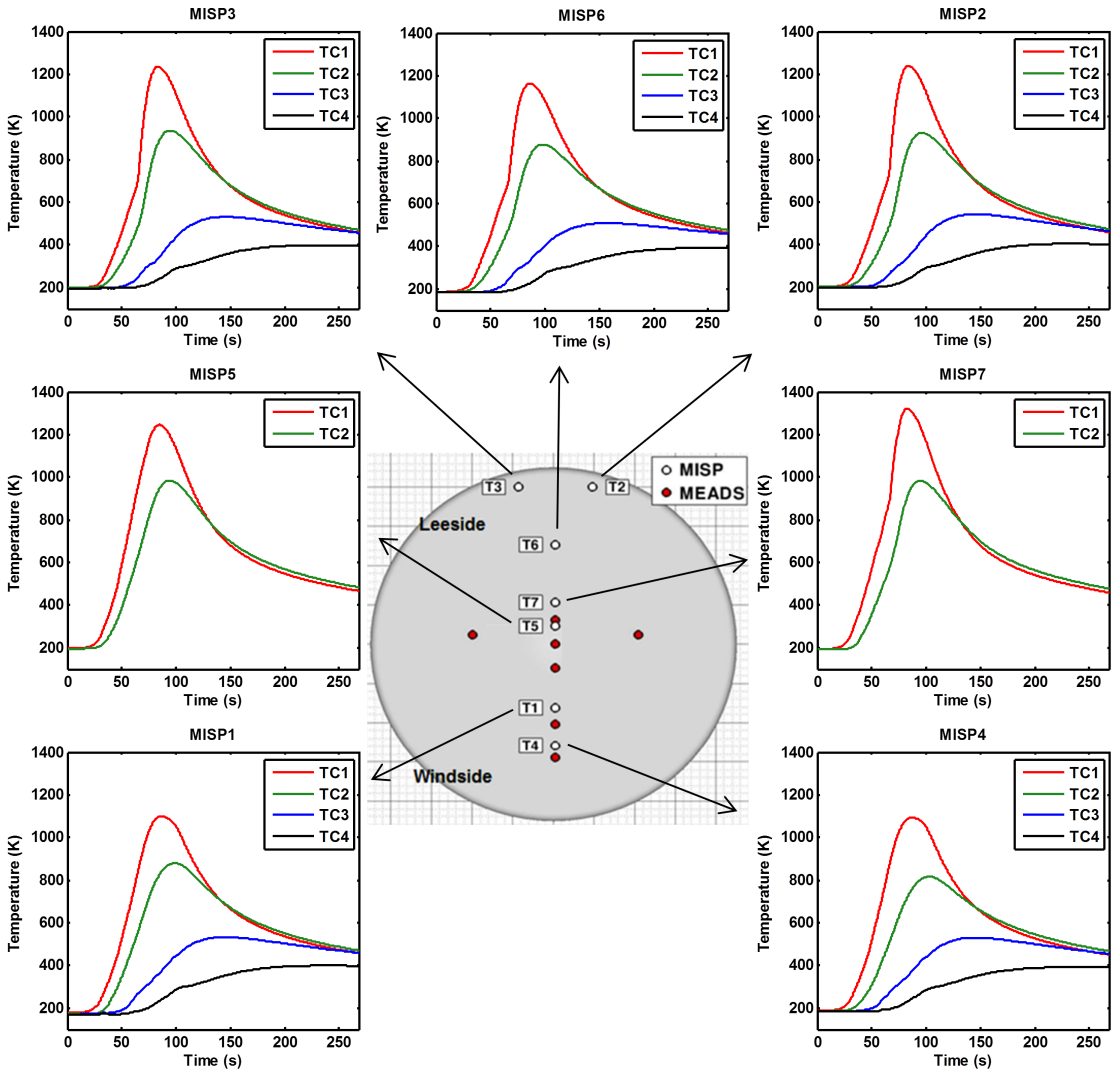

Figure 56: The MISP flight thermocouple data at different locations and depths on the heatshield.

followed closely by plugs 7, 1 and 4, while plugs 2, 3 and 6 are at lower temperatures. This trend matches the surface heating distribution expected for laminar flow. After this time, transition to turbulence for plugs 2, 3, 6, and 7 can be clearly observed from the sudden slope change in the temperature data (seen also in Figure 57b). A later transition at plug 5 can also be seen. Transition causes the TC1 temperature at these plugs to rise rapidly and eventually reach higher peak values. Specifically, since plug 7 was already at a high level of laminar heating, its temperature increased

to be the highest peak after transition.

Figure 57b illustrates the TC1 temperature rise rate as a function of time for these plugs. Sharp increases can be observed in the temperature rise rates during the 63-66 s time period. Plug 3 becomes turbulent around 64 seconds, followed by plug 2 at 65 seconds, and plugs 6 and 7 at 66 seconds, and plug 5 later at 74 s. It should be noted that these transition times are based on the slope changes observed in the subsurface thermocouple data. In-depth temperature response lags somewhat behind any changes in the surface heating; therefore, the actual surface turbulent transition times are likely 1-2 seconds earlier than the numbers reported here. In the inverse analysis section, a better estimate of transition time is provided based on surface heating reconstruction results. The transition front moved quickly from plugs 2 and 3 at the shoulder to plugs 6 and 7. Pre-flight predictions indicated transitions times of 52, 57, and 70 seconds for plugs 2 (3), 6, and 7 respectively. These predictions are based on a smooth wall momentum thickness Reynolds number threshold of 200. It is currently believed that the observed quick motion of the transition front is due to roughness-induced transition. See Refs. [145, 146] for more information on this topic.

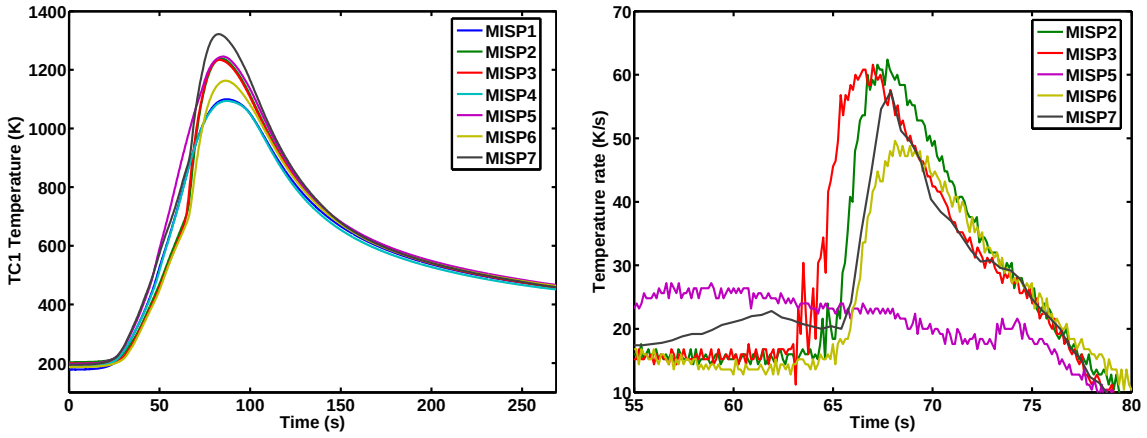

(a) TC1 Temperature

(b) TC1 Temperature Rise Rate

Figure 57: Transition to turbulence can be seen from TC1 data for plugs 2, 3, 5, 6 and 7.

In Figure 58, it can be seen that there is an unexpected slope change ("hump") in the temperature profile for the deeper thermocouples (TC3-4) at plug 2. The hump happens in the 200-400 K temperature range. This trend is observed consistently for all plug locations. Similar behavior has also been seen in the MISP qualification arc jet dataset, arc jet testing for some other materials, and also for Mars Pathfinder bondline thermocouples flight data. This phenomenon is not well understood at present and current analysis tools are not able to model this behavior. Therefore, a match between the data and model predictions should not be expected for this part of the data.

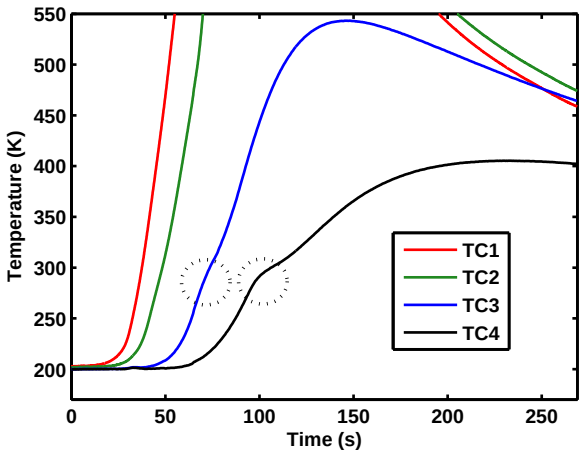

Figure 58: The "hump" observed in TC3 and TC4 flight temperature data.

5.3 Direct Analysis

The purpose of the direct analysis is to compare the FIAT temperature predictions based on the nominal heating environments with the flight temperature data. In order to predict the vehicle's aeroheating environment, CFD simulations are performed using the DPLR code along the Best Estimated Trajectory (BET) incorporating MEADS and Inertial Measurement Unit (IMU) flight data. [147] These CFD solutions were generated by Todd White from NASA Ames Research Center. Refs. [148, 145] provide more details on the models and assumptions used in CFD simulations. The

Mitcheltree and Gnoffo model [41] is used for surface catalytic reactions while the wall is assumed to be at radiative equilibrium. Turbulent flow is simulated with the Baldwin-Lomax algebraic model. [27] Turbulent transition is modeled based on a smooth wall momentum thickness Reynolds number, Re_θ, threshold of 200. Surface heating for the periods before 25 seconds and after 115 seconds is set to zero. Radiative heating is assumed to be zero for this analysis, consistent with assumptions made during design.

As discussed in Chapter 1, surface heat rate is not a direct input to FIAT for ablative materials. Surface boundary conditions such as pressure, heat transfer coefficient and recovery enthalpy are extracted from the CFD solutions at each plug location. These quantities are then fit in time with tight monotonic cubic splines, and provided to the FIAT material response code. The surface energy balance equation (Eq. (18) from Chapter 2) is solved in FIAT using the PICA equilibrium chemistry model. Reradiation is modeled with an effective temperature of 180 K. A manual grid is employed to specify the initial temperature distribution of the PICA block according to the flight data initial temperatures. The blowing reduction parameter is assumed to be 0.5 for laminar flow and 0.3 for turbulent flow. PICA material model version 3.3 is used in this analysis.

In the following plots, FIAT temperature predictions at all plugs are shown against the flight data. It should be noted that while the temperature predictions are shown at all TC depths for the sake of completeness, the focus will be mainly on how the top thermocouple results compare as it is the closest to the surface and most sensitive to surface heating.

Figure 59 shows the FIAT temperature predictions compared with flight data at plugs 1 and 4. These plugs are on the heatshield windside and close to the stagnation point. It is evident that the analytical models underpredict the flight data peak temperature. Possible causes for this difference could be radiative heating or low

levels of flow turbulence due to pyrolysis gas injection. Additionally, arc jet tests have shown that molten Silica from the RTV bonding used around the plugs can flow on the surface of a plug and result in lower emissivity, and therefore lower reradiation.

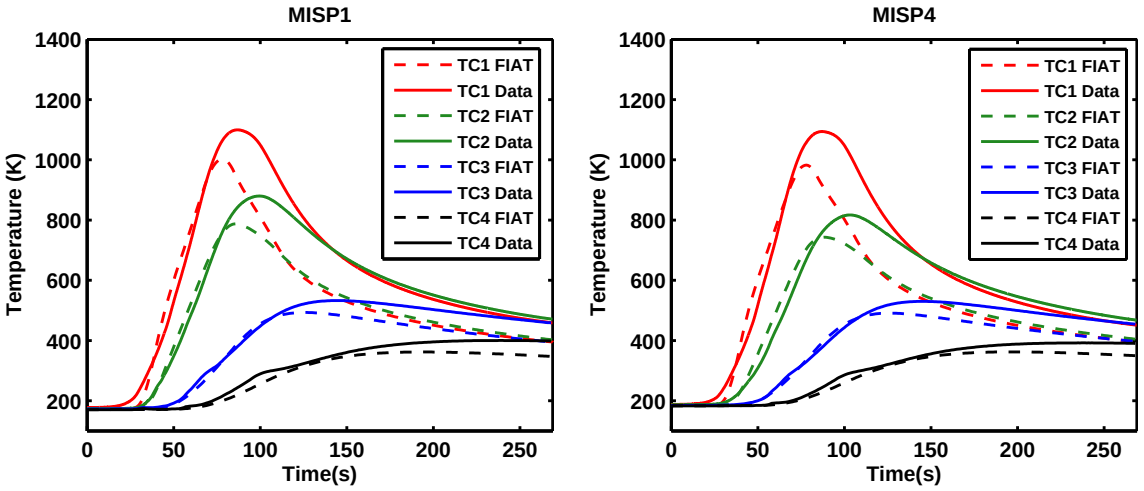

Figure 59: FIAT predictions compared with flight data for plugs 1 and 4.

Figure 60 shows the comparison with flight data for plugs 2 and 3. These plugs are close to the leeside shoulder. Being farthest from stagnation point, they were expected to see the highest heating augmentations due to turbulent transition. It is evident that model predictions significantly overpredict peak temperature and temperature rise for these plugs. This is due to the fact that transition to turbulence happened later than expected and for that reason the surface heating did not have as much time to increase. Therefore, the turbulent temperature augmentation at these locations was less than model predictions. FIAT predictions also show that TC1 was expected to burn out because of recession. This did not occur in flight because of the lower than expected heating levels and also possibly because the equilibrium models used in FIAT for gas/surface interactions are known to overpredict recession at the range of heat rates experienced by the MSL vehicle. [83] The only information that can be obtained from flight data regarding recession is that it was less than TC1 depth ($\simeq$

0.1 inch) for all plugs.

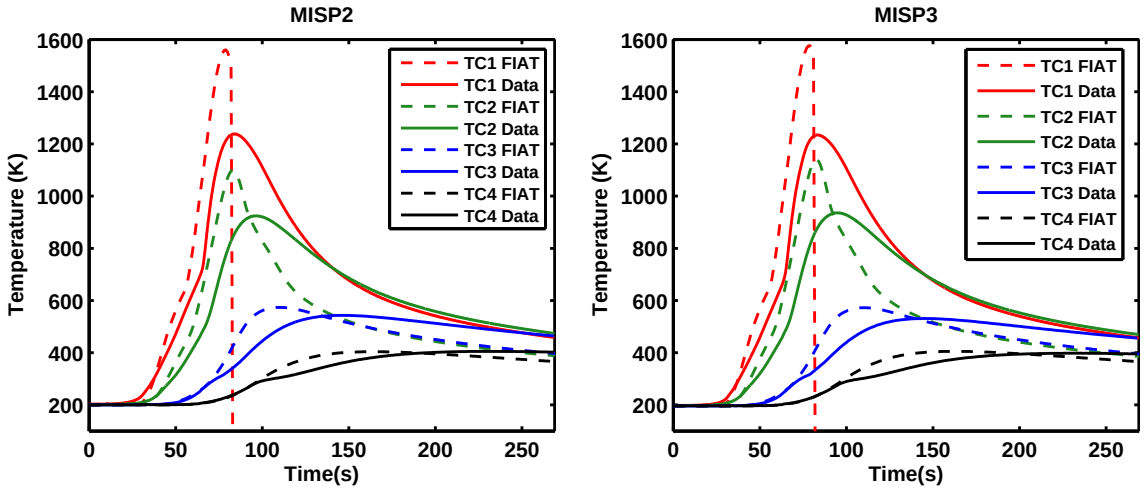

Figure 60: FIAT predictions compared with flight data for plugs 2 and 3.

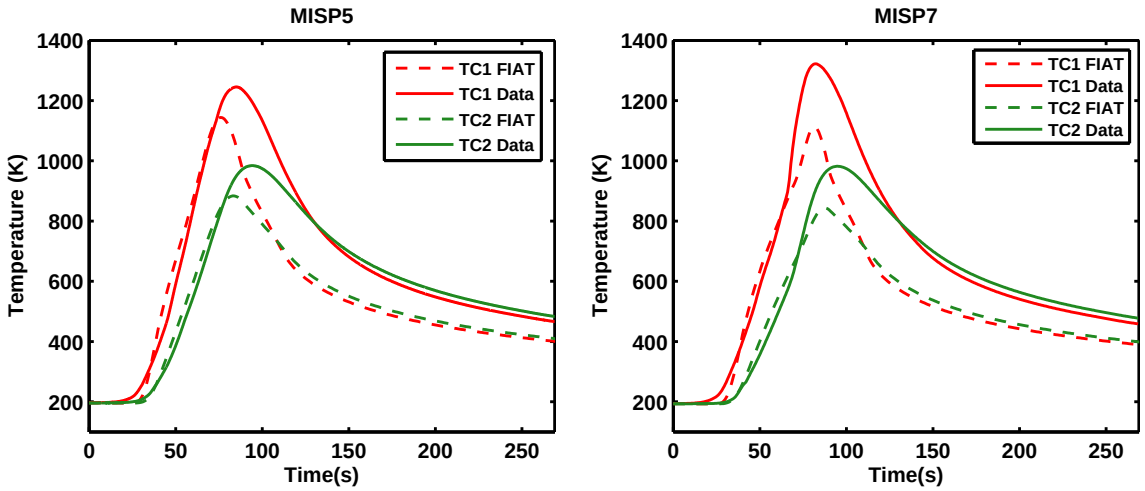

Figure 61: FIAT predictions compared with flight data for plugs 5 and 7.

Model predictions and flight data are compared in Figure 61 for plugs 5 and 7. These plugs are close to the heatshield apex. Similar observations as for plugs 1 and 4 can be made for plug 5. Laminar heating is underpredicted, possibly because of the lower reradiation due to lower surface emissivity caused by Silica flow. Plug 7 experienced higher than expected heating because of earlier transition to turbulence as compared with CFD predictions. In CFD environments, transition happens quite

late in the trajectory for plug 7; therefore, heating does not rise to very high levels.

Figure 62 shows the comparison between flight data and FIAT predictions for plug 6. Similar observations as for plugs 2 and 3 can be made. Based on CFD environments, transition to turbulence was expected to happen earlier in the trajectory (58 seconds). However, since flight transition happened later, the temperature augmentation was not as much as the model predictions.

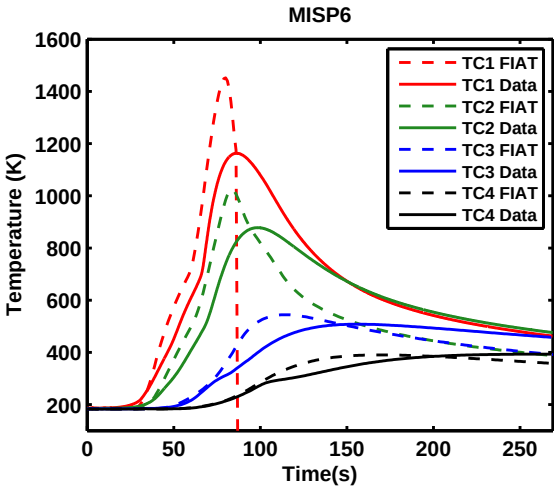

Figure 62: FIAT predictions compared with flight data for plug 6.

One important observation that was made in the comparisons between the data and model predictions for all plugs was that the temperature pulse in the data was wider than model predictions. In other words, analytical models predict TC1 to cool down at a faster rate than flight. There are two possible reasons for this observation. First, the PICA equilibrium chemistry model in Martian atmosphere is known to be inaccurate for MSL heating conditions which results in an overprediction of wall enthalpy leading to lower heating. Second, even though radiative heating was assumed to be zero in this analysis, recent simulations have shown that MSL radiative heating is non-negligible. Radiative heating peaks after the convective heating which will contribute to widening the overall heat pulse and therefore the in-depth temperature pulse.

5.4 Aerothermal Reconstruction

In this section, the surface heating function estimation framework is used to reconstruct MSL's surface heating at MISP plug locations from the flight temperature data. The shallowest thermocouple data (TC1) is utilized for the purpose of surface heating estimation as it is the most sensitive to surface heating and least affected by subsurface material property uncertainty. Heating estimation is performed every 1 second (1 Hz) using flight data at a frequency of 2 Hz. The effect of the estimation and data frequency on the results is also investigated. The estimation is performed by minimizing an objective function containing the sum of squared of errors between FIAT temperature predictions and flight data. The Gauss-Newton minimization method in conjunction with Tikhonov first-order regularization technique are used for estimation. Please refer to Chapter 2 for a more detailed description of the framework and inverse methods used here.

As mentioned earlier, surface heat rate is not a direct input to FIAT for ablative materials. Two distinct approaches are used for this analysis. The first approach reconstructs the surface heating by estimating heat transfer coefficient at an ablating surface with surface recession. Due to the limitations of this approach for MSL heating conditions, a second approach is also employed which directly estimates surface heating of a non-receding surface with no ablation.

5.4.1 Heat Transfer Coefficient Estimation of an Ablating Surface

This approach was used for the inverse analysis of simulated MISP data and Mars Pathfinder data discussed in Chapter 4. Inverse methods are employed to estimate heat transfer coefficient, C_H, as a function of time while keeping recovery enthalpy, H_r, fixed to the CFD-calculated value and allowing FIAT to internally calculate surface ablation chemistry and material decomposition (see Eq. (28)). Once the heat transfer coefficient profile is estimated, the surface heating is reported as the sum of

the first four terms in Eq. (28), which is equal to convection and chemical heating contributions.

$$\begin{aligned} C_H(H_r - h_w) + \dot{m}_g h_g + \dot{m}_c h_c - (\dot{m}_c + \dot{m}_g)\, h_w \\ +\alpha_w q_{rad} - \sigma \epsilon_w (T_w^4 - T_\infty^4) - q_{cond} = 0 \end{aligned} \tag{28}$$

Figure 63 shows the estimated surface heating profiles at all MISP locations using the heat transfer coefficient approach. Both unregularized and regularized solutions are shown. The unregularized solution results in a better match with the in-depth temperature data. This will be illustrated later when the effect of regularization parameter on estimation results is investigated (Figure 67b). However, it is evident that regularization reduces the oscillations and provides a more physically realistic heat rate profile. Comparison of the heat rate profiles for different plugs leads to the

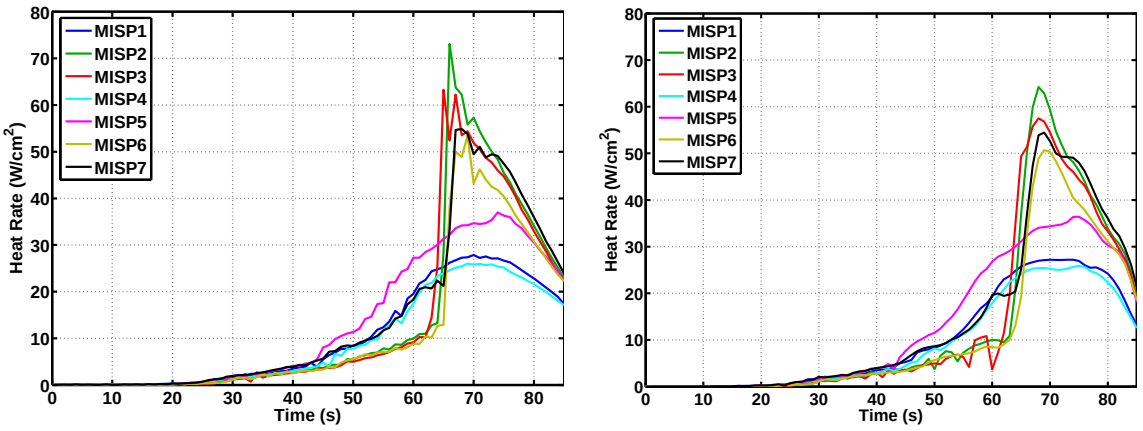

(a) Without Regularization (b) With Regularization

Figure 63: Reconstructed surface heat rate profiles at MISP locations using the C_H estimation approach.

observation that MISP5 has the highest heating up to about 65 seconds followed by plugs 1, 4 and 7, while the plugs close to the shoulder (2, 3, and 6) remain at a low level of heating. This trend matches the laminar heating predictions by CFD tools at the apex region (plugs 5 and 7) and stagnation region (plug 1 and 4) which were

expected to experience the highest laminar heating. However, the onset of Boundary Layer Transition (BLT) can be observed around the 63-65 second period for plugs 3, 2, 6 and 7. BLT results in much higher turbulent heating levels for these plugs. Plugs 2, 3 and 6 match the trends predicted by CFD tools; however, plug 7 significantly exceeds CFD predictions. This can be attributed to heating augmentation due to surface roughness or shock-layer radiation. The small spike in plug 5's surface heating around 74 seconds may also be BLT. Similar to plug 7, surface heating at plug 5 also exceeded the CFD predictions. Plugs 1 and 4 remained laminar throughout the trajectory, but slightly exceeded the CFD predictions. Preliminary analysis shows that the observed difference can be partially explained by radiative heating in the stagnation region, although more work is needed. [146]

Some limitations and uncertainties exist in the heat transfer coefficient approach for MSL heating conditions. This approach relies on equilibrium models for the calculation of surface chemistry terms. As long as the material ablation model is accurate, the heat transfer coefficient estimation is reliable. However, the equilibrium chemistry model employed in FIAT for PICA is known to be inaccurate at the low heating conditions experienced by MSL ($< 100\ W/cm^2$) and it tends to overpredict the recession. [83] As a matter of fact, the model's recession prediction for the nominal MSL heating environment exceeds TC1 depth. This is clearly not accurate because flight data demonstrates that recession was less than 0.10 inch (as the shallow thermocouple survived at all plugs).

Figure 64 compares the nominal CFD-calculated recovery enthalpy and FIAT-calculated wall enthalpy profiles at plugs 1 and 2. This wall enthalpy is calculated by FIAT's PICA equilibrium model and does not match the CFD-calculated wall enthalpy. It can be observed that the two enthalpy profiles approach one another around 80-85 seconds. This leads to convective heat rate (first term in Eq. (28)) approaching zero which results in the loss of in-depth temperature sensitivity to C_H.

For this reason, in the heat transfer coefficient approach, estimation is ceased around 85 seconds as a close match between the FIAT temperature predictions and TC1 flight data can not be achieved through C_H iteration after this time.

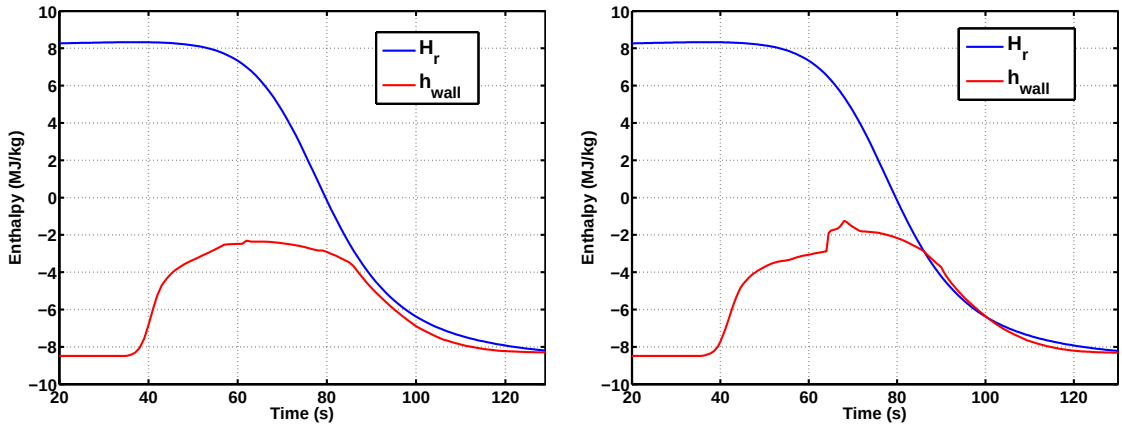

(a) Plug 1 (b) Plug 2

Figure 64: Recovery enthalpy and FIAT wall enthalpy compared at plugs 1 and 2.

5.4.2 Heat Rate Estimation of a Non-Receding Surface

No validated finite-rate models exist for PICA gas-surface chemistry in the Martian atmosphere. Consequently, the observed lack of substantial recession in flight and the known overprediction by FIAT equilibrium chemistry models motivate the application of another bounding approach where surface heating is estimated without recession. Recession can not simply be turned off in Eq. (28) without regenerating the chemistry solutions; therefore, C_H estimation is not possible for this approach. An alternative surface energy balance option is implemented in FIAT (called "option 3") which can be reformulated into the following equation:

$$q_s + \alpha_w q_{rad} - \sigma \epsilon_w (T_w^4 - T_\infty^4) - q_{cond} = 0 \tag{29}$$

The first term in this equation is analogous to the sum of the first four terms in Eq. (28) (reported as the surface heat rate in the previous section) which includes the convective heat flux and chemical heating contributions. This approach allows

suppression of surface recession, thus estimating a non-receding surface heat rate using the inverse methods described earlier. Being independent of FIAT surface chemistry models, this approach enables more accurate estimation of the surface heating profile for the entire time period. The estimation is not limited to 0-85 seconds as it was with the C_H approach. Figure 65 shows the unregularized and regularized surface heating estimates at all MISP plug locations. The estimation was performed in the same manner as previous section by using the Gauss-Newton method in conjunction with Tikhonov regularization technique. Only TC1 data were used.

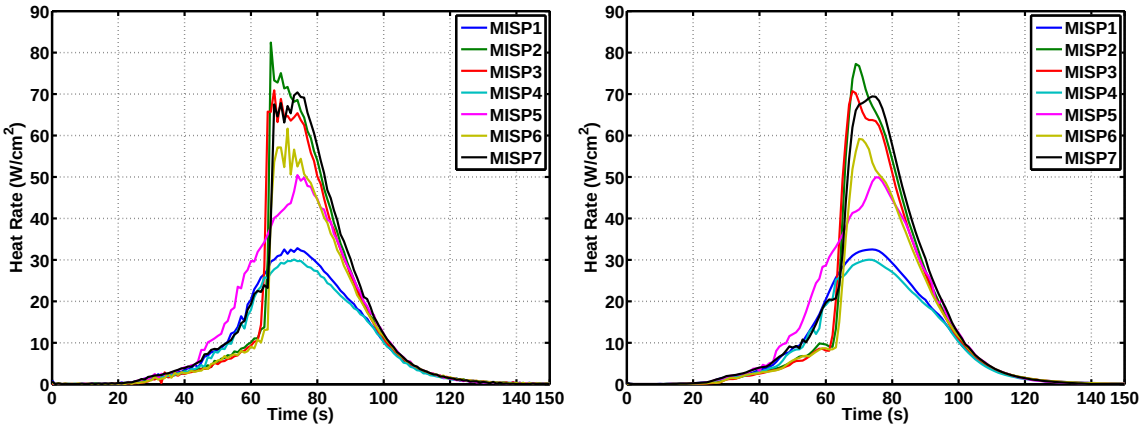

(a) Without Regularization (b) With Regularization

Figure 65: Estimated non-receding surface heat rate profiles at MISP locations.

The same laminar and turbulent heating trends observed in the first approach (Fig. 63) can be seen here. In general, the estimated surface heating is higher for this approach. In the absence of recession, the surface is farther away from TC1 and consequently higher incoming heating is required to achieve the same in-depth temperature. This figure also shows that the regularized solutions provide smoother and more physically realistic heating profiles than the unregularized solutions. Nonetheless, the unregularized solutions match the data more accurately. Some uncertainties are associated with these estimates due to numerical issues, measurement errors, recession uncertainty and material property variations. The next sections examine the

effect of these uncertainties on the estimated non-receding surface heat rate profile mainly at plug 2 (highest heating case). Similar results are expected at other locations.

5.4.2.1 Numerical Sensitivity

A numerical sensitivity study shows that the estimated heat rate profiles are stable and robust to numerical parameters. Four parameters are examined: regularization order, regularization parameter, data frequency and heat rate estimation frequency. Figure 66 shows the effect of regularization order. As mentioned before, regularization has a smoothing effect on the estimated heating profile. Minor differences can be observed in the peak region (67-74 seconds) in Fig. 66a. Lower order of regularization results in higher level of damping. In Fig. 66b, it can be seen that the match between the data and FIAT predictions is similar for all three cases. First-order regularization is typically used in literature for surface heating estimation problems and is applied in this analysis.

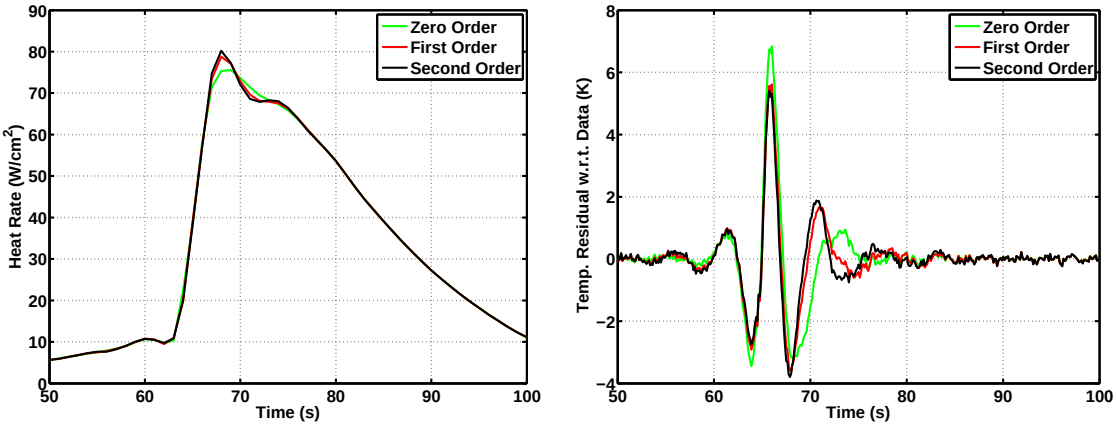

(a) Estimated heat rate profile (b) FIAT TC1 temperature residual w.r.t. data

Figure 66: Effect of regularization order on surface heating estimation results.

The plots in Fig. 67 show the effect of the regularization parameter, which is a scaling factor that controls the level of smoothing. Estimation without regularization results in a good match between FIAT TC1 temperature predictions and the flight

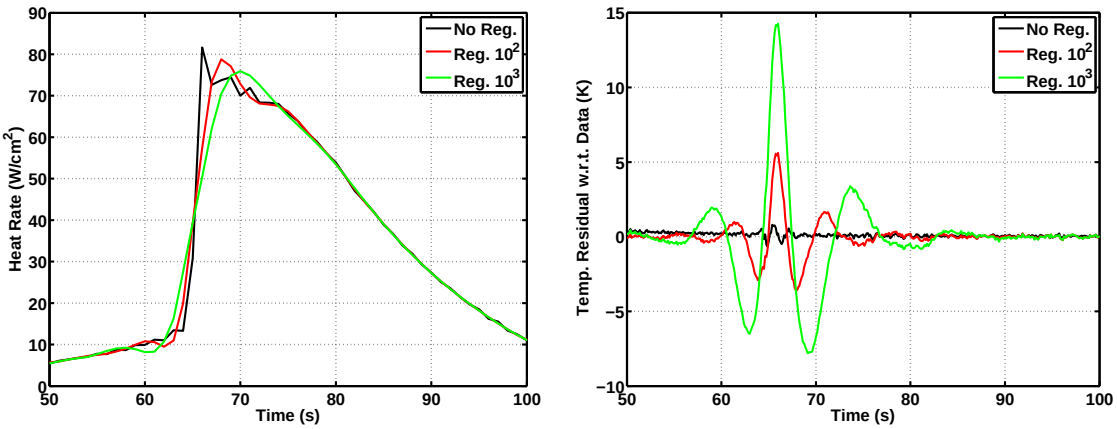

(a) Estimated heat rate profile (b) FIAT TC1 temperature residual w.r.t. data

Figure 67: Effect of regularization parameter on surface heating estimation results.

TC1 data. The difference is within 1 K as shown in Fig. 67b. However, Fig. 67a shows that the reconstructed heat rate profile includes oscillations around the peak heating time. As the regularization parameter is increased, the oscillations are reduced and the estimated heat rate profile takes a shape which is more similar to CFD-generated profiles. It is evident that regularization dissipates the sharp rise due to turbulent transition and that a higher parameter value results in a worse match between FIAT temperature predictions and TC data (Fig. 67b). Consequently, a baseline regularization parameter of 10^2 was selected in this work as a balance between smoothing and data matching.

For most plugs, the TC1 temperature data are available at 8 Hz. However, selection of the data frequency used in the inverse analysis should be approached carefully. Using the original 8 Hz data in the estimation would require significant computer time as FIAT simulations would have to be performed and saved at a high rate. A lower data frequency is desirable because it lowers the computational cost in addition to providing an inherent smoothing of the data through interpolation. However, one needs to ensure that the estimation problem remains over-determined, meaning that there should be more measurement points than estimation parameters. Figure 68a

illustrates the effect of data frequency on estimated surface heating profile. Data frequency does not have a significant effect on the surface heating estimation results. However, a mild smoothing effect is evident as the data frequency is reduced. This is related to the inherent smoothing of the data that occurs when the original data are interpolated at a lower frequency.

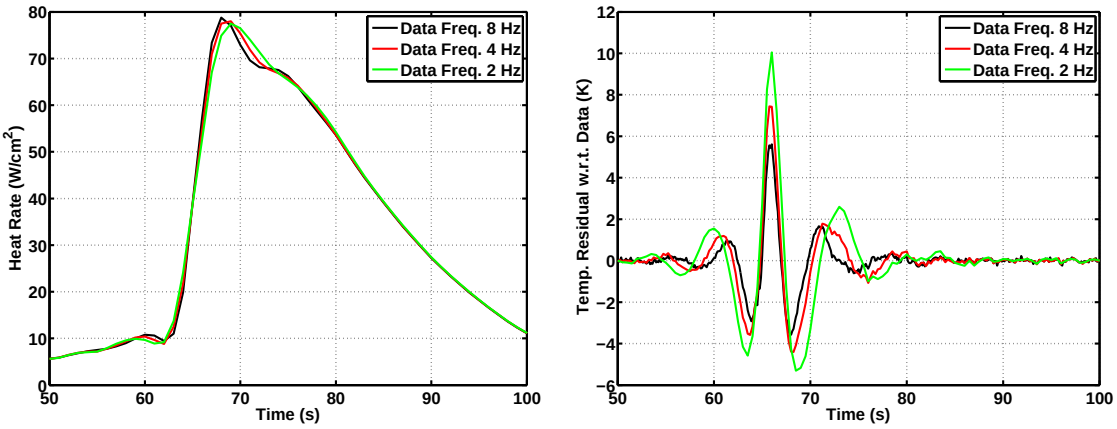

(a) Estimated heat rate profile (b) FIAT TC1 temperature residual w.r.t. data

Figure 68: Effect of data frequency on surface heating estimation results.

Figure 69 shows the effect of estimation frequency. Higher estimation frequency results in the reconstruction of surface heating at a higher time resolution; however, it requires more computational resources. For higher estimation frequency, turbulent transition is captured only slightly more accurately than for the lower estimation frequency case. The temperature residual with respect to flight data is smaller; however, the overall effect is still minimal.

This numerical sensitivity analysis showed that the estimated heat rate profiles are robust with respect to numerical parameters. Therefore, the rest of the analysis in this work use the first order regularization with a parameter of 10^2, data frequency of 2 Hz and estimation frequency of 1 Hz. This will allow obtaining numerically accurate smooth solutions at reasonable computational cost.

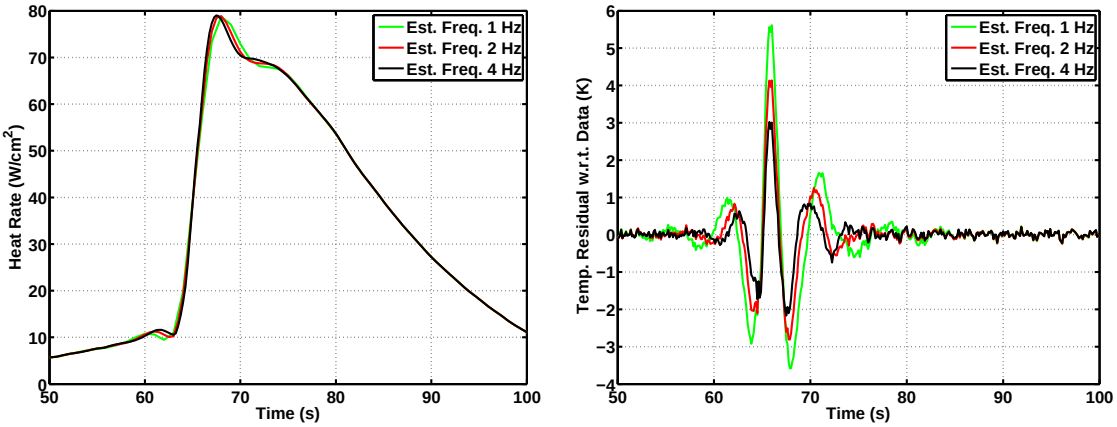

(a) Estimated heat rate profile (b) FIAT TC1 temperature residual w.r.t. data

Figure 69: Effect of estimation frequency on surface heating estimation results.

5.4.2.2 Measurement Error Sensitivity

Two types of possible measurement errors are examined here: TC depth uncertainty and thermal lag. Accurate flight heatshield TC depths using X-ray measurement are available; however, this measurement technique can have a $\pm 2\sigma$ uncertainty of ± 0.003 inch. Figure 70a shows the effect of this uncertainty on the estimated heating profile at plug 2. The deviation resulting from this uncertainty is bounded by $\pm 4\ W/cm^2$ at the peak.

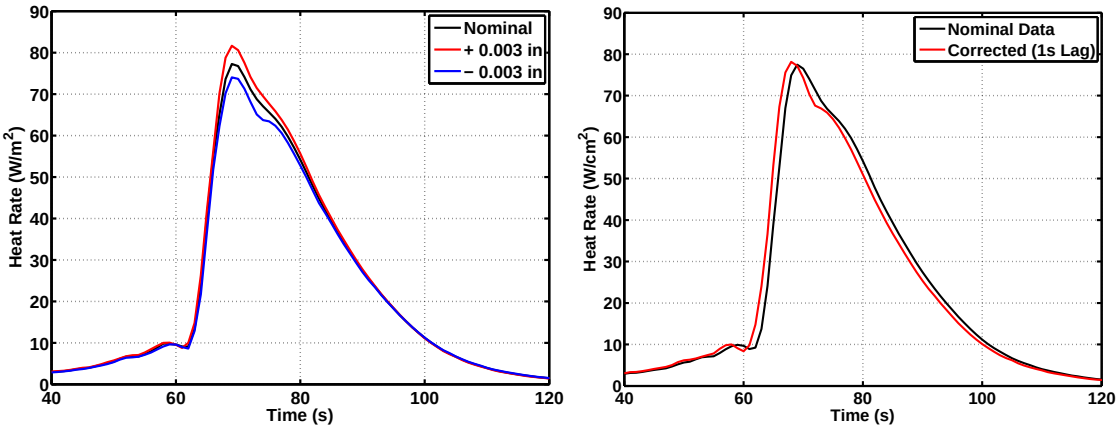

(a) TC depth uncertainty (b) 1-second lag correction

Figure 70: Effect of measurement errors on surface heating estimation results.

Additionally, the TC temperature readings may contain a thermal lag bias error. Thermal lag is caused by the thermal mass of the thermocouple and is defined as the difference between the material temperature and the thermocouple reading. Figure 70b shows the surface heating profile estimated from temperature data corrected for a constant 1-second lag (partially based on ground testing of MISP instrumentation). It is clear that the thermal lag correction results in a 1-second shift in the estimated heating profile.

5.4.2.3 Recession Sensitivity

The heat rate estimation approach used in this section assumes zero surface recession because the nominal PICA ablation model significantly overpredicts recession for MSL conditions. The only information obtained from flight data regarding recession is that it was less than 0.10 inch (TC1 depth) as the shallowest thermocouples did not burn out. Therefore, it is desirable to examine the effect of surface recession on the estimated heating profile.

Once the non-receding surface heat rate profile is estimated at plug 2, the complete in-depth material response is known. The temperature and heat conduction are known as functions of time at any depth between the original surface and the TC1 location. If the surface is assumed to be at a specific depth at a given time, the required surface heat rate which would maintain the same in-depth thermal response can be calculated. In equation 29, all the parameters in the second, third and fourth terms are known at any location and time; therefore, the first term can be readily calculated for the entire time and depth domain, thus creating an estimated surface heat rate map for varying surface locations (Fig. 71a). The surface heat rate can then be estimated for a pre-defined recession profile using this map. One approach for choosing such a recession profile is to scale the recession profile calculated by the nominal PICA ablation model for the nominal heating environments. Recession

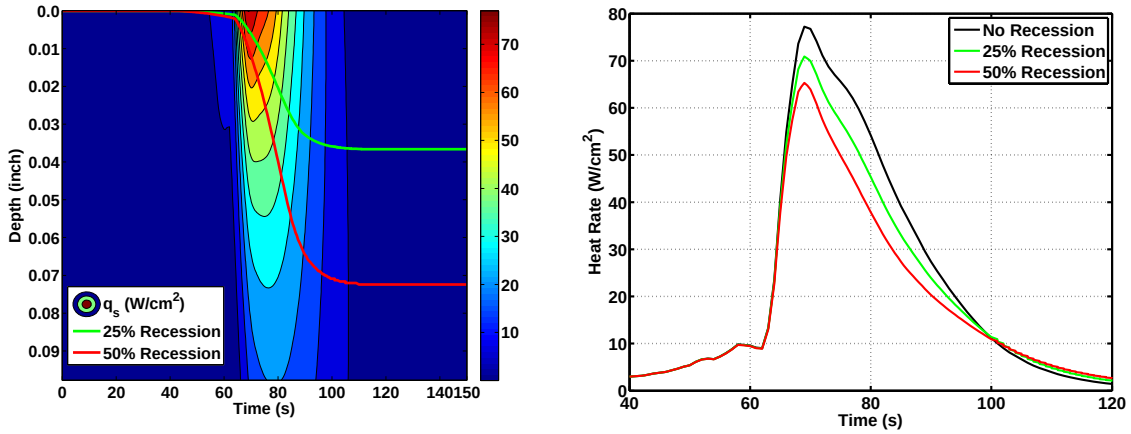

(a) Estimated heat rate map for varying surface locations

(b) Surface heat rate profile for pre-defined recession profiles

Figure 71: Effect of surface recession uncertainty on heating estimation results.

profiles scaled to 25% and 50% are overlayed on the surface heat rate map shown in the same figure. Figure 71b shows the estimated surface heat rate for these pre-defined recession profiles. It can be seen that increased surface recession results in a lower estimated surface heating because the surface becomes closer to TC1, requiring a lower surface heating to maintain the same in-depth temperature response. It can also be observed that the recession sensitivity is not significant in the first 65 seconds when surface recession is small.

It should be noted that this analysis only shows the conduction effect of recession. Chemical processes that happen during recession can have additional effects on the surface heating. This analysis demonstrated the significant effect that recession uncertainty has on the estimated surface heating profile and provides a motivation for the developement of a recession sensor for future flight experiments.

5.4.2.4 Material Property Sensitivity

Figure 72 shows the sensitivity of the estimated surface heating profile at plug 2 to perturbations in different PICA material properties. For this sensitivity analysis, a fixed ±10% perturbation is applied to both virgin and char properties. Figure 72a

shows that an increase in material density results in higher estimated surface heating for the entire time period. Higher density means a higher material thermal mass and consequently a higher surface heating is required to maintain the same temperature response. The effect is most visible around the peak region. Pre-flight density

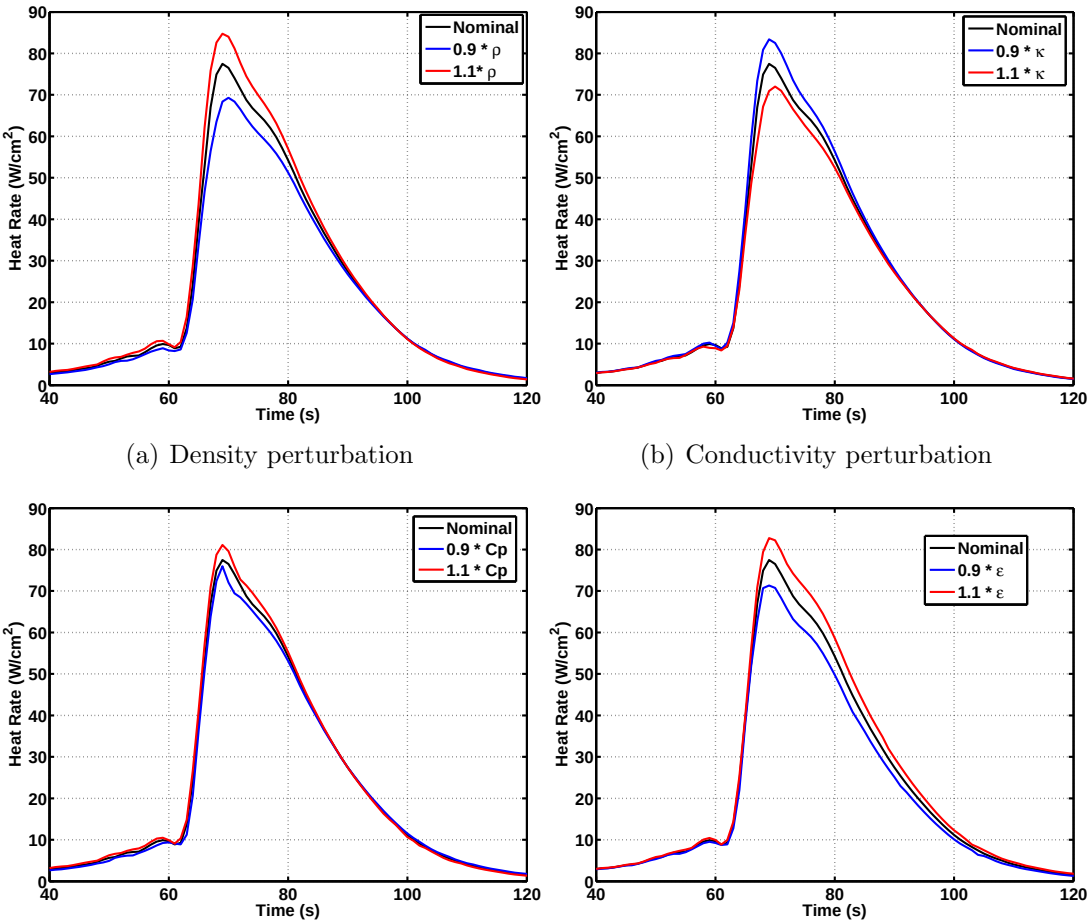

(a) Density perturbation

(b) Conductivity perturbation

(c) Specific heat perturbation

(d) Emissivity perturbation

Figure 72: Effect of PICA material property perturbations on heating estimation results.

measurement of the MISP plugs indicate only a ±1.5% variation in virgin density; therefore, the effect of density uncertainty on estimated surface heating is expected to be small. Figure 72b shows the effect of thermal conductivity perturbation. It can be observed that a higher thermal conductivity leads to higher heat conduction into the material, resulting in a lower surface heating required to maintain the same

temperature response. Figure 72c shows the effect of specific heat perturbation. Similar to density, higher specific heat leads to a higher thermal mass which results in a higher estimated surface heating. However, the sensitivity to specific heat is far less than sensitivity to density. Finally, Fig. 72d shows the effect of surface emissivity perturbation. Higher surface emissivity leads to higher reradiation and lower heat conduction into the material. Consequently, higher incoming heating is required to maintain the same in-depth response. It can also be observed that the estimation sensitivity to emissivity is significant only during the peak and post-peak regions when significant reradiation is expected due to higher wall temperature.

5.4.2.5 Uncertainty Quantification

A Monte Carlo analysis was performed on the inverse estimation procedure to quantify the uncertainty associated with the estimated surface heating profiles. Each Monte Carlo iteration performs a surface heating estimation for a set of input parameters. Eight input parameters are varied in the simulation using Gaussian distributions. Table 8 provides the standard deviation for these parameters. These values are derived based on engineering judgment and material property characterization experiments conducted on material samples from the same PICA billets that the MISP flight plugs originated from. For example, the virgin density of the flight MISP plugs is measured to be within $\pm 1.5\%$ of the nominal PICA density. Assuming that this interval represents $\pm 2\sigma$ bounds, the standard deviation is estimated to be 0.75% of the nominal value. The standard deviations for other parameters are estimated in a similar manner. Char density is correlated to virgin density by using a fixed char yield value (with a 1% standard deviation) to derive the char density from virgin density. Virgin and char thermal conductivity are also correlated.

The Monte Carlo analysis is conducted for 2000 iterations. Then, the standard deviations are calculated as functions of time for the estimated surface heat rate

Table 8: Standard deviation for Monte Carlo simulation parameters.

Par.	Std. Dev. (% of nominal)	Par.	Std. Dev. (% of nominal)
ρ_v	0.75%	Char yield	1% (corr.)
Cp_v	4%	Cp_c	1%
κ_v	7.5%	κ_c	10% (corr.)
$\epsilon_{v,c}$	1.5%	TC1 depth error	0.0015 inch

profiles obtained from the Monte Carlo results. After about 1000 iterations, the peak heat rate standard deviation stabilized and did not change significantly, affirming the analysis convergence. Figure 73 shows the 95-percentile bounds ($\pm 1.96\sigma$) for the estimated heat rate profiles at plugs 1, 2, 5 and 7.

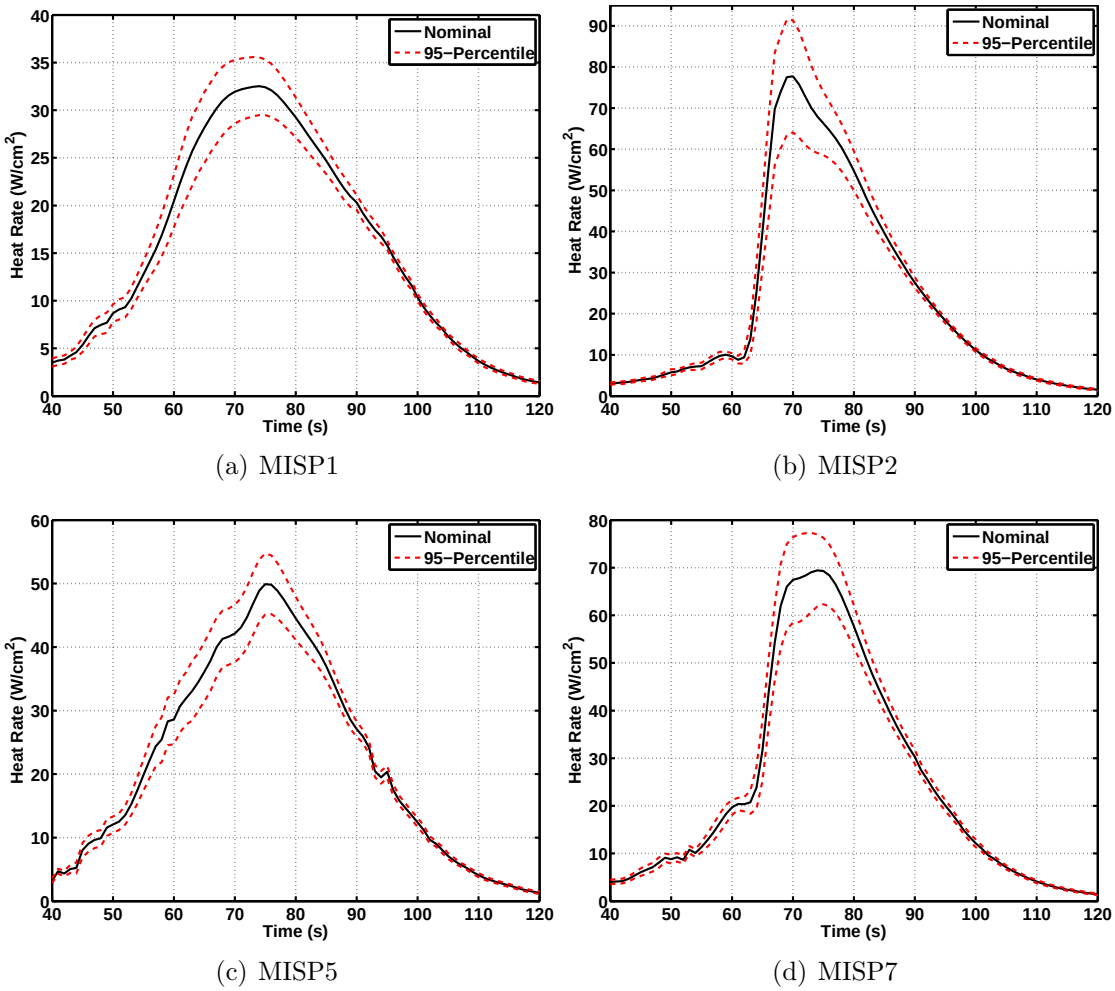

(a) MISP1 (b) MISP2

(c) MISP5 (d) MISP7

Figure 73: Estimated heat rate 95-percentile bounds at plugs 1, 2, 5 and 7 derived from the Monte Carlo analysis.

Figure 74 shows the surface heat rate standard deviation for all plugs derived from the Monte Carlo results. It is evident that the plugs with higher nominal heating also have a higher uncertainty. The maximum heat rate standard deviation for plug 2 happens around the peak heating time and is about 7 W/cm^2 which is almost 10% of the nominal surface heating value. The maximum heat rate standard deviation for plug 4 is less than 2 W/cm^2 which is about 6% of its peak heating value. It should be noted that this Monte Carlo analysis does not include the effect of recession uncertainty because the recession sensitivity is determined based on post-estimation computations and relies on an arbitrarily predefined recession profile. The recession sensitivity analysis performed earlier provides an indication of the expected level of uncertainty due to recession.

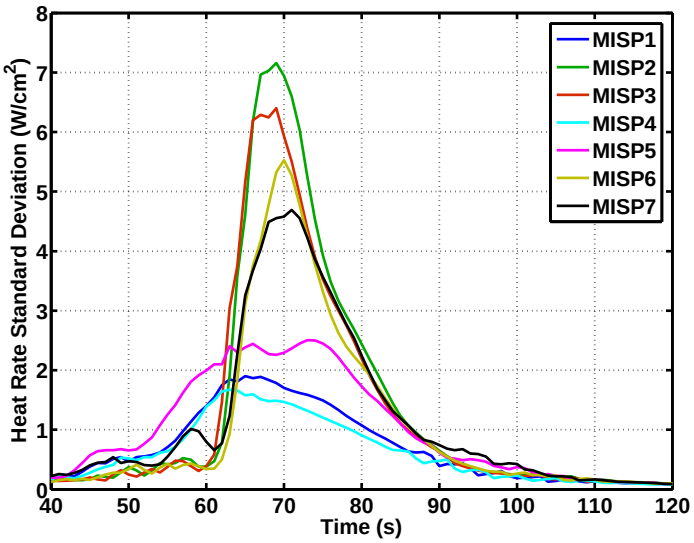

Figure 74: Heat rate estimation standard deviation derived from the Monte Carlo analysis.

5.5 Material Property Estimation

As mentioned in Chapter 2, simultaneous estimation of material properties and time-varying surface heating is a challenging problem because the surface energy balance and the in-depth material response problems are tightly coupled. In this situation,

the thermocouple (TC) driver approach is used to estimate PICA material properties from MISP flight data. In this approach, the data from the thermocouple closest to the surface (TC1) is used as the temperature boundary condition at that thermocouple location and the in-depth heat transfer and pyrolysis problem is solved for the material stack beneath that thermocouple. As such, this approach effectively decouples the in-depth heat transfer and surface heating problems, allowing the application of inverse methods to estimate material properties from TC2-4 temperature data without requiring knowledge of surface heating conditions.

A multi-parameter estimation framework was developed in Chapter 2 and applied to arc jet data in Chapter 3. In this section, this framework is employed to estimate PICA material properties from MSL heatshield temperature data using the TC driver approach. This framework proposes guidelines on how to conduct the parameter estimation via four steps: nominal analysis, uncertainty analysis, sensitivity analysis, and inverse analysis. The first three steps provide the prerequisite information to set up a successful inverse estimation. In the last step, inverse methods are used to estimate the selected parameters from the data. For the sake of brevity, the analysis presented here will focus on material property estimation at plug 2. Similar analyses can be performed for other plugs.

5.5.1 Nominal Analysis

In the TC driver approach, the temperature data from the shallowest thermocouple (TC1) is used as the true boundary condition and the thermal response for the underlying material is calculated using FIAT and nominal PICA properties. It should be noted that while TC1 data can be deemed as the true material temperature at TC1 depth, there is a ± 0.003 inch uncertainty in the location of thermocouples ($\pm 2\sigma$). In this analysis, two bounding scenarios are considered in addition to the nominal TC depths to account for their location uncertainty. In one scenario, TC1 depth is

offset by +0.003 inch while TC2-4 depths are offset by −0.003 inch. This will lead to the farthest possible separation between the driver thermocouple and the underlying ones, thus resulting in a lower bound for temperature predictions. In another scenario, TC1 depth is offset by −0.003 inch while TC2-4 depths are offset by +0.003 inch leading to the closest distance between TC1 and TC2-4 and thus a higher bound for temperature predictions. In this work, results from these scenarios are respectively labeled as "lower" and "upper" bounds.

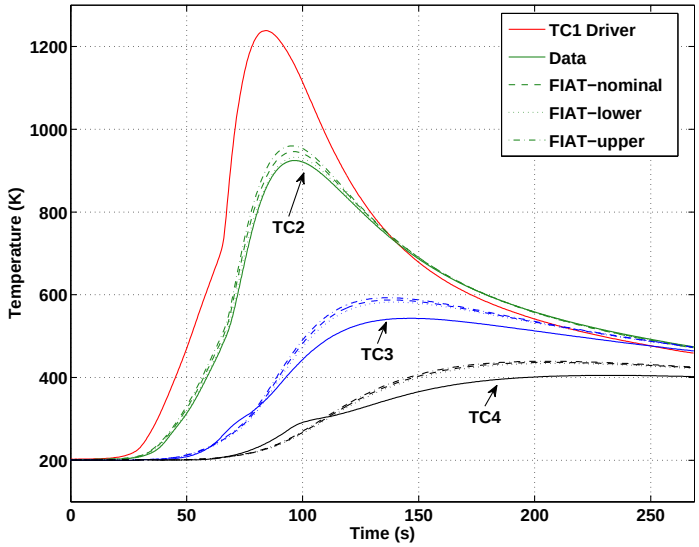

Figure 75: FIAT predictions compared to flight temperature data using a TC1 driver approach at plug 2.

Figure 75 shows the comparison between the FIAT predictions and TC2-4 flight temperature data using a TC1 driver approach at plug 2. The lower and upper-bound FIAT predictions are presented in addition to the nominal predictions. It can be observed that the nominal FIAT solutions slightly overpredict the flight data at TC2 location; however, the flight temperatures are close to the lower bound of the FIAT temperature predictions. At TC3-4 locations, all three FIAT solutions significantly overpredict the flight data. Considering the fact that TC3-4 are mainly in the virgin material, this overprediction is indicative of inaccuracies in virgin material properties. As mentioned earlier, there is an unexpected slope change ("hump") in the TC3-4

temperature profiles. The hump happens in the 200-400 K temperature range. This trend is observed consistently for all plug locations. Current analysis tools are not able to model this behavior; therefore, a match between the data and model predictions should not be expected for this part of the data. For this reason, the TC3-4 data range used here in inverse analysis is limited to the time after the clearance of this slope change. This corresponds to the time period after about 92 and 195 seconds for TC3 and TC4 respectively.

5.5.2 Uncertainty and Sensitivity Analysis

The goal of uncertainty analysis is to define the material properties that contribute the most to the uncertainty in the heatshield material in-depth thermal response. The approach employed to accomplish this goal is probabilistic, and is accomplished with Monte Carlo simulations. This process starts with a complete list of material parameters which are then down-selected to a smaller subset containing parameters of most importance that should be estimated by inverse methods. This analysis should not be confused with the Monte Carlo analysis presented in the previous section which was performed around the inverse analysis procedure to determine uncertainties in the estimated surface heating. Unlike that analysis, this Monte Carlo simulation is performed around the forward analysis by varying material properties and recording the material in-depth temperature response. The input probability distributions shown in Table 8 for material properties are also used here with the addition of pyrolysis gas enthalpy, h_g. A Gaussian distribution with a standard deviation of 7.5% of the nominal value is applied for this parameter. [132] To ensure statistical accuracy, 10,000 runs are performed. Upon completion of the Monte Carlo simulations, a linear regression analysis of the results is conducted to calculate the uncertainty contribution of the material properties to in-depth temperature response. Figure 76 shows the uncertainty contribution of different properties to TC2 and TC3

temperature as a function of time. The results for TC4 are not shown here because they are very similar to TC3 results. It is evident that the virgin and char thermal conductivity are the top contributors to both TC2 and TC3 temperature uncertainty followed by the virgin and char specific heat.

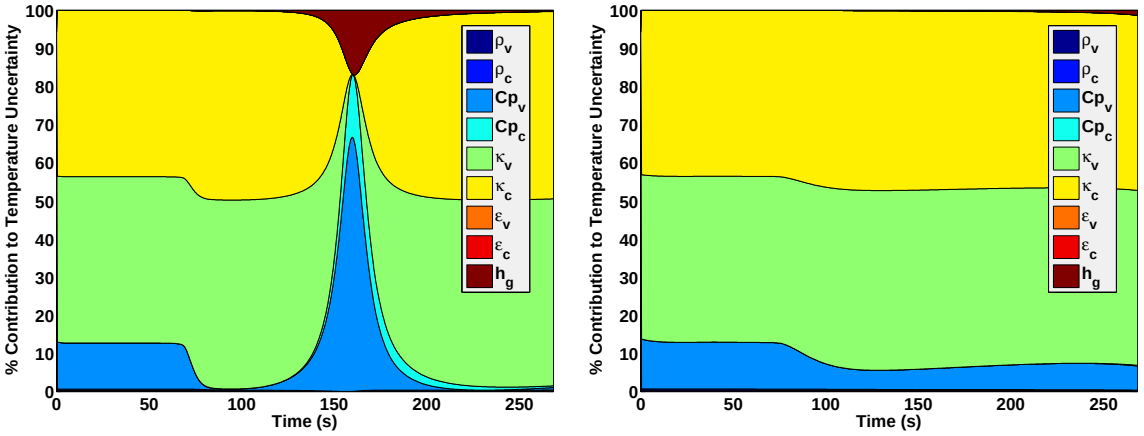

(a) Uncertainty contribution at TC2

(b) Uncertainty contribution at TC3

Figure 76: Material property contribution to in-depth temperature uncertainty at plug 2.

Before any attempt to estimate these parameters, a sensitivity analysis must be performed to examine the level of linear dependency among them. In this analysis, each parameter is perturbed independently by a small amount ($\pm 0.5\%$) and the change in in-depth temperature is recorded. Figure 77 shows the results of this sensitivity analysis for TC2 and TC3 locations at plug 2. Only the parameters that have been identified as the top uncertainty contributors are included in this step. Examination of the shape and magnitude of these plots gives an indication of the level of correlation between these parameters. There is a strong correlation between specific heat and thermal conductivity. The reason for this behavior is that the heat transfer through the material is mainly driven by thermal diffusivity which is directly proportional to the thermal conductivity and inversely proportional to the specific heat. Therefore increasing one or reducing the other one will have the same effect on the in-depth temperature response. This strong correlation means that in the presence

of measurement errors these parameters cannot be estimated simultaneously as they are not independently observable from the flight temperature data.

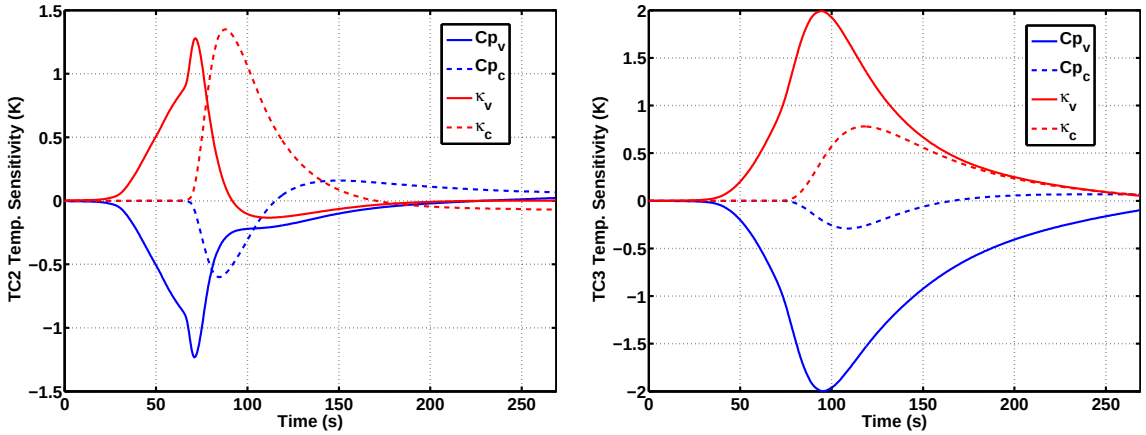

(a) Temperature sensitivity at TC2

(b) Temperature sensitivity at TC3

Figure 77: Plug 2 in-depth temperature sensitivity to one-by-one perturbations in material properties.

5.5.3 Inverse Analysis

Uncertainty and sensitivity analyses helped determine that virgin and char thermal conductivity are not linearly dependent and contribute the most to in-depth temperature uncertainty. Through nominal analysis, it was also identified the range of TC2-4 measurements that should be used in the inverse analysis. Now, inverse parameter estimation methods are applied to the TC driver problem to estimate these two parameters leading to a better match between FIAT temperature predictions and TC2-4 flight data. Similar to heating reconstruction, the estimation is done by minimizing an objective function comprised of the sum of squared differences between FIAT predictions and flight data. The minimization is performed using the Levenberg-Marquardt method. The detailed algorithm for this method can be found in Chapter 2.

The inverse analysis is performed for the lower and upper bound scenarios in addition to the nominal TC depths. This will enable the determination of the expected

range of parameter estimates due to TC depth uncertainty. Table 9 shows the estimates for PICA virgin and char conductivity at plug 2. The estimates given here are scaling factors multiplied by the entire temperature-dependent thermal conductivity curve. For example, a value of 0.9 would mean a 10% reduction in the thermal conductivity nominal value at all temperatures.

Table 9: Material property estimation results for plug 2.

Parameter	Estimate	Lower-Bound Est.	Upper-Bound Est.
Virgin Conductivity	0.7902	0.8079	0.7749
Char Conductivity	0.7878	0.8714	0.7051

The inverse estimation requires about 20% reduction in both virgin and char thermal conductivity to provide a better match with the flight data. This reduction is within the 3σ uncertainty bounds for these parameters. It can be seen that the sensitivity of char conductivity estimate to TC depth uncertainty is much greater than virgin conductivity. Figure 78 shows the comparison of TC2-4 flight temperature data with the nominal and post-estimation FIAT predictions. These plots are generated for the nominal TC depth scenario. It is clear that a better match between FIAT predictions and flight data is achieved after inverse estimation of virgin and char thermal conductivity. The root mean square of errors is reduced by a factor of almost four.

It should be noted that the material property estimation analysis presented here can easily be extended to other plugs and other thermocouple driver possibilities. For example, one can conduct this analysis for a TC2 or TC3 driver at plug 1 to focus mainly on virgin properties. In each one of these cases, a separate uncertainty and sensitivity analysis can be performed to identify the properties that should be estimated. Unfortunately, all these possibilities currently can not be explored due to the observed slope change ("hump") in the TC3-4 data which significantly reduces the confidence in the inverse estimates. Further material property estimation work

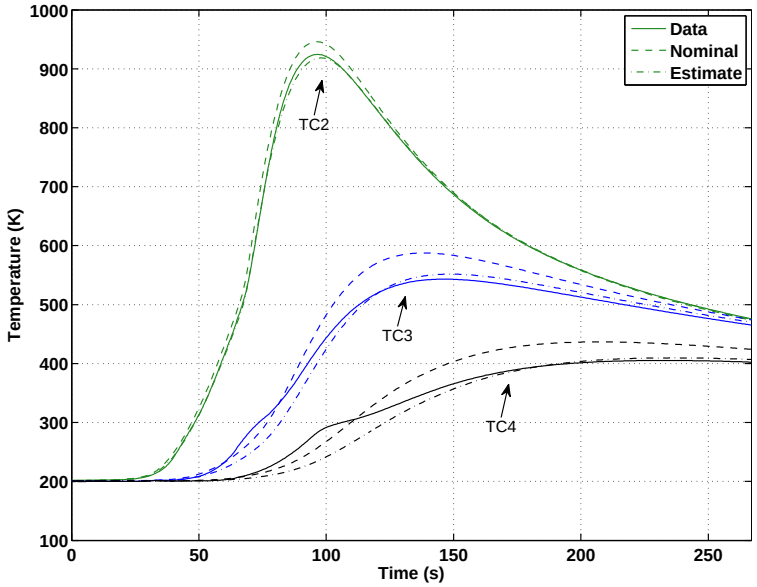

Figure 78: Flight temperature data compared with the nominal and post estimation FIAT predictions for plug 2 TC1 driver.

should be pursued once this behavior is understood and modeled in the analytical tools. Furthermore, the current analysis estimated the virgin and char conductivity by uniformly scaling their temperature-dependent curve. In future, temperature-dependent estimation of these properties can also be pursued to obtain more accurate conductivity curves.

5.6 Modification of TPS Design Margin Policies

5.6.1 MSL Heatshield Design Margin Methodology

The MSL heatshield was designed and sized using a more rigorous thermal margins policy as compared with previous missions. The margin methodology employed for MSL is explained in Refs. [149, 150] in detail. Figure 79 from Ref. [149] highlights the margin process, which evaluates uncertainties due to entry trajectory dispersions, aerothermal environments, material response, and recession rate. First, the trajectory analysis team generated Monte Carlo dispersed trajectories for the mission. Bounding ($+3\sigma$) heat load and heat rate trajectories were then selected for detailed aerothermal

and TPS analysis. The laminar and turbulent aeroheating environments were characterized using CFD tools such as LAURA or DPLR. In the case of MSL, only the fully turbulent environments were used in the sizing process because predictions indicated boundary-layer transition early in the trajectory. The heating environments were calculated using conservative assumptions such as supercatalytic wall which results in peak heating levels as high as about 200 W/cm^2. [149] The uncertainties associated with these predictions including turbulence model and roughness augmentation uncertainties were also calculated.

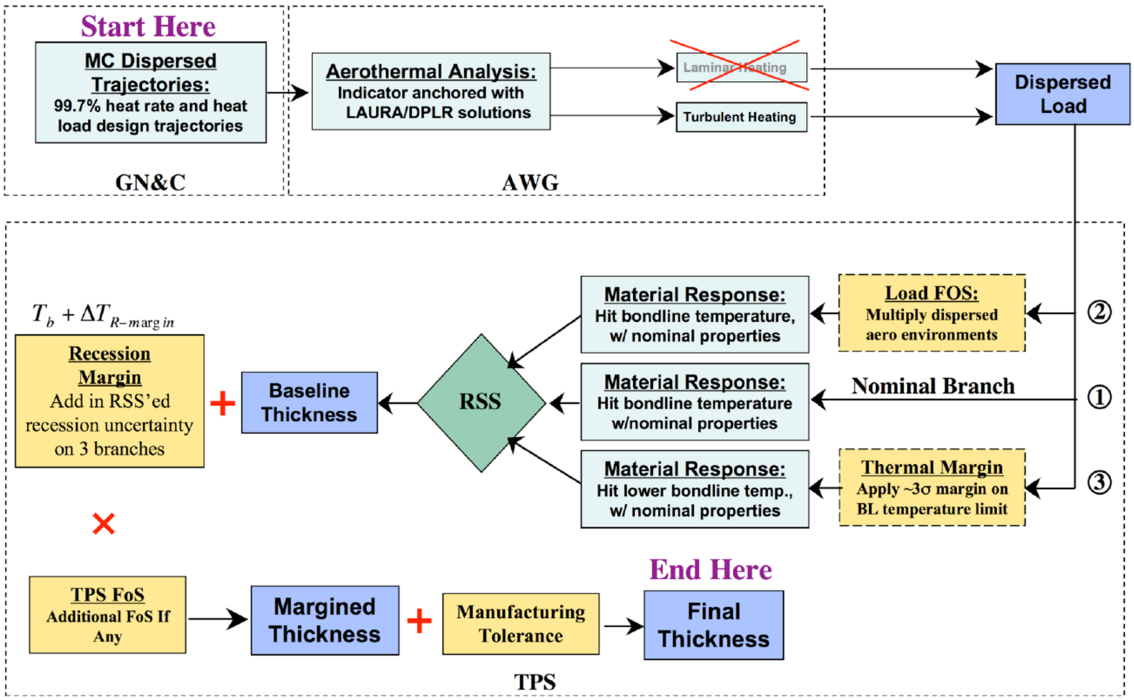

Figure 79: Flowchart of the TPS margin process employed for MSL.

The margin process is then performed by calculating the required TPS thickness to maintain a bondline temperature of 250 $°C$, the limiting temperature for the RTV bonding used between the TPS and substructure. The TPS thickness calculation was done using the NASA code FIAT and is performed in three separate branches of the Figure 79 flowchart. The first branch used the nominal heating with the nominal material response model. The second branch applied the aerothermal uncertainties to

the nominal heating environment. The third branch applied a margin to the bondline temperature used in the sizing. This margin accounts for TPS and substructure material variability and is calculated using a separate FIAT Monte Carlo analysis with a dispersed material model. [132] Finally, these uncertainties are combined in a Root Sum Squared (RSS) process to arrive at the baseline thickness.

The next step was to apply the recession margin. During arc jet testings of PICA in shear environments (non-stagnation), it was observed that the material ablation model in FIAT underpredicted the measured recession by an average 50%. [151] However in some cases, the recession mismatch was as high as 150%. Furthermore, at heat rates higher than about 100 W/cm^2, PICA recession is diffusion-limited and depends directly on oxygen availability and indirectly on recovery enthalpy. In a Martian dissociated CO_2 turbulent flow, the available oxygen is higher and the recovery enthalpy is lower than Earth atmosphere. [149] Therefore, the project decided at the time to apply an extremely conservative 150% recession bias to the FIAT-calculated recession and add this bias to the baseline thickness. Analysis performed since then has shown that some of the recession mismatch was due to the arc jet model design which resulted in a much more oxygen-rich boundary layer than expected in flight. [152] Finally, the recession-biased thickness is multiplied by a program-imposed factor of safety in addition to manufacturing tolerances to arrive at the final TPS thickness.

Due to a late change of TPS material, the heatshield had to be built while the design was still ongoing. As a result, the MSL process was unlike a traditional design process where the as-built thickness is based on the final TPS sizing. Instead, the TPS thickness of 1.25 inch was selected based on the maximum amount of available mass. The process shown in Figure 79 was still used, except that designers instead were left to demonstrate that the heatshield thickness would be sufficient. Fortunately, the TPS margin process ultimately showed that 1.25 inch of TPS was more than sufficient. The difference between the as-built and the final thickness was treated as

an "extra thickness".

Figure 80 from Ref. [149] shows the result of that sizing process for the critical location on the heatshield, where the margined TPS thickness was the greatest. Each of the contributors in the margins process flowchart are shown in terms of their contribution to the as-built TPS thickness. Starting from the bottom, the zero margin thickness is the largest contributor. This represents the nominal branch of TPS sizing without any explicit margin added. It is roughly 60% of the total thickness. The next contributor is the "heating margin" which is margin added to cover uncertainties in the aerothermal environments. It is considerably smaller than the nominal thickness, and is less than 10% of the overall thickness. The thermal margin follows, which similar to the heating margin has a small contribution. The "recession margin" is the largest margin contributor. This is due to the extremely conservative bias which makes the margin process recession-dominated. The final component is the "extra margin" which accounts for the difference between the final margined design thickness and the as-built TPS thickness.

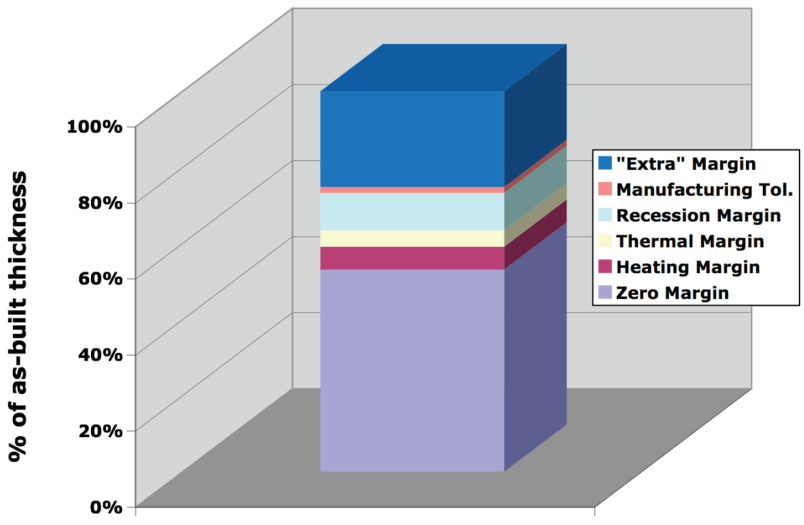

Figure 80: Components of as-built heatshield forebody TPS thickness.

5.6.2 Contributions of MSL Data to Design Margin Policy Improvement

Improvements to the heatshield design process have often been hampered by a lack of flight data. Fortunately, the MSL heatshield was instrumented, and valuable aerothermal environment and heatshield performance data were gathered. The inverse analysis performed in this chapter provided great insight into the aerothermal environment experienced by MSL and its TPS response. This section presents a discussion of how findings from MSL raw data and post-flight analysis may improve the TPS design margin policies.

As discussed in the previous section, TPS sizing is driven by a bondline temperature limit, which was 250 $^{\circ}C$ for MSL mission. The measurement of the flight vehicle bondline temperature at the depth of 1.25 inch would be very useful in assessing TPS performance. However, TC4 (nominal depth of 0.75 inch) is the deepest direct TPS temperature measurement available from the MSL flight data. Figure 81 shows TC3

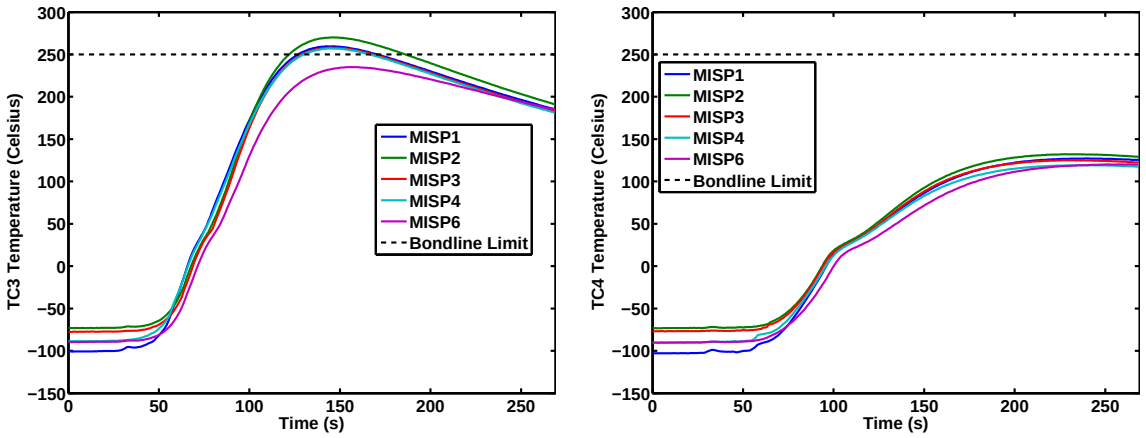

Figure 81: MISP TC3-4 flight data compared to the bondline temperature limit.

and TC4 flight data as a function of time for all plugs. It is clear that the temperature at TC4 did not reach the bondline temperature limit at all plug locations. Temperature at TC3 (nominal depth of 0.45 inch) reached this limit for some of the plugs. This trend was expected because the design margins used in the sizing process were very conservative. Unfortunately, TC3-4 data at plugs 5 and 7 are not available due

to data channel limitations.

The bondline temperature can be estimated using the TC driver approach, introduced earlier. The flight temperature data from the deepest thermocouple is applied as the boundary condition and FIAT is employed to calculate the thermal response for the underlying TPS with the nominal material model. Since TC3-4 data are not available at plugs 5 and 7, TC2 data is used as the driver temperature. This will ensure consistency among all plugs. Figure 82 shows the estimated bondline temperature profile at all plugs. It should be emphasized that due to material model uncertainties this calculation is only an estimate of the flight bondline temperature. Clearly, none of the plugs experienced anything approaching the design bondline temperature limit of 250 $^{\circ}C$ prior to heatshield ejection at 268 seconds.

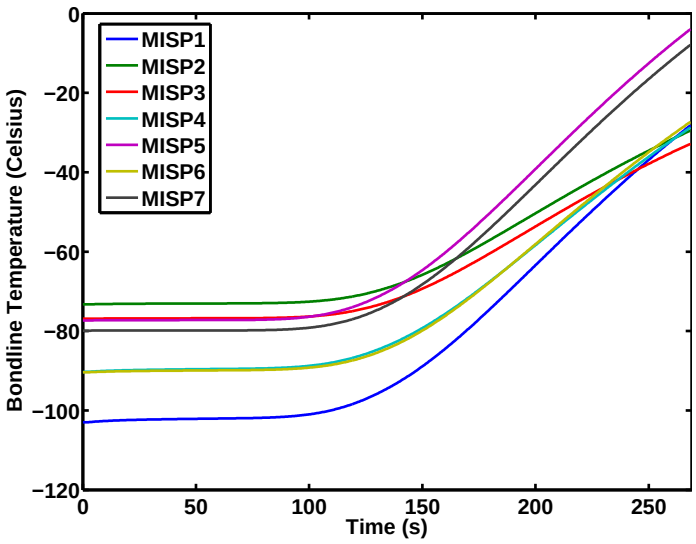

Figure 82: Estimated MSL bondline temperature at MISP locations.

Plugs 5, 7 and 1 had the highest rise in bondline temperature while plugs 2 and 3 had the lowest. This might seem counter-intuitive because analysis in the previous chapter showed that plug 2 had the highest peak heating. However, a closer examination of the estimated heating profiles reveals that plugs 5, 7 and 1 experienced higher laminar heating than plugs 2 and 3 before transition to turbulence, resulting in a higher heat load for these plugs. Due to the delayed nature of heat transfer, the

bondline temperature was still rising when heatshield was jettisoned and had not yet reached its peak. Additionally, the TPS substructure at plugs 2 and 3 was made of a denser aluminum honeycomb. These two reasons, combined, explain for the lower temperature rise at plugs 2 and 3.

In addition to estimating the bondline temperature, a nominal unmargined TPS sizing can be performed using the TC driver approach. TC2 temperature is applied as boundary condition and FIAT is used to calculate the TPS thickness required to maintain the bondline temperature below 250 $^{\circ}C$ at 268 seconds when the heatshield is jettisoned. Then, this calculated thickness is added to TC2 depth to arrive at the total required TPS thickness. Table 10 shows the required unmargined TPS thickness at all plug locations. It is evident that less than half of the design thickness was required to shield the spacecraft. Of course, heatshield designers must ensure payload safety and have to address many unknowns, particularly when working with challenging entry conditions, new mission concepts, and TPS materials. The successful landing of Curiosity and the thermocouple data returned demonstrates that the MSL heatshield was conservatively designed and performed well.

Table 10: Unmargined TPS thickness required at plug locations for MSL as-flown trajectory (Flight heatshield was 1.25 inch thick).

Plug	Thickness (inch)
MISP1	0.463
MISP2	0.346
MISP3	0.338
MISP4	0.407
MISP5	0.515
MISP6	0.420
MISP7	0.506

5.6.2.1 Aerothermal Design Improvements

In the current MSL margin process shown in Figure 79, the margins for aeroheating analysis stem from trajectory dispersions and environment prediction uncertainty.

Reducing trajectory dispersions is not the focus of this work. A better knowledge of atmosphere, planetary gravity field and vehicle's navigation and aerodynamic parameters are required for lower trajectory dispersions. However, aerothermal environment prediction currently involves conservative assumptions and biases such as fully turbulent flow, supercatalytic wall, roughness-induced heating augmentations and stagnation region augmentation. [6] Some of these assumptions and biases can be reconsidered in the light of MSL flight and ground test data.

Turbulent transition was observed in the MSL flight data and an accurate transition time was derived from the estimated surface heating profiles. Flight observations did not match the model predictions of transition time based on a smooth-wall momentum thickness Reynolds number threshold. Predictions based on roughness Reynolds number showed a much better agreement with the data, indicating that MSL transition was likely induced by roughness. However, the roughness height used in this analysis was considerably higher than PICA average distributed roughness height observed in ground testing, implying that transition was caused by a discrete roughness element such as the fencing of RTV bond between PICA tiles. For future missions similar to MSL using PICA, roughness-induced transition must be examined further. However at the current time, our capability of predicting transition time and location on an ablating body is not mature enough to use transitional environments in design. If boundary layer transition is suspected, fully turbulent flow must be assumed for design and sizing purposes. Turbulent flow calculations using the Baldwin-Lomax algebraic model have shown good agreement with the estimated environments from MSL, Pathfinder and also ground test data.

A "supercatalytic wall" model is often used in design aerothermal calculations which assumes the recombination of all atoms to the lowest chemical enthalpy state (CO_2/N_2). This assumption is used in design because it represents the limiting

case of highest heating possible, even though it is not physically based. In practice, other assumptions such as the Mitcheltree or non-catalytic wall models are also used. The estimated MSL and Pathfinder surface heating profiles were consistent with the Mitcheltree model calculations suggesting that this model is likely more representative of flight heating than the supercatalytic wall assumption. For future missions, catalycity calculations can be only improved with better ground testing techniques designed to identify relevant reactions and measure their rates. For example, the primary surface reaction for PICA is carbon oxidation; therefore, a validated finite-rate gas surface interaction model implemented in the CFD tools can greatly reduce uncertainties in model predictions.

Finally, future sizing and margin processes should include coupled aeroheating and TPS response analysis for a more accurate calculation of heating environments. The current process is decoupled and does not accurately capture all the physical phenomena that occur at the material surface. A coupled analysis will also enable a more sophisticated uncertainty propagation technique. The current process uses a simple RSS approach which results in the compounding of multiple uncertainty contributions.

5.6.2.2 TPS Design Improvements

The margins in TPS material design come from two sources: in-depth thermal response and surface recession. The thermal response margin is applied in the form of a required bondline temperature margin and is due to uncertainties in material properties and pyrolysis parameters. Although some material properties were estimated using the framework developed in this work, these results do not necessarily contribute to design margin reduction. The estimated values for material properties are for a given material sample at a given plug. Due to the variability in PICA material properties, different estimates can be obtained at other plugs. The number of plugs is

not high enough to obtain any significant statistical information on the variability of material properties. Therefore, any attempt to reduce thermal margins should focus on improving manufacturing capabilities in order to ensure more consistency and less variability in material properties. Application of the inverse methodology developed in this work to a wide range of arc jet datasets can be beneficial in obtaining accurate statistical information on the variability of material properties. Such information can be later used in a Monte Carlo process to calculate more representative bondline temperature dispersions and develop more realistic margins.

Recession margin can be reduced substantially. As discussed before, the MSL mission used a 150% recession bias due to observed higher recession in shear environment arc jet tests as compared to equilibrium model predictions. Later analysis concluded that increased recession was due to arc jet model design. [152] MSL data clearly showed that the flight recession was not higher than model predictions; it was considerably less. Therefore, in future PICA heatshield designs in similar environments, the recession bias can be completely removed. PICA recession at MSL heating conditions is not well estimated by equilibrium models and is generally overpredicted. A better estimate of surface recession can be obtained if validated and accurate finite-rate gas surface chemistry models are developed and used for PICA.

5.7 Summary

An inverse analysis of the MSL entry vehicle aeroheating environment and thermal protection system response was performed in this chapter based on heatshield flight temperature data. The time-dependent surface heating at MISP plug locations was reconstructed from the shallowest thermocouple flight data using two different approaches. The first approach estimated the heat transfer coefficient profile while relying on PICA equilibrium chemistry models to calculate surface ablation terms. A disadvantage of this approach is the fact that equilibrium chemistry models are known

to overpredict surface recession at MSL heating conditions. Consequently, another bounding approach was considered where the surface heating was directly estimated assuming a non-receding material surface. This work also investigated the effect of numerical parameters, measurement errors, recession uncertainty, and material property perturbations on the estimated surface heating profiles. A Monte Carlo analysis was performed for all plug locations to determine the uncertainty bounds associated with the estimated surface heating profiles.

Additionally, significant material properties were inversely estimated using a TC driver approach. In this approach, the data from the shallowest thermocouple were used for the true boundary condition and material properties were estimated to match FIAT predictions with the underlying thermocouple flight data. A four-step methodology was utilized to determine which material properties should be estimated and what range of temperature data should be used in the estimation. An uncertainty analysis was performed to determine the most important material properties based on their contribution to in-depth temperature uncertainty. A sensitivity analysis was conducted to investigate the level of linear dependency among the material properties to determine which parameters are simultaneously observable from the data. Virgin and char thermal conductivity were estimated by using inverse methods to match FIAT predictions with flight data. This analysis was performed for plug 2 on the MSL heatshield, but can easily be extended to other plugs.

MSL aeroheating reconstruction demonstrated that the estimated heating profiles for the leeside plugs (2, 3, and 6) match the CFD predictions, although the turbulent heating augmentation is slightly lower than predictions. Plugs 5 and 7, which are located around the apex region, experienced significantly higher heating than CFD predictions. The proximity of these plugs to the location of turbulent transition and possible shock-layer radiative heating could explain this phenomenon. The estimated heat rate profile at the stagnation region plugs (1 and 4) are slightly higher than CFD

predictions which can be explained partially by radiative heating. The estimated surface heating profiles were shown to be sensitive to surface recession.

The TC driver approach showed that the nominal PICA model overpredicts the temperature profile at TC3 and TC4 location consistently for all plug locations which is indicative of inaccuracy of virgin properties. Furthermore, a slope change was observed in the 200-400 K range in the temperature profiles of TC3 and TC4. This behavior has been seen in other ground and flight datasets.

Finally, the margin methodology used for the MSL aerothermal and TPS design was reviewed. A discussion of how findings from MSL data may improve the margin process for future missions was also presented.

CHAPTER VI

SUMMARY AND FUTURE WORK

6.1 Thesis Summary

There are substantial uncertainties in the current theoretical and computational models used for the prediction of entry aerothermal heating and TPS material response. Ground experimental and flight data will help reduce these uncertainties and improve the current computational capabilities. The MSL rover recently landed on the surface of Mars and provided valuable flight data. The analysis of TPS experimental data has traditionally been done in a direct fashion where model predictions are compared with the data. At best, only high-level qualitative observations regarding TPS performance have been made in the past based on the adjustment of a few parameters or simple scaling of the surface heating profile. However, an inverse analysis is capable of identifying the material model parameters from the data and also estimating the complete time-dependent surface heating profile.

In this thesis, an inverse estimation methodology was developed for the analysis of TPS experimental data. Application of this methodology was demonstrated using many test problems. The estimation methodology is comprised of two distinct parts. The first part is a multi-parameter estimation framework developed for inverse problems where multiple constant parameters such as material properties need to be estimated. The developed framework performs multiple supporting analyses which help identify what parameters should be estimated and what range of the measurements should be used. The second part of the methodology is the surface heating function estimation framework which is aimed at problems where the time-dependent surface heating is reconstructed from in-depth temperature data. This framework identifies

the temperature data and the surface heating parameters that are appropriate for a given problem and provides guidelines on how to perform the estimation.

Chapter 1 discussed the motivation and provided a background for the topics related to this work. The techniques currently employed for prediction of entry aerothermal environment and ablative TPS material response modeling were reviewed. Significant uncertainties in these models were examined and current research areas were discussed. A review of past heatshield flight data was given and the MEDLI instrument was described in detail focusing on its aeroheating and TPS subsystem, MISP. Chapter 2 discussed the difference between direct and inverse analyses, provided a background on inverse heat transfer problems and described the developed inverse estimation methodology in detail.

In Chapter 3, the multi-parameter estimation framework was applied to MSL-relevant arc jet test data. Nominal, uncertainty and sensitivity analyses were performed to intelligently select the range of measurements and the set of parameters used in the inverse estimation process. For the arc jet problem, multiple constant material and aerothermal parameters were estimated and a good match between the data and model predictions was achieved. Through application of this framework, the advantage of an inverse multi-parameter estimation approach over the traditional direct approach was demonstrated. This framework can be easily applied to future arc jet test data. Furthermore, the concepts and analyses developed for this framework can be readily extended to multi-parameter estimation problems in other science and engineering fields.

Unlike the arc jet problem, flight vehicle surface heating is time-dependent and its estimation is a challenging function estimation problem. In Chapter 4, the surface heating function estimation framework was demonstrated for two relevant applications. First, inverse methods were used to estimate MSL time-dependent surface heating profile from simulated data. In the case of simulated data, the true solution

was known, therefore, investigation of the effect of model and measurement errors on the accuracy of surface heating estimation was performed. Additionally, the feasibility and applicability of these methods were demonstrated through application to Mars Pathfinder heatshield flight data. Through this analysis, an improved estimation of Mars Pathfinder surface heating and TPS performance was accomplished.

Chapter 5 discussed the inverse analysis of MSL aerothermal environment and TPS material performance based on the MSL flight data using the developed inverse tools and frameworks. The surface heating profile was estimated at the seven plug locations from the shallowest thermocouple data. The effect of numerical parameters, measurement errors, recession uncertainty, and material property perturbations on the estimated surface heating profiles was investigated. A Monte Carlo analysis was performed for all plug locations to determine the uncertainty bounds associated with the estimated surface heating. A thermocouple driver approach was employed to apply the multi-parameter estimation framework to PICA material property estimation. Through this inverse analysis, accurate estimates of MSL time-dependent surface heating with associated uncertainties, turbulent transition time and location, and the PICA material performance at the plug locations were obtained. Also in Chapter 5, a review of the aerothermal and TPS design margin methodology used for MSL was presented followed by a discussion of how finding from MSL flight data may improve the margin process for future missions.

The next sections will provide some closing thoughts. Recommendations for future heatshield instrumentations will be provided. Certain improvements to the current suite and additional instruments can greatly improve the information obtained during post-flight data analysis. Finally, a discussion of possible augmentations to the inverse methodology is presented.

Table 11 provides a traceability matrix describing what chapters in this thesis discuss the academic contributions introduced in Chapter 1. The inverse estimation

methodology developed in this thesis enabled the first inverse analysis of an atmospheric entry heatshield flight dataset. The benefits of this inverse methodology goes beyond the applications demonstrated in this thesis. The tools and frameworks introduced here can be applied to future flight and ground test data as a complementary analysis approach to the traditional direct approach.

Table 11: Traceability of academic contributions.

Contribution	Ch. 2	Ch. 3	Ch. 4	Ch. 5
Development and Application of a Multi-parameter Estimation Framework	✓	✓		✓
Development and Application of a Surface Heating Function Estimation Framework	✓		✓	✓
First Inverse Analysis of a Mars Entry Vehicle Heatshield Flight Data			✓	✓
Improvement of Mars TPS Design Margin Policies				✓

6.2 Recommendations for Future Heatshield Instrumentation

The MSL MISP instrumentation provided a great improvement to our flight testing capability and provided more entry TPS data than all previous Mars missions combined. However, the analysis presented in this thesis showed that uncertainties associated with the instruments and models remain. Improvements to the current instruments and additional instrumentation possibilities that could significantly reduce analysis uncertainties are discussed in this section.

The analysis presented in this work only focused on the thermocouple data. As mentioned before, the MISP plugs were also a equipped with an isotherm sensor, called HEAT. This sensor was designed to measure the progression of an isotherm through the TPS. Previously used on the Galileo probe mission, this measurement was

correlated to surface recession. However, surface recession is not steady state for MSL and therefore the HEAT sensor did not provide any information regarding recession. Pre-flight testing and analysis by the MISP team had showed that the isotherm depth measured by this sensor can be correlated to PICA char depth. [144] Unfortunately, the flight data received from HEAT was very noisy and did not behave as expected. Currently, the team is investigating multiple theories as why HEAT sensor did not perform nominally and plans to conduct arc jet tests to further examine these issues. Sensors similar to HEAT are planned for flight on the Crew Exploration Vehicle and could be used in future Mars missions. Therefore, it is critical to better understand HEAT's flight anomalies and any shortcomings must be fixed so that useful data can be obtained in future missions.

The MISP instrumentation did not provide detailed information on TPS recession other than it was less than 0.1 inch (TC1 depth). Uncertainty in surface recession calculation leads to significant uncertainties in surface heating estimation. Therefore, it would be greatly beneficial to develop a flight sensor with the capability of direct recession measurement. Over the past decades, multiple instruments using different measuring techniques have been proposed for recession measurement in both ground and flight applications. [153, 154, 155, 156] Currently, NASA Ames is developing and testing an in-house recession sensor based on sapphire tube light pipes. This sensor functions based on the fact that a recessing heatshield surface opens up an optical path. The light from the ablative surface is then transmitted by a light pipe and measured by a photo detector indicating the current location of the surface. These development efforts will lead to higher technology readiness levels for recession sensors facilitating their use in future missions.

Another source of analysis uncertainty is heating from shock-layer radiation. Typically, radiometers and spectrometers are used to obtain flight data for the validation of radiation codes. The Apollo flight testing program and Project Fire were among

the first missions that employed radiometers. [4] These sensors might not be beneficial for Martian entries as radiation is not generally high enough to be measured accurately with radiometers. Such sensors can be useful in Earth entry mission where radiative heating is more substantial. Additionally, they can be employed in ground experiments to validate and improve the computational models that are later used for flight predictions.

A great amount of work went into the development of the MSL MISP instruments. However, because they had never been used on a heatshield before, the majority of pre-flight analysis and testing focused on ensuring that the heatshield performance was not compromised by the plug insertions. Future missions that use similar sensors must focus more on the actual performance of the instruments. A detailed sensor measurement uncertainty and error budget analysis can provide significantly more information on the accuracy of heating and material property estimations. Some examples are further characterization of thermocouple lag, measurement range and uncertainty, and thermocouple location. Additionally, improved thermocouple technologies can be used to reduce these errors. For example, Smart-K thermocouples are known to have lower thermal lag while type-C thermocouples are known to withstand higher temperatures.

Optimization of plug and thermocouple placement across the heatshield is another effort that could lead to better data products and more accurate analysis results. The location of MISP plugs and thermocouple depths were strategically selected for the MSL vehicle; however, a more rigorous optimization methodology can be beneficial. Dutta et al. [157, 158] developed a methodology for the placement optimization of flush atmospheric data system sensors and obtained optimized solutions for the location of MSL MEADS sensors. Similar analyses should be performed for TPS sensors as well.

Analysis presented in this work also showed that material property uncertainty,

especially high-temperature char properties, can lead to substantial uncertainty in surface heating estimation. Therefore, it is extremely valuable to perform a detailed pre-flight property characterization of the material samples used in the sensors. Similar efforts were conducted for the MSL instruments, which helped in deriving material property uncertainties relevant to MISP plugs. Future missions must focus on reducing these uncertainties and also monitoring material samples during design and manufacturing phases to ensure a low level of uncertainty in flight material properties. Placement of thermocouples closer to the surface can also reduce the effect of material property uncertainty on the heating estimation results.

6.3 Potential Augmentations of the Inverse Methodology

6.3.1 Multi-Parameter Estimation Framework

The framework developed here sets the groundwork for a systematic approach that enables a multi-parameter estimation analysis based on TPS experimental data. This baseline framework can be augmented in many different ways.

The Monte Carlo analysis performed in the uncertainty analysis is based on normal distributions for input parameters and a linear regression post-processing. It is possible to improve the Monte Carlo analysis by constructing more rigorous experiment-based material property distributions that also account for the dependency between material properties. This approach can be used in practice as more experimental data becomes available on material properties. Furthermore, in the case where normal distributions are not used for input parameters, it is crucial to employ more sophisticated uncertainty propagation methods such as analysis of variance or Sobol's sensitivity indices instead of a simple linear regression. Copeland et al. [133] discuss some of these methods and their application to Mars-relevant test cases.

The contribution plots generated as a part of the uncertainty analysis provided valuable insight regarding the time-dependent contribution of the input parameters

to model prediction uncertainty. In the arc jet application discussed in Chapter 3, these plots were examined at a high level to determine the parameters that were most important and the estimation was performed for the entire time range. Future applications can further use the available time-dependent information to break up the problem's time domain into multiple segments. Next, the uncertainty plots can be employed to identify the top contributors in each segment. Inverse analysis can then be performed for each segment with a fewer number of parameters. This will allow a more direct targeting of individual parameters based on their time-dependent contribution to model prediction uncertainty.

Some material properties such as thermal conductivity and specific heat are temperature dependent properties. In this work, it was assumed that the functional form of these properties with temperature were known and scaling factors for these properties were used. When these material properties were changed, the entire temperature dependent curve was shifted up and down. Through this approach, these properties were treated as constant parameters. It is also possible to consider the temperature dependent estimation of these properties; however, because this approach will be a function estimation problem, it will not fit well within the parameter estimation framework developed here. There has been significant work in the literature on temperature dependent estimation of thermophysical properties; however, such analyses for pyrolyzing ablative materials have been rare. [159, 160, 161, 162] A framework similar to the one developed for time-dependent estimation of surface heating can be used for the estimation of temperature-dependent material properties. Temperature-dependent estimation can result in a more accurate characterization of the TPS material properties and a better match between model predictions and data.

The inverse methods used in this work were based on an ordinary least-squares objective function and were deterministic. While it is possible to obtain some information about the uncertainties in the estimates and calculate confidence intervals,

such statistical analyses are based on many assumptions that are not valid for this problem (e.g., additive, normal, random errors). Other objective functions such as weighted least-squares, maximum likelihood or maximum a posteriori, are possible and Bayesian estimation methods can also be used. These estimation techniques will provide more information on estimation uncertainty; however, the use of statistical techniques for the problem on hand requires accurate characterization of sensor and model errors as such errors are inputs to these estimation algorithms.

In this work, the multi-parameter estimation framework was applied to one arc jet test case and one flight plug dataset to illustrate the benefits of the inverse analysis. The analyses can be similarly performed for other arc jet datasets and future flight data. Application to multiple arc jet datasets will address material property variability from one sample to another and provide a better confidence level for the estimation results. However, future applications to other test conditions might require additional analyses to resolve problem-dependent challenges.

6.3.2 Surface Heating Function Estimation Framework

The inverse methods used in this work for surface heating function estimation framework were whole-time domain methods. These methods estimate all the surface heating estimation points simultaneously using the entire measurement time span. Sequential estimation methods may be also employed. These methods estimate the surface heating sequentially in time using only a limited time span of the measurements. While whole-time domain methods are more stable, they are less efficient. However, in order to benefit from the efficiency of sequential methods, the computational code used for the direct problem must have the capability of saving solutions and restarting them in time. Unfortunately, FIAT does not have this capability at this time. If future versions of FIAT include this capability or if another tool is used that has this capability, sequential methods can provide similar results at a much

lower computational cost.

The surface heating estimation methods used in this work belonged to the class of deterministic regularization methods. Bayesian statistical techniques may be also used with the added benefit that these methods can provide further information on estimation uncertainty. To use these methods effectively, a good knowledge of measurement uncertainties and covariances are required. Such information was not available for the cases investigated in this work. If future programs perform a more detailed analysis of instrument measurement error and uncertainty, the prerequisite statistical information may become available and Bayesian methods can be employed for surface heating estimation problems.

The C_H estimation approach requires the calculation of many surface chemistry terms internally by FIAT. The equilibrium models used in FIAT for PICA gas-surface chemistry are not accurate at MSL heating conditions which limited the estimation of convective surface heating using the C_H estimation approach. Since validated finite-rate gas-surface chemistry models are not currently available for PICA in the Martian atmosphere, the total surface heating including the chemical contributions was estimated while assuming zero recession. While this approach provided great insight into the overall surface heating experienced by the MSL entry vehicle, direct estimation of C_H and the convective surface heating was not possible. In future, the C_H estimation approach must be revisited when PICA finite-rate gas-surface chemistry models become available and are validated for Martian environments. The results of that analysis can be more easily compared with CFD convective heating predictions.

This thesis presented a flexible methodology for preforming inverse analysis of TPS data independent of the computational tool used for the direct problem. FIAT, being the standard NASA tool for ablative thermal response modeling, was used here for the solution of the direct problem. In the future, as higher fidelity codes are

developed that more accurately model the problem physics, they could substitute FIAT in this methodology.

APPENDIX A

LIST OF PUBLICATIONS

A.1 Journal Articles

A.1.1 Published

1. **Mahzari, M.**, Braun, R., and White, T., "Reconstruction of Mars Pathfinder Aeroheating and Heat Shield Response Using Inverse Methods," *Journal of Spacecraft and Rockets*, Vol. 50, No. 6, 2013.

2. **Mahzari, M.** and Braun, R., "Time-Dependent Mars Entry Aeroheating Estimation from Simulated In-Depth Heat Shield Temperature Measurements," *Journal of Thermophysics and Heat Transfer*, Vol. 27, No. 3, 2013, pp. 435-446.

A.1.2 Planned

1. **Mahzari, M.**, and Braun, R., "A Multi-Parameter Estimation Methodology for Application to Planetary Entry Thermal Protection System Experimental Data," *Journal of Spacecraft and Rockets*, To be submitted in November 2013.

2. **Mahzari, M.**, Braun, R., White, T., and Bose, D., "Inverse Estimation of the Mars Science Laboratory Entry Aerothermal Environment and Thermal Protection System Response" *Journal of Spacecraft and Rockets*, To be submitted in November 2013.

3. Edquist, K., Hollis, B., Johnston, C., Bose, D., White, T., and **Mahzari, M.** "Mars Science Laboratory Heatshield Aerothermodynamics: Design and Reconstruction," *Journal of Spacecraft and Rockets*, Submitted July 2013.

4. White, T., Bose, D., **Mahzari, M.**, and Edquist, K., "Reconstruction of the Aerothermal Environment and Heatshield Response of the Mars Science Laboratory Entry Vehicle," *Journal of Spacecraft and Rockets*, Submitted July 2013.

A.2 Conference Papers

A.2.1 Published

1. Smith, B., Tanner, C., **Mahzari, M.**, Clark, I., Cheatwood, F.M., Braun, R., "A Historical Review of Inflatable Aerodynamic Decelerator Technology Development," IEEEAC 1276, 2010 IEEE Aerospace Conference, Big Sky, MT, March 2010.

2. **Mahzari, M.**, Cozmuta, I., Clark, I., Braun, R., "An Inverse Parameter Estimation Methodology for the Analysis of Aeroheating and Thermal Protection System Experimental Data," AIAA 2011-4027, 42nd AIAA Thermophysics Conference, Honolulu, Hawaii, June 2011.

3. White, T., Cozmuta, I., Santos, J., Laub, B., and **Mahzari, M.**, "Proposed Analysis Process for Mars Science Laboratory Heat Shield Sensor Plug Flight Data," AIAA 2011-3957, 42nd AIAA Thermophysics Conference, Honolulu, Hawaii, June 2011.

4. Copeland, S., **Mahzari, M.**, Cozmuta, I., and Alonso, J., "Statistics-Based Material Property Analysis to Support Ablation Simulation UQ Efforts," AIAA 2012-1763, 53rd AIAA/ASME/ASCE/AHS/ASC Structures, Structural Dynamics and Materials Conference, Honolulu, Hawaii, April 2012.

5. Dutta, S., **Mahzari, M.**, White, T., and Braun, R., "Integrated Trajectory, Atmosphere, and Aerothermal Reconstruction Methodology Using the MEDLI Dataset," 9th International Planetary Probe Workshop, Toulouse, France, June 2012.

6. **Mahzari, M.**, and Braun, R., "Time-dependent Estimation of Mars Science Laboratory Surface Heating from Simulated MEDLI Data," AIAA 2012-2871, 43rd AIAA Thermophysics Conference, New Orleans, Louisiana, June 2012.

7. **Mahzari, M.**, Braun, R., and White, T., "Reconstruction of Mars Pathfinder Aerothermal Heating and Heatshield Material Response Using Inverse Methods," AIAA 2012-2872, 43rd AIAA Thermophysics Conference, New Orleans, Louisiana, June 2012.

8. **Mahzari, M.**, White, T., Dutta, S., Braun, R., and Bose, D., "Preliminary Analysis of the Mars Science Laboratory's Entry Aerothermodynamic Environment and Thermal Protection System Performance," AIAA 2013-0185, 51st AIAA Aerospace Sciences Meeting, Grapevine, Texas, January 2013.

9. Bose, D., White, T., Santos, J., Feldman, J., **Mahzari, M.**, Olson, M., and Laub, B., "Initial Assessment of Mars Science Laboratory Heat Shield Instrumentation and Flight Data," AIAA 2013-0908, 51st AIAA Aerospace Sciences Meeting, Grapevine, Texas, 2013.

10. Bose, D., White, T., **Mahzari, M.**, and Edquist, K., "A Reconstruction of Aerothermal Environment and Thermal Protection System Response of the Mars Science Laboratory Entry Vehicle," 23rd AAS/AIAA Spaceflight Mechanics Meeting, AAS 13-311, Kauai, Hawaii, February 2013.

11. Bose, D., Santos, J., Rodriguez, E., White, T., and **Mahzari, M.**, "Mars Science Laboratory Heat Shield Instrumentation and Arc Jet Characterization," AIAA 2013-2778, 44th AIAA Thermophysics Conference, San Diego, California, June 2013

12. White, T., **Mahzari, M.**, Bose, D., and Santos, J., "Post-flight Analysis of

Mars Science Laboratory's Entry Aerothermal Environment and Thermal Protection System Response," AIAA 2013-2779, 44th AIAA Thermophysics Conference, San Diego, California, June 2013.

13. **Mahzari, M.**, Braun, R., White, T., and Bose, D., "Inverse Estimation of the Mars Science Laboratory Entry Aerothermal Environment and Thermal Protection System Response," AIAA 2013-2780, 44th AIAA Thermophysics Conference, San Diego, California, June 2013.

14. Edquist, K., Hollis, B., Johnston, C., Bose, D., White, T., and **Mahzari, M.** "Mars Science Laboratory Heatshield Aerothermodynamics: Design and Reconstruction," AIAA 2013-2781, 44th AIAA Thermophysics Conference, San Diego, California, June 2013.

A.2.2 Planned

1. White, T., **Mahzari, M.** and Bose, D., "Post-flight Review of the Mars Science Laboratory Heatshield Sizing and Margins Procedure" To be presented at 52nd AIAA Aerospace Sciences Meeting, National Harbor, Maryland, January 2014.

REFERENCES

[1] Braun, R. and Manning, R., "Mars Exploration Entry, Descent, and Landing Challenges," *Journal of Spacecraft and Rockets*, Vol. 44, No. 2, 2007, pp. 310–323.

[2] Steltzner, A., Kipp, D., Chen, A., Burkhart, P., Guernsey, C., Mendeck, G., Mitcheltree, R., Powell, R., Rivellini, T., Martin, A. S., and Way, D., "Mars Science Laboratory entry, descent and landing system," *IEEE Aerospace Conference*, IEEAC1497, Big Sky, MT, March 2006.

[3] Wright, M., Chun, T., Edquist, K., Hollis, B., Krasa, P., and Campbell, C., "A Review of Aerothermal Modeling for Mars Entry Missions," *48th AIAA Aerospace Sciences Meeting*, AIAA 2010-44, January 2010.

[4] Wright, M., Milos, F., and Tran, P., "Afterbody Aeroheating Flight Data for Planetary Probe Thermal Protection System Design," *Journal of Spacecraft and Rockets*, Vol. 43, No. 5, 2006, pp. 929–943.

[5] Milos, F., Chen, Y., Congdon, W., and Thornton, J., "Mars Pathfinder Entry Temperature Data, Aerothermal Heating, and Heatshield Material Response," *Journal of Spacecraft and Rockets*, Vol. 36, No. 3, 1999, pp. 380–391.

[6] Edquist, K., Dyakonov, A., Wright, M., and Tang, C., "Aerothermodynamic Design of the Mars Science Laboratory Heatshield," *41st AIAA Thermophysics Conference*, AIAA 2009-4075, San Antonio, Texas, June 2009.

[7] Beck, R., Driver, D., Wright, M., Laub, B., Hwang, H., Slimko, E., Edquist, K., Sepka, S., Willcockson, W., and Thames, T., "Development of the Mars Science Laboratory Heatshield Thermal Protection System," *41st AIAA Thermophysics Conference*, AIAA 2009-4229, San Antonio, Texas, June 2009.

[8] Gazarik, M., Wright, M., Little, A., Cheatwood, F., Herath, J., Munk, M., Novak, F., and Martinez, E., "Overview of the MEDLI Project," *IEEE Aerospace Conference*, IEEE 2008-1510, Big Sky, Montana, March 2008.

[9] White, T., Cozmuta, I., Santos, J., Laub, B., and Mahzari, M., "Proposed Analysis Process for Mars Science Laboratory Heat Shield Sensor Plug Flight Data," *42nd AIAA Thermophysics Conference*, AIAA 2011-3957, Honolulu, Hawaii, June 2011.

[10] Anderson, J., *Hypersonic and High-Temperature Gas Dynamics*, AIAA, 2nd ed., 2006.

[11] Hollis, B. and Prabhu, D., "Assessment of Laminar, Convective Aeroheating Prediction Uncertainties for Mars Entry Vehicles," *42nd AIAA Thermophysics Conference*, AIAA 2011-3144, Honolulu, Hawaii, June 2011.

[12] Gnoffo, P., "Planetary Entry Gas Dynamics," *Annual Review of Fluid Mechanics*, Vol. 31, 1999, pp. 459–494.

[13] Bose, D., Brown, J., Prabhu, D., Johnston, C., Gnoffo, P., and Hollis, B., "Uncertainty Assessment of Hypersonic Aerothermodynamics Prediction Capability," *42nd AIAA Thermophysics Conference*, AIAA 2011-3141, Honolulu, Hawaii, June 2011.

[14] Moss, J. and Price, J., "Survey of Blunt Body Flows Including Wakes at Hypersonic Low Density Conditions," *Journal of Thermophysics and Heat Transfer*, Vol. 11, No. 3, 1997, pp. 321–329.

[15] Wright, M., "Aerothermodynamics Lecture," *Guest Lecture for AE 6355 (Planetary Entry Descent and Landing)*, Georgia Institute of Technology, Spring 2009, Instructor: R.D. Braun.

[16] Pletcher, R., Tannehill, J., and Anderson, D., *Computational Fluid Mechanics and Heat Transfer*, Taylor and Francis, Inc., 2nd ed., 1997.

[17] Gnoffo, P., Gupta, R., and Shinn, J., "Conservation Equations and Physical Models for Hypersonic Air Flows in Thermal and Chemical Nonequilibrium," NASA TP 2867, February 1989.

[18] Park, C., "Assessment of Two-Temperature Kinetic Model for Air," *Journal of Thermophysics and Heat Transfer*, Vol. 3, No. 3, 1989, pp. 233–244.

[19] Millikan, R. and White, D., "Systematics of Vibrational Relaxation," *Journal of Chemical Physics*, Vol. 39, No. 12, 1963, pp. 3209–3213.

[20] Camac, M., "CO_2 Relaxation Processes in Shock Waves," *Fundamental Phenomena in Hypersonic Flow*, edited by J. Hall, Cornell University Press, 1964, pp. 195–215.

[21] Park, C., Howe, J., Jaffe, R., and Candler, G., "Review of Chemical-Kinetic Problems of Future NASA Missions, II: Mars Entries," *Journal of Thermophysics and Heat Transfer*, Vol. 8, No. 1, 1994, pp. 9–23.

[22] Gordon, S. and McBride, B., "Computer Program for Calculation of Complex Chemical Equilibrium Compositions and Applications," NASA RP 1311, October 1994.

[23] Capitelli, M., Colonna, G., Giordano, D., Marraffa, L., Casavola, A., Minelli, P., Pagano, D., Pietanza, L., and Taccogna, F., "High-Temperature Thermodynamic Properties of Mars-Atmosphere Components," *Journal of Spacecraft and Rockets*, Vol. 42, No. 6, 2005, pp. 980–989.

[24] Mitcheltree, R. and Gnoffo, P., "Wake Flow about the Mars Pathfinder Entry Vehicle," *Journal of Spacecraft and Rockets*, Vol. 32, No. 5, 1995, pp. 771–776.

[25] Wright, M., Bose, D., Palmer, G., and Levin, E., "Recommended Collision Integrals for Transport Property Computations I: Air Species," *AIAA Journal*, Vol. 43, No. 12, 2005, pp. 2558–2564.

[26] Wright, M., Hwang, H., and Schwenke, D., "Recommended Collision Integrals for Transport Property Computations II: Mars and Venus Entries," *AIAA Journal*, Vol. 45, No. 1, 2007, pp. 281–288.

[27] Baldwin, B. and Lomax, H., "Thin Layer Approximation and Algebraic Model for Separated Turbulent Flows," *16th AIAA Aerospace Sciences Meeting*, AIAA 1978-257, Huntsville, AL, January 1978.

[28] Menter, F., "Two-Equation Eddy-Viscosity Turbulence Models for Engineering Applications," *AIAA Journal*, Vol. 32, No. 8, 1994, pp. 1598–1605.

[29] Brown, J., "Turbulence Model Validation for Hypersonic Flows," *8th AIAA Thermophysics and Heat Transfer Conference*, AIAA 2002-3308, St. Louis, Missouri, June 2002.

[30] Tauber, M., "A Review of High-Speed Convective Heat Transfer Computation Methods," NASA TP-2914, July 1989.

[31] Chang, C., Choudhari, M., Hollis, B., and Li, F., "Transition Analysis for the Mars Science Laboratory Entry Vehicle," *41st AIAA Thermophysics Conference*, AIAA 2009-4076, San Antonio, Texas, June 2009.

[32] Reshotko, E. and Tumin, A., "Role of Transient Growth in Roughness-Induced Transition," *AIAA Journal*, Vol. 42, No. 4, 2004, pp. 766–770.

[33] Demetriades, A., Laderman, A., Seggern, L. V., Hopkins, A., and Donaldson, J., "Effect of Mass Addition on the Boundary Layer of a Hemisphere at Mach 6," *Journal of Spacecraft and Rockets*, Vol. 13, No. 8, 1976, pp. 508–509.

[34] Schneider, S., "Laminar-Turbulent Transition on Reentry Capsules and Planetary Probes," *Journal of Spacecraft and Rockets*, Vol. 43, No. 6, 2006, pp. 1153–1173.

[35] Anderson, B., "BLT Flight Experiment Overview and In-Situ Measurements," *48th AIAA Aerospace Sciences Meeting*, AIAA 2010-0240, Orlando, Florida, January 2010.

[36] Hollis, B., Liechty, D., Wright, M., Holden, M., Wadhams, T., MacLean, M., and Dyakonov, A., "Transition Onset and Turbulent Heating Measurements for the Mars Science Laboratory Entry Vehicle," *43rd AIAA Aerospace Sciences Meeting*, AIAA 2005-1437, Reno, Nevada, January 2005.

[37] Hollis, B. and Collier, A., "Turbulent Aeroheating Testing of Mars Science Laboratory Entry Vehicle in Nitrogen," *45th AIAA Aerospace Sciences Meeting*, AIAA 2007-1208, Reno, Nevada, January 2007.

[38] Stewart, D., "Determination of Surface Catalytic Efficiency for Thermal Protection Materials: Room Temperature to Their Upper Use Limit," *31st AIAA Thermophysics Conference*, AIAA 1996-1863, New Orleans, LA, June 1996.

[39] Sepka, S., Chen, Y., Marschall, J., and Copeland, R., "Experimental Investigation of Surface Reactions in Carbon Monoxide and Oxygen Mixtures," *Journal of Thermophysics and Heat Transfer*, Vol. 14, No. 1, 2000, pp. 45–52.

[40] Marschall, J., Copeland, R., Hwang, H., and Wright, M., "Surface Catalysis Experiments on Metal Surfaces in Oxygen and Carbon Monoxide Mixtures," *44th AIAA Aerospace Sciences Meeting*, AIAA 2006-0181, Reno, Nevada, January 2006.

[41] Mitcheltree, R., "Computational Aerothermodynamics for Mars Pathfinder Including Turbulence," AIAA 95-3493, August 1995.

[42] Wright, M., Olejniczak, J., Brown, J., Hornung, H., and Edquist, K., "Modeling of Shock Tunnel Aeroheating Data on the Mars Science Laboratory Aeroshell," *Journal of Thermophysics and Heat Transfer*, Vol. 20, No. 4, 2006, pp. 641–651.

[43] Wright, M., Candler, G., and Bose, D., "Data-Parallel Line Relaxation Method of the Navier-Stokes Equations," *AIAA Journal*, Vol. 36, No. 9, 1998, pp. 1603–1609.

[44] Cheatwood, F. and Gnoffo, P., "Users Manual for the Langley Aerothermal Upwind Relaxation Algorithm (LAURA)," NASA TM-4674, April 1996.

[45] Holden, M., "Studies of Surface Roughness and Blowing Effects on Hypersonic Turbulent Boundary Layers Over Slender Cones," *27th Aerospace Sciences Meeting*, AIAA 1989-0458, Reno, Nevada, January 1989.

[46] Wilcox, D., *Turbulence Modeling for CFD*, DCW Industries, La Canada, CA, 3rd ed., 2006.

[47] Chen, Y. and Milos, F., "Ablation and Thermal Response Program for Spacecraft Heatshield Analysis," *Journal of Spacecraft and Rockets*, Vol. 36, No. 3, 1999, pp. 475–483.

[48] Chen, Y. and Milos, F., "Navier-Stokes Solutions with Finite Rate Ablation for Planetary Mission Earth Reentries," *Journal of Spacecraft and Rockets*, Vol. 42, No. 6, 2005, pp. 961–970.

[49] Johnston, C., "A Study of Ablation-Flowfield Coupling Relevant to Orion Heatshield," *41st AIAA Thermophysics Conference*, AIAA 2009-4318, San Antonio, Texas, June 2009.

[50] MacLean, M., "Implicit Surface Boundary Conditions for Blowing, Equilibrium Composition, and Diffusion-Limited Oxidation," *48th AIAA Aerospace Sciences Meeting*, AIAA 2010-1179, Orlando, Florida, January 2010.

[51] Cruden, B., Martinez, R., Grinstead, J., and Olejniczak, J., "Simultaneous Vacuum Ultraviolet Through Near IR Absolute Radiation Measurement with Spatiotemporal Resolution in an Electric Arc Shock Tube," *41st AIAA Thermophysics Conference*, AIAA 2009-4240, San Antonio, Texas, June 2009.

[52] McDaniel, R., Wright, M., and Songer, J., "Aeroheating Predictions for Phoenix Entry Vehicle," *Journal of Spacecraft and Rockets*, Vol. 48, No. 5, 2012, pp. 727–745.

[53] Edquist, K., "Afterbody Heating Predictions for a Mars Science Laboratory Vehicle," *38th AIAA Thermophysics Conference*, AIAA 2005-4817, Toronto, Ontario, June 2005.

[54] Dec, J. A., *Three Dimensional Finite Element Ablative Thermal Response Analysis Applied to Heatshield Penetration Design*, Ph.D. thesis, Georgia Institute of Technology, May 2010.

[55] Sutton, K., "Heating Analysis for the Pioneer Venus Multiprobe Mission," NASA TM X-72001, July 1974.

[56] Milos, F., Chen, Y., Squire, T., and Brewer, R., "Analysis of Galileo Probe Heatshield Ablation and Temperature Data," *Journal of Spacecraft and Rockets*, Vol. 36, No. 3, 1999, pp. 298306.

[57] Laub, B., Chen, Y., and Dec, J., "Development of a High-Fidelity Thermal/Ablation Response Model for SLA-561V," *41st AIAA Thermophysics Conference*, AIAA 2009-4232, San Antonio, Texas, June 2009.

[58] Tran, H., Johnson, C., Rasky, D., Hui, F., Chen, Y., and Hsu, M., "Phenolic Impregnated Carbon Ablators (PICA) for Discovery Class Mission," *31st AIAA Thermophysics Conference*, AIAA 1996-1911, New Orleans, LA, June 1996.

[59] Milos, F. and Chen, Y., "Ablation and Thermal Response Property Model Validation for Phenolic Impregnated Carbon Ablator," *Journal of Spacecraft and Rockets*, Vol. 47, No. 5, 2010, pp. 786–805.

[60] Stackpoole, M., Sepka, S., Cozmuta, I., and Kontinos, D., "Post Flight Evaluation of Stardust Sample Return Capsule Forebody Heatshield Material," *46th AIAA Aerospace Sciences Meeting*, AIAA 2008-1202, Reno, NV, January 2008.

[61] Laub, B. and Curry, D., "Tutorial on Ablative TPS," *2nd International Planetary Probe Workshop*, NASA Ames Research Center, Moffett Field, CA, August 2004.

[62] Hurwicz, H., "Aerothermochemistry Studies in Ablation," *5th AGARD Colloquium on High-Temperature Phenomena*, Braunschweig, Germany, April 1962.

[63] Katsikas, C., Castle, G., and Higgins, J., "Ablation Handbook - Entry Materials Data and Design," AFML-TR-66-262, September 1966.

[64] Munson, T. and Spindler, J., "Transient Thermal Behavior of Decomposing Materials. Part I, General Theory and Application to Convective Heating," AVCO Corp., AVCO RAD-TR-61-10, Wilmington, MA, May 1961.

[65] Kratsch, K., Hearne, L., and McChesney, H., "Thermal Performance of Heat Shield Composites During Planetary Entry," Lockheed Missiles and Space LMSC-803099, Sunnyvale, CA, October 1963.

[66] Lees, L., "Convective Heat Transfer With Mass Addition and Chemical Reactions," *Third AGARD Colloquium on Combustion and Propulsion*, Pergamon, New York, 1959.

[67] Kendall, R., Rindal, R., and Bartlett, E., "Thermochemical Ablation," *AIAA Thermophysics Specialist Conference*, AIAA 1965-642, Monterey, CA, September 1965.

[68] Moyer, C. and Rindal, R., "An Analysis of the Coupled Chemically Reacting Boundary Layer and Charring Ablator-Part II. Finite Difference Solution for the In-Depth Response of Charring Materials Considering Surface Chemical and Energy Balances," NASA CR-1061, 1968.

[69] Goldstein, H., "Kinetics of Nylon and Phenolic Pyrolysis," Lockheed Missiles and Space Co., LMSC-667876, Sunnyvale, CA, October 1965.

[70] Acurex UM-87-11/ATD, Acurex Corporation, Aerotherm Division, Mountain View, California, *User's Manual, Aerotherm Charring Material Thermal Response and Ablation Program*, November 1987.

[71] Milos, F., Chen, Y., and Squire, T., "Updated Ablation And Thermal Response Program For Spacecraft Heatshield Analysis," *17th Thermal and Fluids Analysis Workshop*, TFAWS06-1008, University of Maryland, August 2006.

[72] Milos, F. and Chen, Y., "Comprehensive Model for Multicomponent Ablation Thermochemistry," *35th AIAA Aerospace Sciences Meeting*, AIAA 1997-0141, Reno, NV, January 1997.

[73] Acurex Report UM-81-11/ATD, Acurex Corporation, Aerotherm Division, Mountain View, California, *Users Manual, Aerotherm Chemical Equilibrium Computer Program (ACE)*, August 1981.

[74] Kays, W. and Crawford, M., *Convective Heat and Mass Transfer*, McGraw Hill, New York, 2nd ed., 1980.

[75] Lachaud, J., Magin, T., Cozmuta, I., and Mansour, N., "A Short Review of Ablative-Material Response Models and Simulation Tools," *7th Aerothermodynamics Symposium*, Brugge, Belgium, May 2011.

[76] Laub, B., "Ablator Modeling: Why Not Much Has Changed Over the Past 45+ Years," *4th AF/SNL/NASA Ablation Workshop*, Albuquerque, NM, March 2011.

[77] Milos, F. and Chen, Y., "Two-Dimensional Ablation, Thermal Response, and Sizing Program for Pyrolyzing Ablators," *Journal of Spacecraft and Rockets*, Vol. 46, No. 6, 2009, pp. 1089–1099.

[78] Chen, Y. and Milos, F., "Three-Dimensional Ablation and Thermal Response Simulation System," *38th AIAA Thermophysics Conference*, AIAA 2005-5064, Toronto, Ontario, June 2005.

[79] Dec, J., Braun, R., and Laub, B., "Ablative Thermal Response Analysis Using the Finite Element Method," *Journal of Thermophysics and Heat Transfer*, Vol. 26, No. 2, 2012, pp. 201–212.

[80] Lachaud, J. and Mansour, N., "A Pyrolysis and Ablation Toolbox-based on OpenFOAM, with Application to Material Response under High-enthalpy Environments," *5th OpenFOAM Workshop*, Chalmers, Gothenburg, Sweden, June 2010.

[81] Mansour, N., Lachaud, J., Magin, T., de Muelenaere, J., and Chen, Y., "High-Fidelity Charring Ablator Thermal Response Model," *42nd AIAA Thermophysics Conference*, AIAA 2011-3124, Honolulu, Hawaii, June 2011.

[82] Amar, A., Calvert, N., and Kirk, B., "Development and Verification of the Charring Ablating Thermal Protection Implicit System Solver," *49th AIAA Aerospace Sciences Meeting*, AIAA 2011-144, Orlando, Florida, January 2011.

[83] Milos, F., Chen, Y., and Gokcen, T., "Nonequilibrium Ablation of Phenolic Impregnated Carbon Ablator," *48th AIAA Aerospace Sciences Meeting*, AIAA 2010-981, Orlando, Florida, January 2010.

[84] Lachaud, J., Cozmuta, I., and Mansour, N., "Multiscale Approach to Ablation Modeling of Phenolic Impregnated Carbon Ablators," *Journal of Spacecraft and Rockets*, Vol. 47, No. 6, 2010, pp. 910–921.

[85] Dec, J., "Thermal Protection Systems," *Guest Lecture for AE 6355*, Georgia Institute of Technology, Spring 2009, Instructor: R.D. Braun.

[86] Laub, B., Balboni, J., and Goldstein, H., "Ground Test Facilities for TPS Development," NASA TM-2002-211400, NASA Ames Research Center, Moffett Field, California, 2002.

[87] Laub, B., "Use of Arc-Jet Facilities in the Design and Development of Thermal Protection Systems," *25th AIAA Aerodynamic Measurement Technology and Ground Testing Conference*, AIAA 2006-3292, San Francisco, California, June 2006.

[88] Congdon, W., "Thermostructural Testing of Scaled Ablative-Aeroshell Systems Using the Sandia Solar Tower Facility," *40th AIAA Thermophysics Conference*, AIAA 2008-3909, Seattle, Washington, June 2008.

[89] Lander, M., Bagford, J., North, M., and Hull, R., "Characterization of the Thermal Performance of High Heat Flux Systems at the Laser Hardened Materials Evaluation Laboratory," *Proc. SPIE*, Vol. 2855, 1996, pp. 129–137, High Heat Flux Engineering III.

[90] Ingoldby, R., Michel, F., Flaherty, T., Doryand, M., Preston, B., Villyard, K., and Steele, R., "Entry Data Analysis for Viking Landers 1 and 2 Final Report," NASA CR-159388, Martin Marietta Corporation, 1976.

[91] Schmitt, D., "Base Heating on a an Aerobraking Oribital Transfer Vehicle," *21st AIAA Aerospace Sciences Meeting*, AIAA 83-0408, Reno, Nevada, January 1983.

[92] Edquist, K., Wright, M., and Allen, G., "Viking Afterbody Heating Computations and Comparisons to Flight Data," *44th AIAA Aerospace Sciences Meeting*, AIAA 2006-386, Reno, Nevada, January 2006.

[93] Mahzari, M., Braun, R., and White, T., "Reconstruction of Mars Pathfinder Aerothermal Heating and Heatshield Material Response Using Inverse Methods," *43rd AIAA Thermophysics Conference*, AIAA 2012 2872, New Orleans, Louisiana, June 2012.

[94] Wakefield, R. and Pitts, W., "A Description of the Heatshield Experiment on the Pioneer-Venus Entry Probe," AIAA 1978-917, Palo Alto, CA, 1978.

[95] Wakefield, R. and Pitts, W., "Analysis of the Heat-Shield Experiment on the Pioneer-Venus Entry Probes," *15th AIAA Thermophysics Conference*, AIAA 1980-1494, July 1980.

[96] Milos, F., "Galileo Probe Heat Shield Ablation Experiment," *31st AIAA Thermophysics Conference*, AIAA 1996-1823, New Orleans, LA, June 1996.

[97] Desai, P., Qualls, G., and Schoenenberger, M., "Reconstruction of the Genesis Entry," *Journal of Spacecraft and Rockets*, Vol. 45, No. 1, 2008, pp. 33–38.

[98] Tang, C. and Wright, M., "Analysis of the Forebody Aeroheating Environment during Genesis Sample Return Capsule Reentry," *45th AIAA Aerospace Sciences Meeting*, AIAA 2007-1207, Reno, Nevada, January 2007.

[99] Horvath, T., "The Hythirm Project: Flight Thermography of the Space Shuttle During Hypersonic Re-entry," *48th AIAA Aerospace Sciences Meeting*, AIAA 2010-241, Orlando, Florida, January 2010.

[100] Oishi, T., Martinez, E., and Santos, J., "Development and Application of a TPS Ablation Sensor for Flight," *46th AIAA Aerospace Sciences Meeting*, AIAA 2008-1219, January 2008.

[101] Santos, J., Jacobs, T., and Martinez, E., "Isotherm Sensor Calibration Program for Mars Science Laboratory Heat Shield Flight Data Analysis," *42nd AIAA Thermophysics Conference*, AIAA 2011-3955, Honolulu, Hawaii, June 2011.

[102] Bose, D., "MISP Reconstruction Readiness Status," *Presented at MEDLI Peer Review*, NASA Ames Research Center, Moffett Field, CA, July, 24, 2012.

[103] Beck, J. and Arnold, K., *Parameter Estimation in Engineering and Science*, Wiley, New York, 1977.

[104] Beck, J., Blackwell, B., and Clair, C. S., *Inverse Heat Conduction, Ill-posed Problems*, Wiley, New York, 1985.

[105] Alifanov, O., *Inverse Heat Transfer Problems*, Springer-Verlag, New York, 1994.

[106] Ozisik, M. and Orlande, H., *Inverse Heat Transfer: Fundamentals and Applications*, Taylor and Francis, New York, 2000.

[107] Woodbury, K., *Inverse Engineering Handbook*, CRC Press, Boca Raton, 2003.

[108] Kurpisz, K. and Nowak, A., *Inverse Thermal Problems*, WIT Press, Southampton, UK, 1995.

[109] Orlande, H., Fudym, F., Maillet, D., and Cotta, R., *Thermal Measurements and Inverse Techniques*, CRC Press, Boca Raton, FL, 2011.

[110] Aster, R., Borchers, B., and Tauber, C., *Parameter Estimation and Inverse Problems*, Elsevier Academic Press, Burlington, 2005.

[111] Spencer, D., Blanchard, R., Braun, R., Kallemeyn, P., and Thurman, S., "Mars Pathfinder Entry, Descent, and Landing Reconstruction," *Journal of Spacecraft and Rockets*, Vol. 36, No. 3, 1999, pp. 357–366.

[112] Christian, J., Verges, A., and Braun, R., "Statistical Reconstruction of Mars Entry, Descent, and Landing Trajectories and Atmospheric Profiles," *AIAA SPACE Conference and Exposition*, AIAA 2007-6192, Long Beach, CA, 2007.

[113] Dutta, S. and Braun, R., "Mars Entry, Descent, and Landing Trajectory and Atmosphere Reconstruction," *48th AIAA Aerospace Sciences Meeting*, AIAA 2010-1210, Orlando, FL, January 2010.

[114] Wells, G., *A Comparison of Multiple Techniques for the Reconstruction of Entry, Descent and Landing Trajectories and Atmospheres*, Ph.D. thesis, Georgia Institute of Technology, May 2011.

[115] Dutta, S., Braun, R., Russell, R., Clark, I., and Striepe, S., "Comparison of Statistical Estimation Techniques for Mars Entry, Descent, and Landing Reconstruction from MEDLI-like Data Sources," *50th AIAA Aerospace Sciences Meeting*, AIAA 2012-0400, Nashville, TN, January 2012.

[116] Shunlin, L., editor, *Advances in Land Remote Sensing: System, Modeling, Inversion and Application*, Springer, University of Maryland, 2008.

[117] Bertero, M. and Boccacci, P., *Introduction to Inverse Problems in Imaging*, Institute of Physics, London, UK, 1998.

[118] Tapley, B., Schutz, B., and Born, G., *Statistical Orbit Determination*, Elsevier Academic Press, Burlington, MA, 2004.

[119] Orlande, H., "Inverse Problems in Heat Transfer: New Trends on Solution Methodologies and Applications," *Journal of Heat Transfer*, Vol. 134, No. 3, 2012.

[120] Tikhonov, A. and Arsenin, V., *Solution of Ill-Posed Problems*, Winston and Sons, Washington, DC, 1977.

[121] Tikhonov, A., Lenov, A., and Yagola, A., *Nonlinear Ill-posed Problems*, Chapman and Hall, London, 1998.

[122] Alifanov, O., "Solution of an Inverse Problem of Heat Conduction by Iterative Methods," *Journal of Engineering Physics*, Vol. 26, No. 4, 1974, pp. 471–476.

[123] Beck, J., "Nonlinear Estimation Applied to the Nonlinear Inverse Heat Conduction Problem," *International Journal of Heat and Mass Transfer*, Vol. 13, No. 4, 1970, pp. 703–716.

[124] Kalman, R., "A New Approach to Linear Filtering and Prediction Problems," *ASME Journal of Basic Engineering*, Vol. 82, 1960, pp. 3545.

[125] Zarchan, P. and Musoff, H., *Fundamental of Kalman Filtering, A Practical Approach*, American Institute of Aeronautics and Astronautics, Inc., Reston, VA, 2000.

[126] Julier, S., Uhlmann, J., and Durrant-Whyte, H., "A New Method for the Nonlinear Transformation of Means and Covariances in Filters and Estimators," *IEEE Transactions on Automatic Control*, Vol. 45, No. 3, 2000, pp. 477482.

[127] Kaipio, J. and Fox, C., "The Bayesian Framework for Inverse Problems in Heat Transfer," *Heat Transfer Engineering*, Vol. 32, No. 9, 2011, pp. 718–753.

[128] Dec, J. and Mitcheltree, R., "Probabilistic Design of A Mars Sample Return Entry Vehicle Thermal Protection System," *40th AIAA Aerospace Sciences Meeting*, AIAA 2002-0910, January 2002.

[129] Bose, D., Wright, M., and Gokcen, T., "Uncertainty and Sensitivity Analysis of Thermochemical Modeling for Titan Atmospheric Entry," *37th AIAA Thermophysics Conference*, AIAA 2004-2455, July 2004.

[130] Wright, M., Bose, D., and Chen, Y., "Probabilistic Modeling of Aerothermal and Thermal Protection Material Response Uncertainties," *AIAA Journal*, Vol. 45, No. 2, 2007, pp. 399–410.

[131] Chen, Y., Squire, T., Laub, B., and Wright, M., "Monte Carlo Analysis for Spacecraft Thermal Protection System Design," *9th AIAA/ASME Joint Thermophysics and Heat Transfer Conference*, AIAA 2006-2951, June 2006.

[132] Sepka, S. and Wright, M., "A Monte Carlo Approach to FIAT Uncertainties-Improvements and Applications for MSL," *41st AIAA Thermophysics Conference*, AIAA 2009-4243, June 2009.

[133] Copeland, S., Mahzari, M., Cozmuta, I., and Alonso, J., "A Statistics-Based Material Property Analysis to Support Ablation Simulation UQ Efforts," *53rd AIAA/ASME/ASCE/AHS/ASC Structures, Structural Dynamics and Materials Conference*, AIAA 2012-1763, Honolulu, Hawaii, April 2012.

[134] Levenberg, K., "A Method for the Solution of Certain Non-linear Problems in Least Squares," *Quart. Appl. Math.*, Vol. 2, 1944, pp. 164–168.

[135] Marquardt, D., "An Algorithm for Least-Squares Estimation of Nonlinear Parameters," *Journal of the Society for Industrial and Applied Mathematics*, Vol. 11, No. 2, 1963, pp. 431–441.

[136] Colaco, M. and Orlande, H., "Comparison of Different Versions of the Conjugate Gradient Method of Function Estimation," *Numerical Heat transfer, Part A*, Vol. 36, 1999, pp. 229–249.

[137] Laub, B., "The Mysteries of Real Materials," *5th Ablation Workshop*, Lexington, Kentucky, February 2012.

[138] "CEV Thermal Protection System (TPS) Margin Management Plan," NASA Internal Technical Document, C-TPSA-A-DOC-7005.

[139] Szalai, C., Thoma, B., Lee, W., Maki, J., Willcockson, W., Venkatapathy, E., and White, T., "Mars Exploration Rover Heatshield Observation Campaign," *42nd AIAA Thermophysics Conference*, AIAA 2011-3956, Honolulu, Hawaii, June 2011.

[140] Wright, M., White, T., and Mangini, N., "Data Parallel Line Relaxation (DPLR) Code User Manual; Acadia-Version 4.01.1," NASA TM 2009-215388, Oct. 2009.

[141] Ramshaw, J., "Self-Consistent Effective Binary Diffusion in Multicomponent Gas Mixtures," *Journal of Non-Equilibrium Thermodynamics*, Vol. 15, No. 3, 1990, pp. 295–300.

[142] MPFL-M-ASIMET-4-DDR-EDL-V1.0, m., "ASI/MET Derived EDL Density/Pressure/Temperature Profiles," NASA Planetary Data System, April 1999.

[143] Chen, Y., Henline, W., and Tauber, M., "Mars Pathfinder Trajectory Based Heating and Ablation Calculations," *Journal of Spacecraft and Rockets*, Vol. 32, No. 2, 1995, pp. 225–230.

[144] Bose, D., Santos, J., Rodriguez, E., White, T., and Mahzari, M., "Mars Science Laboratory Heat Shield Instrumentation and Arc Jet Characterization," *44th AIAA Thermophysics Conference*, AIAA 2013-2778, San Diego, CA, June 2013.

[145] White, T., Mahzari, M., Bose, D., and Santos, J., "Post-fight Analysis of Mars Science Laboratory's Entry Aerothermal Environment and Thermal Protection System Response," *44th AIAA Thermophysics Conference*, AIAA 2013-2779, San Diego, CA, June 2013.

[146] Edquist, K., Hollis, B., Johnston, C., Bose, D., White, T., and Mahzari, M., "Mars Science Laboratory Heatshield Aerothermodynamics: Design and Reconstruction," *44th AIAA Thermophysics Conference*, AIAA 2013-2781, San Diego, CA, June 2013.

[147] Karlgaard, C., Schoenenberger, M., Kutty, P., and Shidner, J., "Mars Science Laboratory Entry, Descent, and Landing Trajectory and Atmosphere Reconstruction," *AAS/AIAA Space Flight Mechanics Meeting*, AAS 13-307, Kauai, Hawaii, February 2013.

[148] Bose, D., White, T., Mahzari, M., and Edquist, K., "A Reconstruction of Aerothermal Environment and Thermal Protection System Response of the Mars Science Laboratory Entry Vehicle," *23rd AAS/AIAA Spaceflight Mechanics Meeting*, AAS 13-311, Kauai, Hawaii, February 2013.

[149] Wright, M., Beck, R., Edquist, K., Driver, D., Sepka, S., Slimko, E., Willcockson, W., DeCaro, A., and Hwang, H., "Sizing and Margins Assessment of the Mars Science Laboratory Aeroshell Thermal Protection System," *41st AIAA Thermophysics Conference*, AIAA 2009-4231, San Antonio, Texas, June 2009.

[150] Cozmuta, I., Wright, M., Laub, B., and Willcockson, W., "Defining Ablative Thermal Protection System Margins for Planetary Entry Vehicles," *42nd AIAA Thermophysics Conference*, AIAA 2011-3757, Honolulu, Hawaii, June 2011.

[151] Driver, D., Caballo, E., Beck, R., Prabhu, D., Santos, J., Cassell, A., Skokova, K., Hwang, H., Slimko, E., Willcockson, B., and Songer, J., "Arc Jet Testing in a Shear Environment for Mars Science Laboratory Thermal Protection System," *41st AIAA Thermophysics Conference*, AIAA 2009-4230, San Antonio, Texas, June 2009.

[152] Driver, D. and MacLean, M., "Improved Predictions of PICA Recession in Arc Jet Shear Tests," *49th AIAA Aerospace Sciences Meeting*, AIAA 2011-141, Orlando, Florida, January 2011.

[153] Lebel, P. and Russell, J., "Developement of Sensors to Obtain In-Flight Ablation Measurements of Thermal Protection Materials," NASA TN D-3686, November 1966.

[154] Schairer, E. and Heineck, J., "Photogrammetric Recession Measurements of Ablative Materials during Arcjet Testing," *45th AIAA Aerospace Sciences Meeting*, AIAA 2007-1158, Reno, NV, January 2007.

[155] Papadopoulos, G., Tiliakos, N., and Thomson, C., "Real-Time Ablation Recession Rate Sensor System for Advanced Reentry Vehicles," *50th AIAA Aerospace Sciences Meeting*, AIAA 2012-0531, Nashville, TN, January 2012.

[156] Natali, M., Koo, J., Allcorn, E., and Ezekoye, O., "In-situ Ablation Recession Sensor Based on Ultra-Miniature Thermocouples - Part A: 0.25 mm Diameter Thermocouples," *49th AIAA/ASME/SAE/ASEE Joint PropulsionConference*, AIAA 2013-3660, San Jose, CA, July 2013.

[157] Dutta, S., Braun, R., and Karlgaard, C., "Atmospheric Data System Sensor Placement Optimization for Mars Entry, Descent, and Landing," *AIAA Atmospheric Flight Mechanics Conference*, AIAA 2012-4507, Minneapolis, Minnesota, August 2012.

[158] Dutta, S. and Braun, R., "Cramer-Rao Lower Bound Optimization of Flush Atmospheric Data System Sensor Placement," *AIAA Atmospheric Flight Mechanics Conference*, AIAA 2013-4502, Boston, MA, August 2013.

[159] Sawaf, B. and Ozisik, M., "An Inverse Analysis to Estimate Linearly Temperature-Dependent Thermal Conductivity Components and Heat Capacity of an Orthotropic Medium," *International Journal of Heat and Mass Transfer*, Vol. 38, No. 16, 1995, pp. 3005–3010.

[160] Dantas, L. and Orlande, H., "A Function Estimation Approach for Determining Temperature-Dependent Thermophysical Properties," *Inverse Problems in Engineering*, Vol. 3, No. 4, 1996, pp. 261279.

[161] Dowding, K., Beck, J., and Blackwell, B., "Estimating Temperature-Dependent Thermal Properties," *Journal of Thermophysics and Heat Transfer*, Vol. 13, No. 3, July-September 1999, pp. 328–336.

[162] Molavi, H., Hakkaki-Fard, A., Pourshaban, I., Fard, M. M., and Rahmani, R., "Estimation of Temperature-Dependent Thermophysical Properties of Noncharring Ablators," *Journal of Thermophysics and Heat Transfer*, Vol. 23, No. 1, 2009, pp. 50–58.